SUBWAVELENGTH NANOSTRUCTURES FOR OPTICAL BIOSENSING AND RAPID PHOTOCHEMICAL REACTIONS

BY

HYUNJONG JIN

DISSERTATION

Submitted in partial fulfillment of the requirements
for the degree of Doctor of Philosophy in Electrical and Computer Engineering
in the Graduate College of the
University of Illinois at Urbana-Champaign, 2012

Urbana, Illinois

Doctoral Committee:

Assistant Professor Gang Logan Liu, Chair
Professor Brian T. Cunningham
Professor Kyekyoon Kim
Professor John A. Rogers
Assistant Professor Xiuling Li

ABSTRACT

This thesis reports on the experimental examination of the use of nanostructures for three topics of light-matter interaction.

First, enhanced photon absorption for photocatalytic reactions has been demonstrated. Photocatalytic metal nanoparticle synthesis is of significant interest in plasmonic biosening due to the simple fabrication capability. However, long synthesis time of more than 10 hours and the use of particle stabilization chemical agents hinder economical and rapid synthesis of such metal nanoparticle systems. We demonstrate a Si subwavelength nanostructure-based photochemical device. We show rapid photocatalytic structure transformation of noble metal nanoparticle ionization and reduction within 5 minutes with only pure water and room light illumination.

Second, 3D nanostructures for optical biosensing have been investigated. We demonstrate optical spectroscopy by using subwavelength dielectric nanostructures as the substrate material for localized surface plasmon resonance metallic nanoparticles. Nanostructured substrates made of Si and Si_3N_4 have been characterized and compared. Schemes of enhancing the optical signal extraction are also discussed. We show the potential of dielectric based nanostructure substrate for applications in optical molecular sensing.

Third, the experimental approaches from the two demonstrations are merged for photocatalytic nanoparticles. TiO_2 nanoparticles are formed along the sidewall of subwavelength Si nanostructure. The dual semiconductor system is investigated for photocatalytic bacteria disinfection in water. We show disinfection of E. coli with just room light illumination on our proposed device. Possibilities of extending this device towards water splitting are also discussed.

Each application is introduced with a brief motivation, description of the experimental method, and discussion of the results. Possible future directions are also presented.

This thesis is dedicated to

my father Dr. Min Jin for sharing his wisdom,
my mother Hee Sook Kwon for her unconditional love,
&
my wife Sung Jin Park for being the woman I love.

ACKNOWLEDGMENTS

I would like to thank my adviser, Prof. Gang Logan Liu. His enthusiasm and encouragement have helped me to develop independence and innovation in research. As his first doctoral student, having the chance to take part in the early development of his research group has been a valuable experience. I am grateful for his guidance and thank him for valuing my opinions throughout my graduate career. I would also like to thank my committee members, Prof. Brian T. Cunningham, Kyekyoon Kim, John A. Rogers, and Xiuling Li for providing their expertise in evaluation of this project.

I appreciate the help from fellow group members: Te-Wei, Sujin, Gulsim, Zidar, Jimmy and Austin. I am grateful for those that have helped me start this journey: Prof. Kanti Jain, Dr. Junghun Chae, Dr. Linus Jang, Dr. Kevin Lin, and Dr. Yoonsoo Han.

I would like to reserve my most sincere gratitude for my family. My father, Dr. Min Jin, has always been my source of wisdom. My mother, Hee Sook Kwon, will always be the strength that guides me through any difficulties. I thank my brother Austin Jin, Dr. Won-Zei Park and Ki Nam Oh for their moral support.

Lastly, but most importantly, I would like to thank my wife, Sung Jin Park, for all the happiness she brings to my life. She has been, and always will be, the love of my life. Thank you for blessing my life.

TABLE OF CONTENTS

CHAPTER 1

LIGHT-MATTER INTERACTION FOR APPLICATIONS TOWARDS RENEWABLE ENERGY AND BIOSENSING

In the 21st century we are met with a consistent increase in demand for technological innovation to overcome the challenges our society faces. Diminishing natural resources along with the need for sustainable growth have led to investigations toward clean renewable energy schemes. Increase in population and life expectancy have driven the demand for technological advancement in healthcare. This presents engineering tasks for innovative approaches that may cost effectively deliver high performance in both fields. For energy, the specific conditions required for wind generators and the recent tragedies involving nuclear power plants have opened opportunities for utilizing solar energy. For healthcare, increasing average age and recent pandemics have heightened the need for low cost, high throughput biosensors for pharmaceutical and vaccine development procedures.

The conversion of solar radiation to consumable electrical energy has been explored in the field of photovoltaics [1] and also photocatalytic water splitting [2]. Semiconductor material with an electrical band gap absorbs the incoming photon, converting optical energy to excited electron-hole pairs. In photovoltaic, the electrical carriers are directly extracted by proper energy band engineering. In photocatalytic water splitting, the excited electric carriers are injected into the electrolyte, enhancing the chemical reactions in the proximity of the device surface. Both applications require practical schemes to increase the photon absorption by the semiconductor surface to enhance such energy conversion efficiency.

In the field of optical biosensors, fluorescence based detection and label-free detection based on Raman scattering are the dominant approaches. Incoming excitation laser would interact with the molecule of interest. In fluorescence enhancement, such a molecule would be a fluorescent dye that would absorb the incoming light and reemit at a higher wavelength. This requires the detection target molecules to be tagged with such fluorescent dye material.

For Raman scattering, the excitation signal is inelastically scattered from the molecule of interest itself. The loss of energy during the interaction with the vibrational state indicates the specific chemical bonds, which may identify the molecule. Hence, the basis of optical biosensor relies on a complex interaction between incoming light, the device surface that is typically made of metal, and the molecule of interest.

To provide the theoretical basis for both applications, in which incoming photons interact with different types of materials, this chapter discusses light-matter interaction. Section 1.1 introduces scattering, with emphasis on Rayleigh and Mie scattering. Section 1.2 discusses the light-metal interaction, leading to the illustration of surface plasmon resonance and localized surface plasmon resonance. The light-molecule interactions, ranging from absorption to fluorescence and scattering, are discussed in Section 1.3. The extension of scattering into surface enhanced Raman scattering based on plasmonic surfaces is discussed in Section 1.4. Finally, Section 1.5 provides the readers with the overview of this thesis.

1.1 Interaction between light and matter: scattering

Scattering is the change in propagation direction of an electromagnetic (EM) wave in the presence of a perturbing obstacle, as illustrated in Fig. 1.1. The electron orbits within such obstacles induce an oscillation with equal frequency to that of the incoming EM wave, causing a dipole moment. This dipole moment acts as an EM radiation source, causing the scattering of the incoming EM wave. The majority of scattered radiation propagates in the same frequency as the original incident source, hence referred as elastic scattering [3]. As light possesses the dual identity of particle and wave, such wave theory is sufficient to describe propagation properties. It should be noted that consideration of solid-state physics would be required for light-matter interaction at the nanoscale.

We may describe the interaction between light and matter by showing the relation between incident light intensity with that of scattered. With the use of spherical coordinates, with the center of the scattering particle as the coordinate origin,

$$I_{scat} = I_0 \frac{1}{r^2} \sigma_{scat} \tag{1.1}$$

with I_{scat} and I_0 as the light intensity for scattering and incident, respectively. For spherical particles, it can be assumed that scattered light follows the identical polarization as the incident light. Hence the scattering cross section, σ_{scat}, may be thought as the average of the two polarizations of interest.

The development of the above expression into a mathematical expression for the cross sections may be carried out in two frameworks, Rayleigh scattering and Mie scattering. The theory established by Rayleigh applies to cases when the perturbing obstacle particle of interest is small in comparison to incident light wavelength and when absorption may be neglected. Mie theory is the general approach that is not limited by particle size. It is also able to incorporate absorbing materials.

While Mie theory provides a wider scope of interest, Rayleigh scattering is the preferred framework due to the relative simplicity. The condition that validates such approximation is

$$|m|A \leq 1 \tag{1.2}$$
$$for\ A = \frac{2\pi a n_0}{\lambda}\ and\ m = n - i\gamma$$

where a is the spherical radius of the scattering particle, n_0 is the index of refraction of the surrounding medium, n is the index of refraction of the scattering particle, γ is the absorption term defined as

$$\gamma = \frac{absorption\ coefficient\ * \lambda}{4\pi}$$

In the regime of Rayleigh, the scattering cross section σ_{scat} may be defined as

$$\sigma_{scat} = \frac{2\pi^5}{3} \frac{(n^2-1)^2}{(n^2+2)^2} \frac{a^6}{\lambda^4} \tag{1.3}$$

The interesting result from Rayleigh scattering is the scattering cross section dependence in the power of 6 to the spherical radius of the scattering particle

and that in the power of 4 to the incident wavelength. Such behavior is the basis behind the blue color of the sky during daylight, since the blue wavelength would scatter strongly in comparison to red. Only when we are to limit the incoming solar illumination to a straight path, which would occur during sunrise and sunset, will the red become the dominant color seen from the solar radiation.

The thorough analytic treatment of Mie scattering may be found in works such as [3].

1.2 Light-metal interaction: surface plasmon resonance and localized surface plasmon resonance

Other than graded refractive index nanostructures, optical trapping may also be possible with the utilization of surface plasmons. At the same time, such surface plasmon conditions may be used for biosensing applications. This section overviews the background for surface plasmons which is the basis for metal enhanced fluorescence (MEF) and surface enhanced Raman scattering (SERS).

Materials with negative real and small positive imaginary dielectric constant can support surface plasmon resonance. Noble metals such as Ag and Au satisfy the resonance condition in the optical wavelength [4]. Surface plasmon polaritons (SPP), as in Fig. 1.2, are seen in continuous film of metal-dielectric interface. We may interpret SPP as a coherent oscillation of the free electrons of a conducting surface that is excited by an incoming electromagnetic wave. The plasmon will propagate along the metal-dielectric interface and has an evanescent decay in the out-of-plane direction. The resonance condition is highly sensitive to the dielectric constant of the surrounding medium, and hence acts as an efficient sensing mechanism. Such shifts due to interactions between the SPP with a molecule may be observed with fixed wavelength varied angle, variable wavelength fixed angle, or fixed wavelength fixed angle.

Application of the Drude-Sommerfeld model for metals may formulate the dispersion relation in the surface plasmon phenomena. In this framework, the electrons are allowed to freely move until they collide with other electrons, defects, and phonons. The rate of such collisions is denoted as γ, which would

be the inverse of the electron relaxation time. The frequency dependent dielectric function of the metal may be described as

$$\varepsilon_r = 1 - \frac{\omega_p^2}{\omega^2 + i\omega\Gamma} \tag{1.4}$$

where ω_p is the plasmon frequency and Γ is the electron collision rate described above.

In solving for the plasmon at a metal-dielectric interface, the longitudinal wave propagation may be described as

$$k = \frac{\omega}{c}\sqrt{\frac{\varepsilon}{\varepsilon + 1}} = \frac{\omega}{c}\sqrt{\frac{\omega^2 - \omega_p^2}{2\omega^2 - \omega_p^2}} \tag{1.5}$$

The resulting dispersion curve is shown in Fig. 1.3. Since the surface plasmon dispersion has a momentum mismatch for the identical frequency with photons, incident light cannot directly excite such plasmonic modes. Hence additional momentum must be provided, which may be done by the use of prisms in practical applications. This additional requirement hinders such surface plasmon based sensing for cost effective, rapid optical biosensing.

Controlled fabrication of nanoparticles has led to demonstration of localized surface plasmonic resonance (LSPR). Incoming optical radiation induces an oscillation of charge, hence plasmons that oscillate locally around the nanoparticle as shown in Fig. 1.2. Similar to SPP, the LSPR condition is sensitive to the dielectric conditions, and may be directly used for sensing applications [4]. An important characteristic of LSPR is the EM field enhancement relative to the incident field in direct proximity of the metallic nanoparticle when resonance condition is met. The illustration is shown in Fig. 1.2 for the case of single particle LSPR. The field density is locally enhanced when the particle is in resonance. However, for off resonance, such effect is not seen. Arrays of such features create local hot spots of EM field enhanced regions in between adjacent nanoparticles. This condition, which is fulfilled in the visible wavelengths for gold or silver, is the basis for surface enhanced spectroscopy. LSPR conditions may be tuned with the size, shape, material of the nanoparticle, and the gap distance between the metal features [4].

LSPR has a single resonance frequency, whereas SPP has the dispersion relation shown above. With the physical system consisting of metal particles in the nanoscale, absorption and scattering both become of interest in studying the extinction characteristics. Hence we would need to use the Mie scattering approach described above.

1.3 Light-molecule interaction: absorption, fluorescence, and scattering

The light-molecule interaction is described by the Jablonski diagram as show in Fig. 1.4. The different interactions shown are absorption, fluorescence, Rayleigh scattering, Raman scattering, and phosphorescence. Rayleigh scattering has been covered in previous sections, and Raman will be discussed in the following section. Hence the discussion within will focus on the remaining interactions.

The incident light exchanges energy with the molecule in a quantized way by three different methods: electrical energy, vibrational energy, and rotational energy. Each electric energy level may be divided into several different vibrational modes, and each vibrational mode may be continuously split into rotational levels, as shown in Fig. 1.5.

When molecules absorb incoming photon energy, it may be excited to a higher electrical energy level. However, the excitation would prefer to fall into the same vibrational mode within the excited energy level. This is explained by the Franck-Condon theory. It occurs since the physical atomic dislocation, hence vibrational mode, may not transition in the same time scale as the light absorption. Hence the nuclei would not be able to transition immediately, causing the molecule to prefer a relatively higher energy. It would take additional time for the molecule to relax down to a lower vibrational mode within the excited energy state.

The electrical energy states in the diagram may be categorized by the status of electron spin, with S representing a singlet state and T for triplet state. The singlet state is the case for when spin is balanced, hence there would not be any need for reorientation for relaxation. On the other hand, triplet state requires the spin to reorient before relaxation. For this, singlet state is referred to as short-lived whereas triplet is long-lived, as shown in

Fig. 1.6.

With the definitions, it is now possible to explain the process for both fluorescence and phosphorescence. In the case of fluorescence, the incoming photon causes the molecule to enter a higher electrical energy level that corresponds to the vibrational mode it was originally in. After the molecule reorients to a lower vibrational mode, the molecule undergoes an electrical energy level relaxation, emitting a photon. The molecule would fall into the vibrational mode it was in immediately prior to relaxation. It would then further undergo relaxation of vibrational modes. For phosphorescence, rather than directly relaxing, the excited energy state would transition to a triplet state via intersystem crossing as seen in Fig. 1.6. The system would then relax to the electrical energy ground state, emitting a photon. Normally intersystem crossing is not allowed, but spin-orbit coupling may increase the probability of such occurrence. In comparison to fluorescence, the intersystem crossing as well as the required reorientation of spin causes phosphorescence to have a lower probability and hence a longer relaxation time.

1.4 Surface enhanced Raman scattering

The Raman scattering, or Raman effect, is the inelastic scattering effect of photons on the vibrational or rotational states of molecules. Incident photons of certain frequency are inelastically scattered, and shifted in the frequency domain by a characteristic molecular vibration frequency amount. This amount in frequency shift is used to identify the molecule of interest. Typically the scattered Raman signal will result in energy lower than the incident wave. Another feature of interest is the bandwidth of the Raman signal in comparison to fluorescence. The fluorescence spectrum is relatively broadband, and does not give as much information of the molecule structure. On the other hand, the Raman signal provides information related to the vibrational levels of the molecule, which may be used to specifically identify the molecule type [5]. However, Raman scattering has an extremely low cross section, which is 12 to 14 orders lower than that of fluorescence. This result in low probability of Raman scattering occurrence (1 in a million incident photons), hence the signal strength is weak [6].

The Raman scattering may be treated analytically referring to the approach taken for the light-matter scattering above. With the incident EM wave interacting with a particle, the strength of the dipole moment that is induced, P, may be expressed as

$$P = \alpha E_0 cos(2\pi f_0 t) \tag{1.6}$$

with α as the polarizability, E_0 as the amplitude and f_0 as the frequency of the incoming EM wave.

Since the interaction between the incoming EM wave and the electrons in a material would depend on the relative locations of atoms, we may take polarizability to be dependent on the locational displacement of atoms during vibrations. Such physical displacement may be expressed as

$$dL = L_0 cos(2\pi f_v t)$$

where L_0 is the maximum displacement and f_v is the vibrational mode frequency. If we insert the above expression for polarization, with Taylor expansion it may be simplified to

$$\alpha = \alpha_0 + \frac{\partial \alpha}{\partial L} dL = \alpha_0 + \frac{\partial \alpha}{\partial L} L_0 cos(2\pi f_v t)$$

Inserting the above expression into Eq. 1.6, we are able to get

$$P = \alpha_0 E_0 cos(2\pi f_0 t) + (\frac{\partial \alpha}{\partial L} \frac{L_0 E_0}{2}) \{cos[2\pi(f_0 - f_v)t] + cos[2\pi(f_0 + f_v)t]\} \tag{1.7}$$

Hence it is shown in Eq. 1.7 that there are three possible scattering frequencies. The first terms indicate that the scattered signal follows the same frequency as the incident wave. Hence this would be the elastic scattering, in other words Rayleigh or Mie scattering. The two inelastic scatterings described above are Raman scattering, with the decrease in frequency corresponding to Stokes shift and the other to anti-Stokes shift.

For applications toward spectroscopy, considerations of scattering cross section must be understood. It is conventional to consider the scattering signal in units of cm^{-1} hence in terms of wavenumber. The relation between

the scattering cross section and wavenumber is described as

$$\sigma \sim (\omega_0 - \omega_v)^4 \tag{1.8}$$

where ω_0 and ω_v are the wavenumber of the incident light and scattered signal, respectively. Hence the Raman cross section will increase as the incident light wavelength decreases. However, the possibilities of absorption may also increase as shorter wavelength lasers such as those in UV range are used. Also, since the wavelength difference between the incident light and target Raman signal is constant, the utilization of lower wavelength laser forces the difference between the two to decrease. This may make it difficult to differentiate between the incident light and Raman scattered light. For such reasons, typical Raman setups utilize the lasers in the visible wavelengths.

The Raman effect may be enhanced mainly with electromagnetic field enhancement. Such surface enhanced Raman scattering (SERS) utilizes the resonance of incident optical wave with localized surface plasmon modes of the metal substrate. This induces a redistribution of near EM fields to the substrate. The SERS substrate from this effect can be considered as nanoscale antennas for transmitting and enhancing the Raman scattering effect. The enhancement depends on the interaction between plasmons, excitation, and scattered fields. Hence the surface morphology, material, and excitation wavelength would determine the degree of enhancement. Matching the resonance condition of the LSPR metal particle array with the excitation light would highly increase the SERS effect. With the SERS excitation wavelength fixed, different shapes of nanoparticle array are fabricated to shift the LSPR resonance condition. It is seen that the SERS data decreases as the LSPR resonance peak deviates from excitation laser wavelength [7]. For increased efficiency of SERS, it would be advantageous to have more EM hot spots per surface area. The planer surface metallic particle packing approach is limited by the lithography capability. It would have enhanced efficiency with capability of additional dimensionality of hot spot formation.

The LSPR nanoparticle array provides enhancement of fluorescence. Both the radiative and non-radiative decay rates of the fluorophore are modified. The radiative decay is dominantly affected in comparison, resulting in an increase in the quantum yield of the fluorescence process [6]. Such effect arises from the coupling between LSPR modes with the emission band of

fluorophores. Hence the enhancement will be highly affected by the LSPR mode conditions as well as the distance between the fluorophores and metal particles [8]. Similar to LSPR based SERS, high density EM hot spots would increase the fluorescence enhancement effect.

1.5 Overview of thesis

The thesis will cover the topics of subwavelength nanostructure device for applications in photocatalytic reactions and optical biosensing, as illustrated in Fig. 1.7. With Chapter 1 providing the background, Chapter 2 will focus on the fabrication of nanostructures. Reviews of previously reported fabrication schemes are illustrated to provide a background for comparison. Optical characterization of the proposed device has been done to prove the capability of enhanced photon absorption. In Chapter 3, the highly photon absorbent semiconductor surface is used for photocatalytic transformation of metal nanoparticles. The direct reduction of metal ions has also been demonstrated. The thesis then discusses the use of such nanostructures as the backbone material for 3D stacked metal nanoparticles in Chapter 4. Different approaches of forming such 3D metal nanoparticle structure are discussed. Optical biosensing performance dependence on the substrate material is also investigated. The fabrication schemes for such metal nanoparticles have also been applied for semiconductor material such as TiO_2, which is utilized for water disinfection and water splitting experiments in Chapter 5.

This thesis has been structured such that the reader may gain insight into the described material in separate chapters without needing to read the entire thesis. Each chapter provides sufficient details about the experimental approaches as well as future directions so readers may extend the details towards other applications of interest.

1.6 Figures

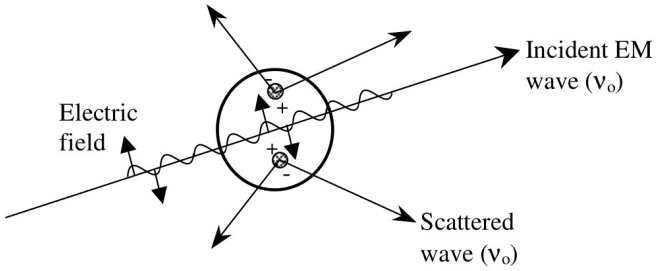

Figure 1.1: The interaction between incoming EM wave and matter [3].

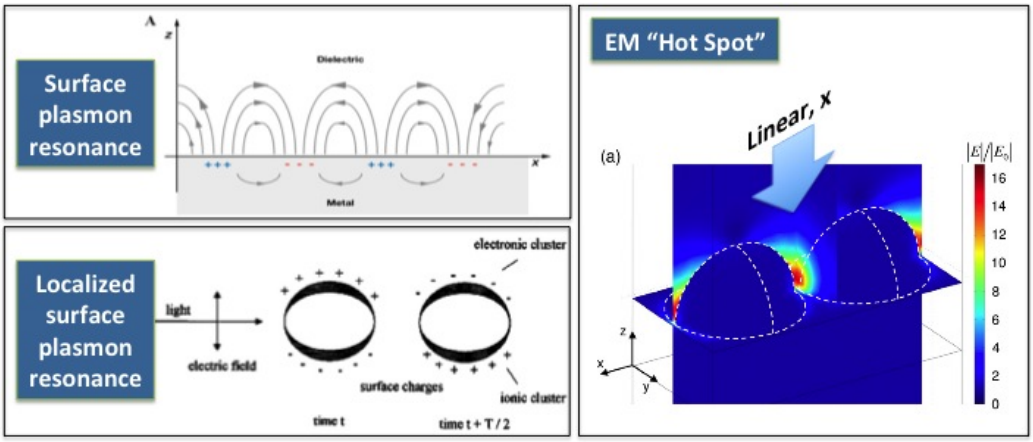

Figure 1.2: Schematic diagram showing the incoming electric field and corresponding electric carrier movement for surface plasmon resonance (SPR) [4] and localized surface plasmon resonance (LSPR) [9]. The EM hot spots formed due to LSPR are show as well [10].

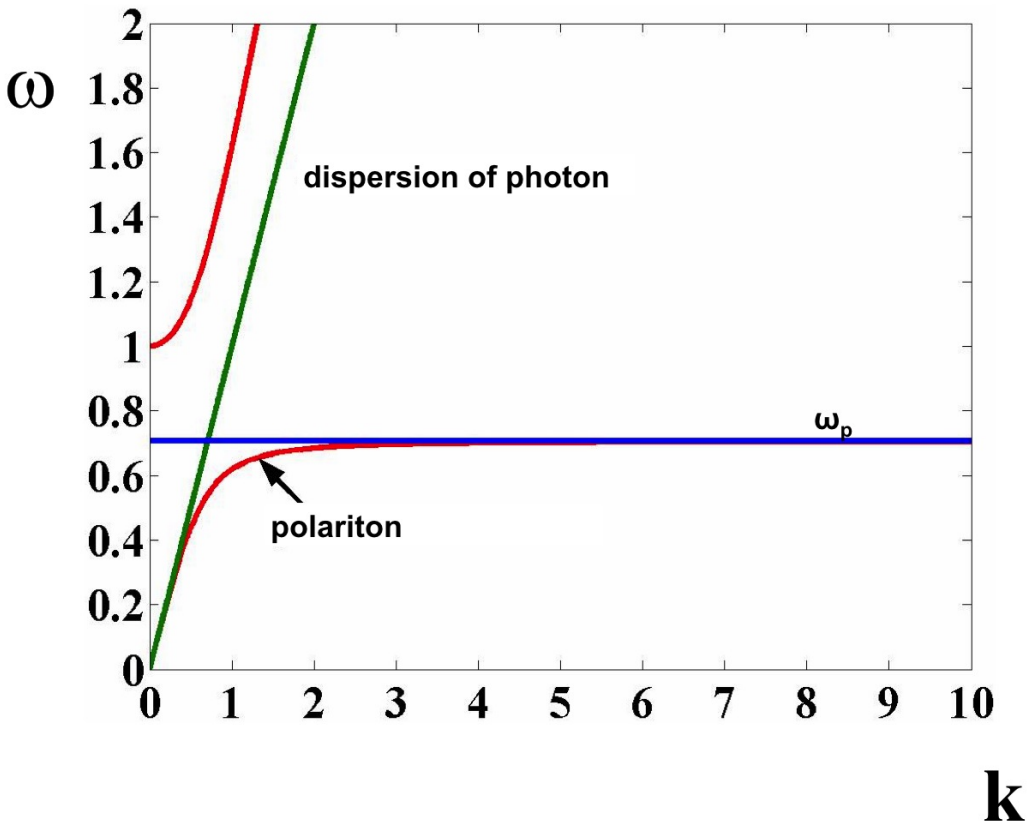

Figure 1.3: An example of the dispersion relationship for surface plasmon resonance [11].

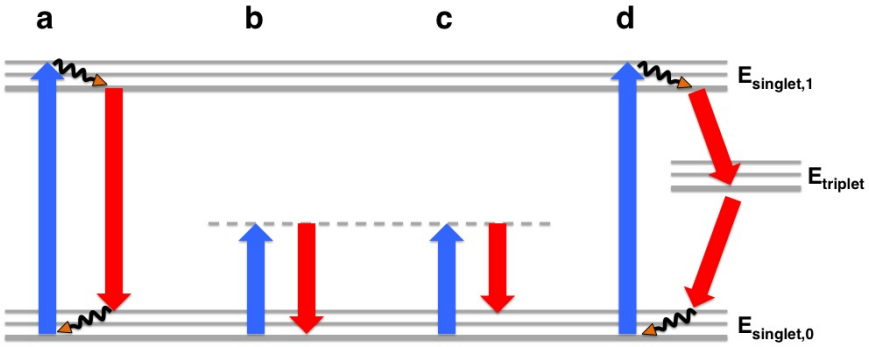

Figure 1.4: The Jablonski diagram showing (a) Fluorescence. (b) Rayleigh scattering. (c) Raman scattering. (d) Phosphorescence.

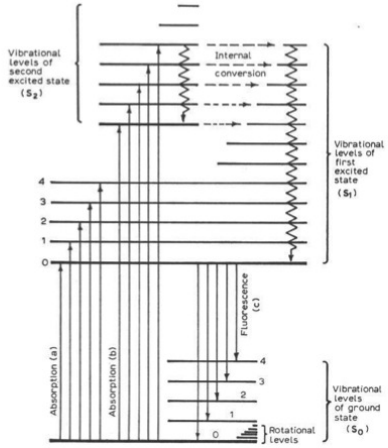

Figure 1.5: The energy diagram of a molecule showing the electrical energy level, vibrational energy level and rotational energy level [12].

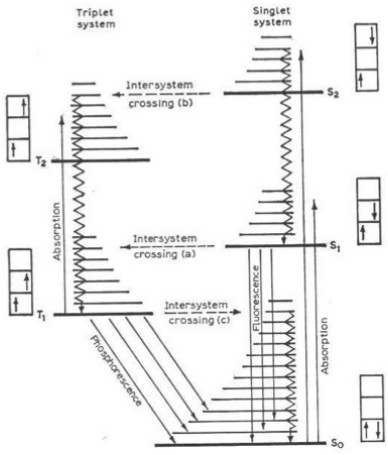

Figure 1.6: Diagram showing the intersystem crossing process during phosphorescence [12].

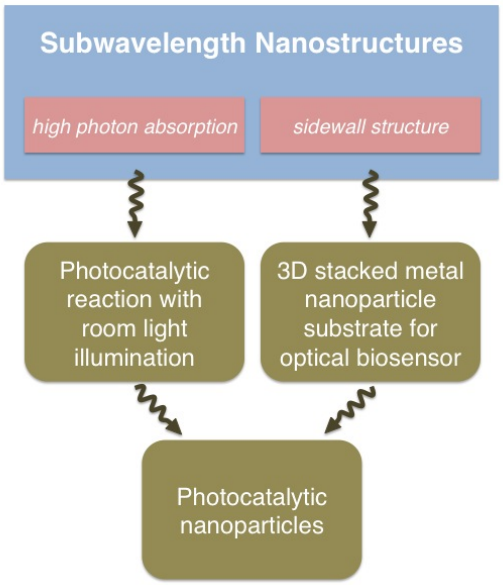

Figure 1.7: Schematic illustrating the overview of the thesis. Two distinct properties, high optical absorption and repeated grooved sidewalls of nanostructures, are explored. The results gained from both experiments are merged for demonstration on photocatalytic nanoparticles.

CHAPTER 2

FABRICATION AND CHARACTERISTICS OF SUBWAVELENGTH NANOSTRUCTURES

For photoelectric devices such as photovoltaic (PV) devices and photodetectors, enhancements in the incident photon absorption by the semiconductor materials can improve the photoelectric energy conversion efficiency and device sensitivity. The lack of absorption as well as leaking of light has been a major source of energy loss within solar cells [1] as shown in Fig. 2.1. Methods that utilize diffuse reflection substrates [13] or distributed Bragg reflector with antireflection coating [14] on thin film Si have provided prolonging of optical absorption pathway within PV device structure. However, such films are only efficient for normal light incidence and for specific wavelengths [15]. Highly efficient reduction in the reflection over a wide range of incident angle as well as over the broadband solar spectrum is proved to be difficult, especially for thin film PV devices with the thickness of a few microns. Here, we discuss the capabilities of subwavelength nanostructures to have two functions: effectively absorb incoming photons over a wide range of wavelength and ensure light trapping within the semiconductor device.

The outline of this chapter is as follows: Section 2.1 introduces the previous literature survey on fabrication of randomized subwavelength nanostructure. Section 2.2 provides the same for ordered and semi-ordered nanostructures. The fabrication of the proposed nanopore/nanoscrew Si device is illustrated in Section 2.3. Fluidic characteristics of the proposed devices are given in Section 2.4, with optical characteristics in Section 2.5. Concluding remarks will follow in Section 2.6.

2.1 Review on fabrication of randomized nanostructures

Randomized nanoscale silicon features are based on non-lithographic approaches. Such random nanostructure may be fabricated by a wet metal-assisted chemical etching approach [16, 17, 18, 19] or by a dry etching scheme [20, 21, 22, 23].

This typically reduces the number of steps required for device fabrication, enabling an economical approach towards achieving subwavelength nanostructures. Also, the randomness of the structure enables scattering of incoming waves over a broad range of wavelengths. The disadvantage, however, is the relative difficulty in predicting the specific optical properties of the randomized surface structures. The practical fabrication issues associated with each approach are illustrated below as well.

The metal-assisted chemical etching utilizes HF/H_2O_2 solution based Si etching. Metal nanoparticles are randomly dispersed on the Si substrate, which acts as a catalyst for the Si etching reaction. The overall chemistry is balanced in Eq. 2.1 and Eq. 2.2.

$$\begin{aligned} &\textit{Cathode reaction} - \textit{ at proximity of catalyst metal}: \\ &\mathrm{H_2O_2 + 2H^+ \rightarrow 2H_2O + 2h^+} \\ &\mathrm{2H^+ + 2e^- \rightarrow H_2} \end{aligned} \tag{2.1}$$

$$\begin{aligned} &\textit{Anode reaction} - \textit{ at etching target, which is } \mathrm{Si}: \\ &\mathrm{Si + 4h^+ + 4HF \rightarrow SiF_4 + 4H^+} \\ &\mathrm{SiF_4 + 2HF \rightarrow H_2SiF_6} \end{aligned} \tag{2.2}$$

Hence, the overall chemical reactions results in the catalytic the conversion of Si to H_2SiF_6. This approach of chemical based etching produces a deep directional etch into the Si substrate only in the proximity of noble metallic particles. However, the chemical etch would still induce surface roughening in other areas that were not targeted for deep etch, as seen in Fig. 2.2.

The resulting surface damage may be a disadvantage for chemical based subwavelength nanostructure fabrication, especially due to increased surface defects. To overcome such difficulties, similar structures may be made by

plasma etching as well. Rapid thermal annealing (RTA) based metal nanodot assembly [24, 25, 20] provides metallic etching mask. Metal thin film of approximately 10 nm is deposited on a prepared Si substrate by methods such as electron beam evaporation. The metal deposited Si wafer is subjected to RTA. Thermal capillary wave is applied to the Ag thin film by the injected thermal energy [25]. The wavelength of the wave depends on the thickness of metal layer and the surface tension between two materials [24]. With enough energy, selected areas of the substrate with high amplitude will break the metal thin film and form isolated metal particles. The substrate is then subjected to reactive ionic etching (RIE). Due to the random distribution of the RTA metal mask, the resulting pillar structures will also have random diameter and inter-pillar distance, as seen in Fig. 2.3. The requirement of an etching mask based on noble metals sets limitations on this approach in comparison to the other cost-effective fabrication schemes.

Direct self-masking in the RIE process is another approach. The plasma in the RIE chamber provides randomly distributed passivation that would act as an etching mask for Si etching [21, 22, 23]. The chemical reaction within the RIE chamber leads to formation of oxide-based nanoparticles simultaneously during Si etching. The resulting nanostructure takes the form of slightly tapered pillars, as in Fig. 2.4. This approach has the advantage of reducing fabrication steps required for the fabrication of pillar structures. However, the delicate condition required to form the self-induced etching mask narrows the processing window. The condition also becomes increasingly challenging to match due to the loading effect [26] as the target wafer size increases.

2.2 Review on fabrication of ordered and semi-ordered nanostructures

In comparison to random structures, the fabrication schemes for ordered nanostructures allow relative robustness as well as ease of study. The high reproducibility as well as superior yield has led to investigation of various approaches to achieve such subwavelength nanostructures.

One method of fabricating ordered nanostructures is the use of ebeam lithography [27] as in Fig. 2.5. By defining the nanoscale features by on alumina by ebeam lithography, it is possible to form a robust etching mask on Si.

Sequentially, the Si wafer is subjected to inductively coupled plasma (ICP) RIE to remove the exposed regions. The size of the Si nanostructure may be additionally thinned by thermal oxidation of the nanostructure surface [28]. However, the use of ebeam lithography makes this approach difficult to scale to larger area applications.

To a certain dimension limit, optical lithography may also be used to overcome the difficulty of ebeam lithography [29]. With the utilization of interference lithography, periodic features in the range of 100 nm and similar spacing may be patterned on photoresist. The patterned photoresist is then hard-baked as an etching mask for subsequent RIE process. The resulting structures form the same periodic patterns of that formed by the initial lithography step, as shown in Fig. 2.6. The disadvantage of this approach is the complex optics and lens strength required. Also, multiple additional steps of lithography are required for planar surfaces to be integrated with this sample.

The metal-assisted chemical etching process discussed for random nanostructure formation can also be used with various approaches of metal patterning for ordered structures as well. The process starts with evaporating a 10 nm thick layer of Ag on the Si wafer. While there are lithographic and ebeam based approaches [30], our interest is to discuss non-lithographic approaches for higher throughput and cost effectiveness. With a process called superionic solid state stamping (S4) [31], an Ag_2S stamp is brought into contact with the Ag thin film on the Si substrate. A voltage bias is applied across the stamp and substrate setup, inducing ions from the Ag thin film to be released into the stamp. This causes the Ag thin film to form reverse patterns of the prepared stamp, effectively patterning the Ag metal mask on Si in nanoscale features. Hence metal-assisted chemical etching on this substrate would result in the fabrication of specific patterns, as illustrated in Fig. 2.7. Various patterns shown in Fig. 2.8 can be formed by this approach [32].

Ordered silicon nanopillars based on nanosphere lithography and subsequent RIE have been demonstrated on Si substrates [33, 34]. The overview and results are displayed in Fig. 2.9. Polystyrene or silica nanospheres are uniformly dispersed on Si wafer. For efficient etching and shorter inter-pillar distance, monolayer deposition of nanosphere is preferred. The pillar diameter may be controlled by the initial sphere diameter as well as subsequent

nanosphere shrinking by isotropic dry etch. The sample is then etched in RIE for fabrication of nanopillars. Tapered nanopillars may also be fabricated by etching the nanosphere and the substrate material at the same time [33]. Intentionally utilizing etching gas that has low selectivity between the nanosphere and substrate material may do this. The difficulty of nanosphere lithography based etch is the required multiple steps required for integration with planar surface.

Another approach to produce ordered nanostructure without lithography is the semi-ordered masking by anodized aluminum oxidation (AAO) templates followed by focused ion beam (FIB) etching [35]. The method itself would provide a robust and possibly economical way to produce nanostructures of interest. However, previous approaches based on AAO templates generally cannot produce efficient light trapping features such as deep pore structures or pillars that have aspect ratios higher than 4, as shown in Fig. 2.10. Capabilities to overcome such limitations and having precise control of structural geometry may elucidate more physical insight of light trapping nanostructures.

2.3 Fabrication of nanopore/nanoscrew Si

In this section, we report on the demonstration of a robust fabrication approach for making both nanopores and a type of graded refractive-index substrate we name as nanoscrews due to the tapered pillar appearance. AAO template is formed as an etching mask against subsequent deep reactive-ion etching (DRIE) process. The etching is significantly efficient and the longest etch time performed for micron-height samples reported in this chapter has been less than 100 seconds. Also, the capability to freely select the nanostructures to be either nanopore or nanoscrew with the same surface pattern provides versatility in device fabrication.

The fabrication procedures for both nanopore and nanoscrew are illustrated in Fig. 2.11. Unless stated otherwise, device fabrication and characterization have been conducted within the Micro and Nanotechnology Laboratory in the University of Illinois at Urbana-Champaign. N-type single crystalline Si $< 100 >$ sample is degreased with acetone and IPA. Thorough residue removal of sample is done by 5:1 H_2SO_4/H_2O_2 piranha etch followed

by 10:1 HF for oxide removal. 200 nm of Al is deposited onto the substrate either by thermal or electron beam evaporation with 99.99% pure Al source. The sample is then immersed into 0.3 M oxalic acid where a constant voltage of 40 V is applied across the Al film and counter electrode. This condition is from previous literature in which pore distance of 95 nm has been observed [36]. For the Al film presented in this chapter, the anodization time of total 12 minutes has been used. The AAO mask pores are then widened by Transene Al Etchant type A, which completes that AAO template formation. The resulting SEM images are shown in Fig. 2.12. Nanopore and nanoscrew Si are made by DRIE in a STS Advanced Silicon Etcher (STS ASE). The STS ASE provides high aspect ratio deep etching of Si with the Bosch process, with alternates between etching with SF_6 and sidewall passivation with C_4H_8. Such alternation of etching and passivation allows enhancement of anisotropic etch in the ICP RIE process, as seen in Fig. 2.13. The difference between the fabrications of the nanopore and nanoscrew is the etch/passivation rate ratio applied for the Bosch process. If the etch/passivation ratio is balanced such that the passivation is enough to protect the sidewalls during etch, Si nanopore structure can be obtained. As seen in Fig. 2.11, the nanopore samples show specular reflection characteristics and the change in optical reflection characteristics is dependent on the depth of the nanopores. On the other hand, with more aggressive etching compared to passivation, the undercut beneath the AAO mask results in the tapered nanoscrew features. Due to their graded refractive-index nature, the nanoscrew samples only show very low diffuse reflectance. The apparent diffuse reflectance color changes and higher nanoscrews exhibit enhanced suppression in the reflectance intensity. After Si etching, both types of samples are put under hydrofluoric (HF) acid followed by piranha etch and then HF etch to remove the AAO mask and polymer byproducts of Bosch process.

The nanopore and nanoscrew features may be integrated with each other or with a planar surface on the same substrate by photolithography. Conventional lithography with Karl Suss MJB3 Contact Mask Aligner and S1818 as photoresist (PR) is used for differentiation of the surface. For nanopore or nanoscrew integration with planar Si surface, as in the left image of Fig. 2.14, lithography is directly done on the AAO template covered substrate prior to DRIE process. The PR covered portion is protected against the nanopore and nanoscrew formation.

2.4 Fluidic properties of nanopore/nanoscrew Si

In absence of an external electric field, the surface hydrophobicity comes from the balance of surface tension. The physical system consisting of a water droplet on a particular rigid substrate can be divided into domains of solid (substrate), liquid (water) and vapor (ambient surrounding) [37]. The balanced water droplet surface tension comes from the summation of three different interfacial energies: solid-vapor (E_{sv}), solid-liquid (E_{sl}), and liquid-vapor (E_{lv}). It is worth noting the direction of each energy as well, shown in Fig. 2.15. E_{sv} is parallel to the substrate surface away from the droplet surface, E_{sl} is also in parallel to the substrate but towards the droplet surface and liquid-vapor E_{lv} is in the normal direction of the water droplet. The relation between the interfacial energy and contact angle, a, is

$$cos(a) = \frac{E_{sv} - E_{sl}}{E_{lv}} \tag{2.3}$$

In addition to contact angle, the surface state is also of interest to correctly understand the fluidic properties of a micro or nanostructured surface. The Cassie state is that in which an air gap is trapped between the applied liquid droplets. On the other hand, the Wenzel state is when no such gaps exist. The surface is completely wetted when in the Wenzel state [38].

In fluidic characteristics, we have tested the contact angle of water on the prepared nanopore/nanoscrew surface. The contact angle measurements in Fig. 2.16 illustrate the self-wetting nature of our device. The hydrophilic nanoscrew is used as the channel, whereas the hydrophobic nanopore is used as the channel surrounding. A photograph of the finished device, with demonstration of fluidic confinement within the hydrophilic channel, is shown in Fig. 2.17. It is shown that the nanopore is in the Cassie state and has a relatively high contact angle ranging from 60° to 149° for different etching depths. As for the nanoscrew, the contact angle is less than 6° and is in the Wenzel state.

The hydrophilic nature of the nanoscrew substrate is due to enhanced roughening caused by the grooves on the nanostructure sidewalls. It has been previously demonstrated that extreme roughness in nanoscale features would lead a normally hydrophobic substrate to exhibit complete surface wetting [39]. Such illustration is shown in Fig. 2.18.

2.5 Optical characteristics of nanopore/nanoscrew Si

Optical characteristics of Si nanostructures were evaluated by diffuse reflectance measurements via a Varian Cary 5 G spectrophotometer. Scanning Electron Microscopy (SEM) images were taken from a Hitachi S4800 High Resolution SEM system. The SEM images in Fig. 2.19 show the side view of the nanopores, along with the same in higher magnifications. Silicon nanopores with etching depths targeted for approximately 550 nm, 750 nm, and 1600 nm are shown. The scalloped profiles of the nanopore sidewall are formed due to the etch/passivation sequence of the Bosch process. The discrepancy between neighboring pore depths in the same sample are due to the etching rate dependence to AAO mask opening. The AAO mask templates are only semi-ordered, hence adjacent pores may have different diameters. This creates increased etching rate in larger diameter pores, which becomes more apparent as the target etching depth increases. The optical data shows significantly suppressed specular reflectance, with the 1600 nm deep sample becoming essentially black. However, the nanopore surfaces have an abrupt change in the refractive index; hence they still have strong optical reflection at the Si-air interface. This is seen from the diffuse reflection measurements that are included in the plot of Fig. 2.19. Fig. 2.20 shows optical characteristics related to the graded refractive-index nanoscrews. Nanoscrews with average approximate heights of 550 nm, 800 nm, and 1300 nm are shown. Similar to the nanopores, scalloped sidewall profiles of the nanoscrews are created in the Bosch process and so is the discrepancy of neighboring screw heights. The apparent naked eye colors of the silicon nanoscrew surface range from dark blue (nanoscrew height 550 nm), dark violet (nanoscrew height 800 nm), and black (nanoscrew height 1300 nm). We attribute the stronger diffuse reflection of the blue and violet light (Fig. 2.20) to the stronger optical scattering at shorter wavelengths. The light trapping efficiency can be improved by increasing the nanoscrew height. The diffuse reflectance may be suppressed even down to less than 2.2% in the entire visible wavelengths, as seen in the case for 1300 nm high nanoscrews. The sharp tip and tapered profile of the nanoscrews enables the matching of optical refractive index between air and Si, hence reducing reflections by enhancing the light transmission at the interface [40]. Enhanced scattering would occur in both nanopore and nanoscrew. The two mechanisms for the optical characteristics are shown in

Fig. 2.21. Additional experiments with thin films will be performed in the future to verify whether the nanoscrew layer enhances optical transmission into the underlying Si or absorbs the majority of incoming light.

2.6 Conclusion

In summary, we have demonstrated a controlled fabrication of both nanopore and graded refractive-index nanoscrews with the same AAO mask. We have applied this technique in the demonstration of nanopores and nanoscrews of desired dimensions. The reduced specular and diffuse reflection reflectance of both nanopores and nanoscrews has been observed, confirming the extremely effective antireflection and light trapping function of the nanoscrew substrate. Integration of these nanostructures with each other on planar Si substrate surface has been presented. The approach from this section will be applied to devices that would benefit from better photon trapping such as photochemical reaction substrates.

2.7 Figures

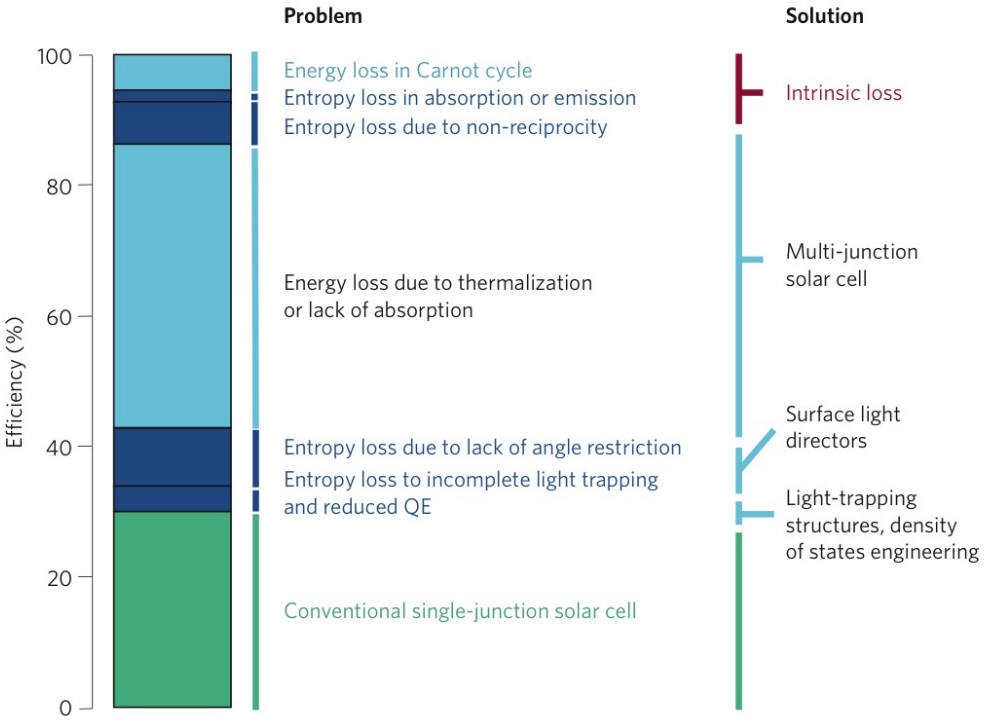

Figure 2.1: Possible sources of loss in solar cells. Dark blue loss is due to entropy while the light blue regions show energy losses. This shows that the main loss is due to thermalization and lack of absorption [1].

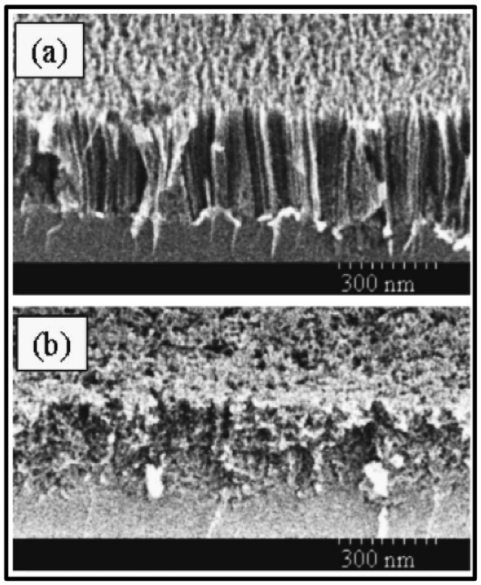

Figure 2.2: Metal-assisted wet chemical etching of porous Si by Au assisted HF/H_2O_2 etch for 30 seconds. The SEM images are 30° tilted from normal incidence. (a) Au assisted etch are for p+ doped Si. (b) p+ doped Si in HF/H_2O_2 etch without Au. (c) Lightly p doped Si in HF/H_2O_2 etch without Au [17].

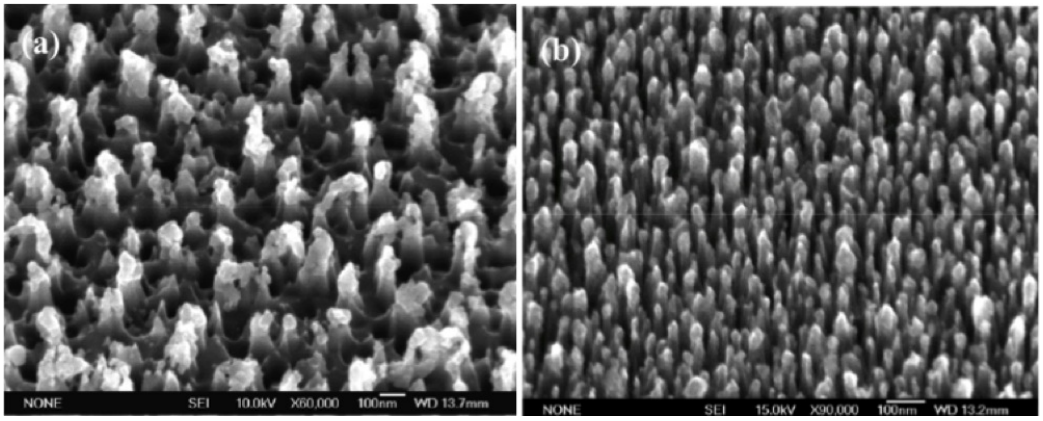

Figure 2.3: Reactive ionic etching (RIE) based nanostructure fabrication by utilization of rapid thermal annealed (RTA) metal etching mask. (a) and (b) Resulting pillars under different etching conditions [20].

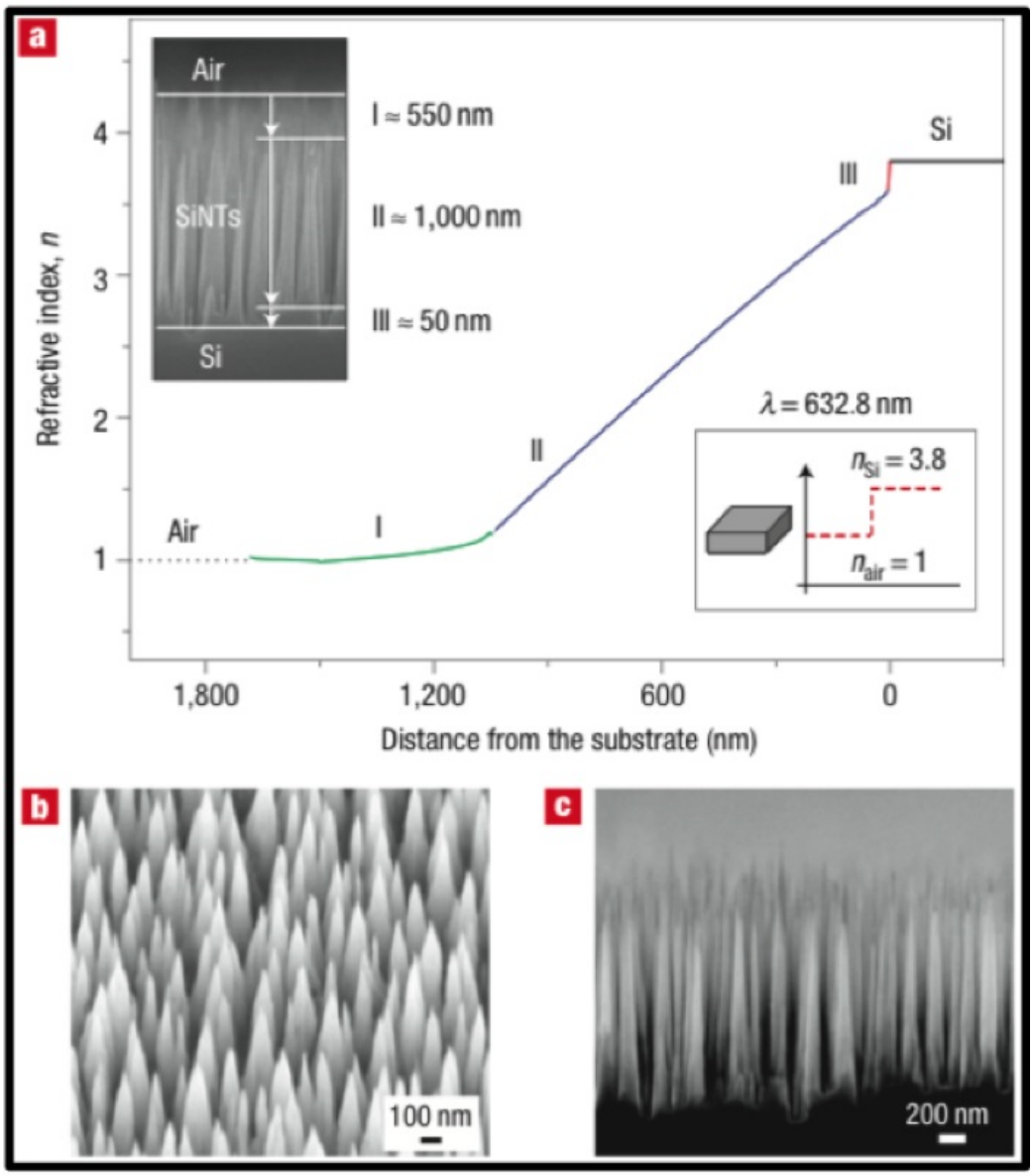

Figure 2.4: RIE based approach for simultaneous masking and etching. The gas composition in the RIE chamber enables a chemical reaction to form in situ nanomasks on the substrate surface that is then etched simultaneously [22].

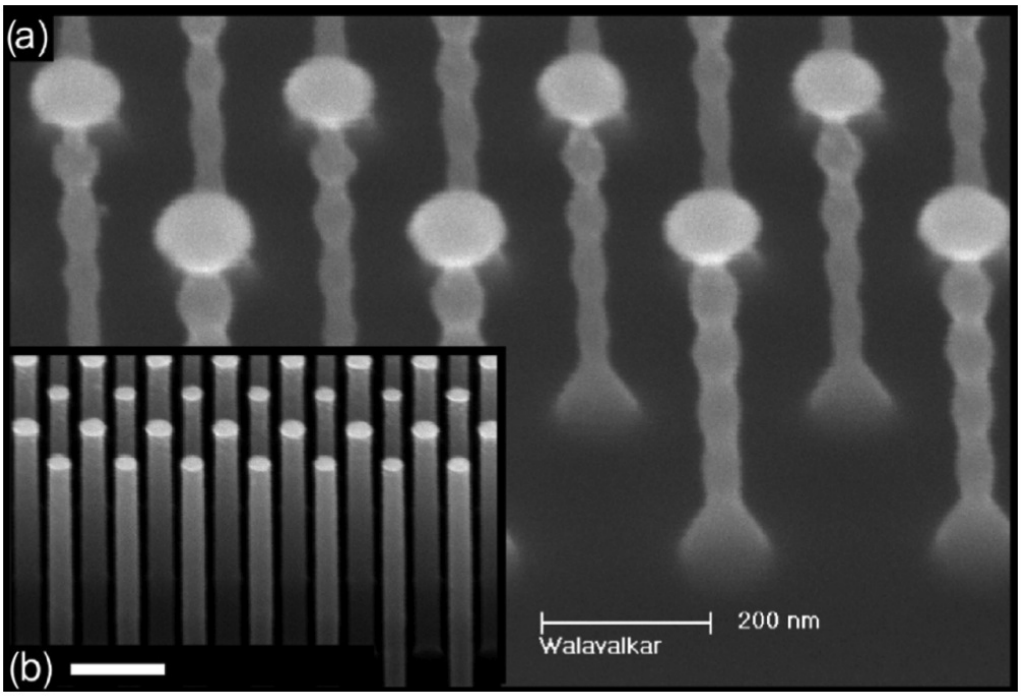

Figure 2.5: Ordered structures have been fabricated by the use of e-beam lithography. The rippled features on the sidewalls are due to the repeated etch-passivation of the Bosch process [28].

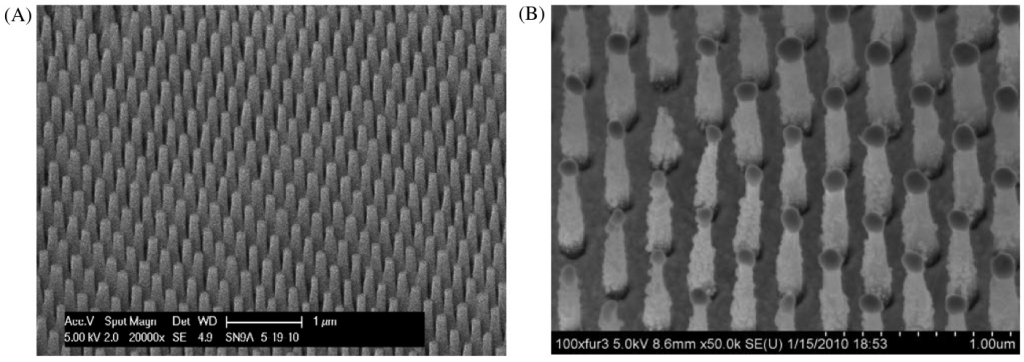

Figure 2.6: Ordered nanopillars fabricated by interference lithography followed by RIE. SEM images have been tilted 25°. The pillars in image (b) have 80 nm of Ag deposited on top [29].

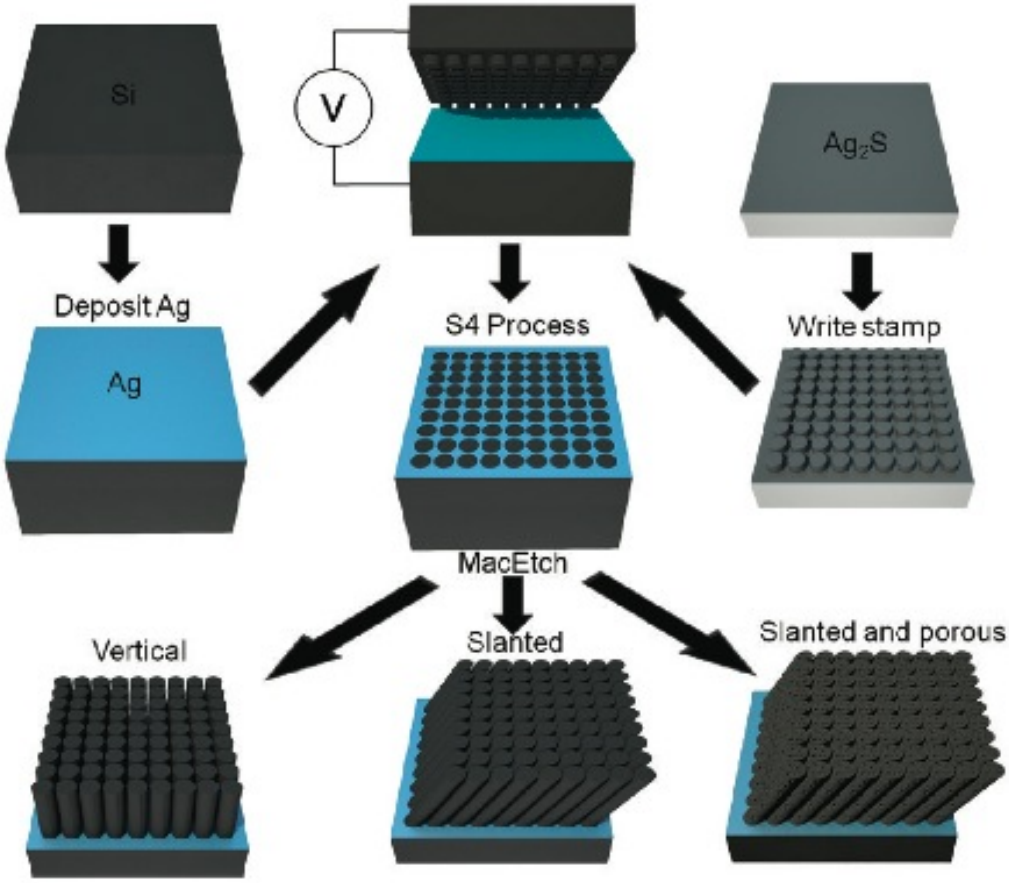

Figure 2.7: Flow chart showing fabrication of nanostructures with superionic solid state stamping followed by metal assisted chemical etching [32].

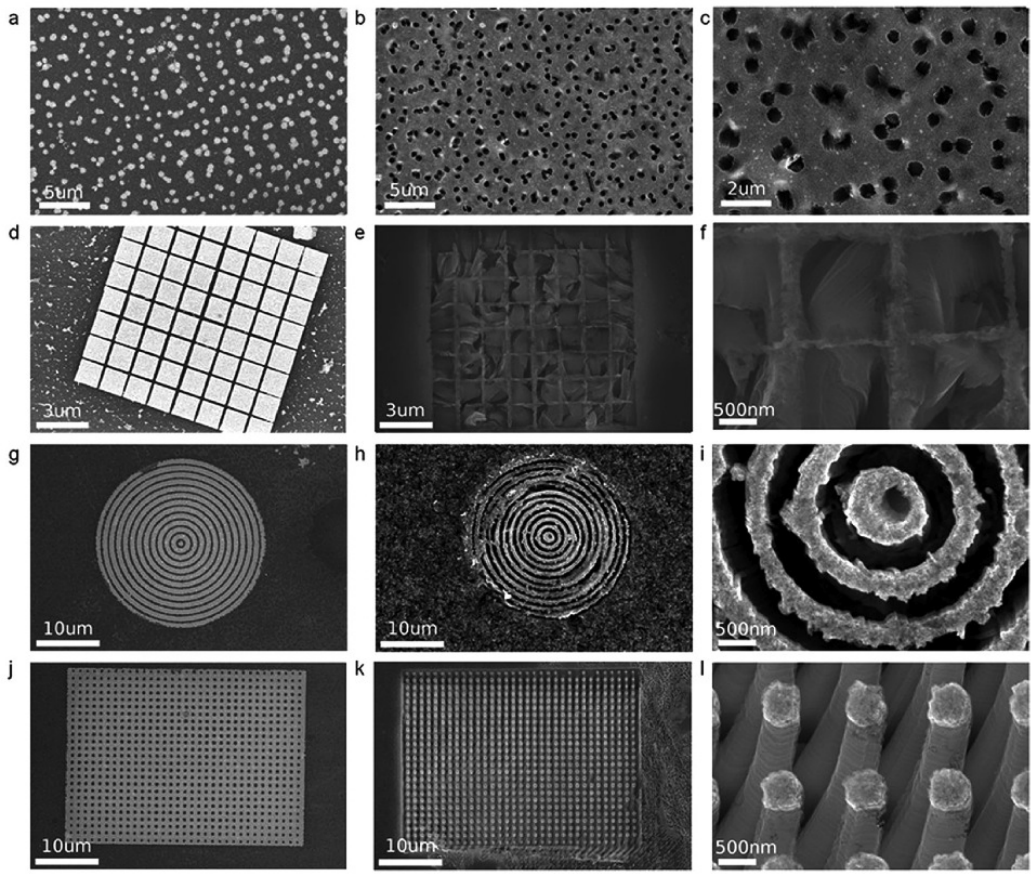

Figure 2.8: SEM images showing resulting features fabricated by superionic solid state stamping followed by metal assisted chemical etching [32].

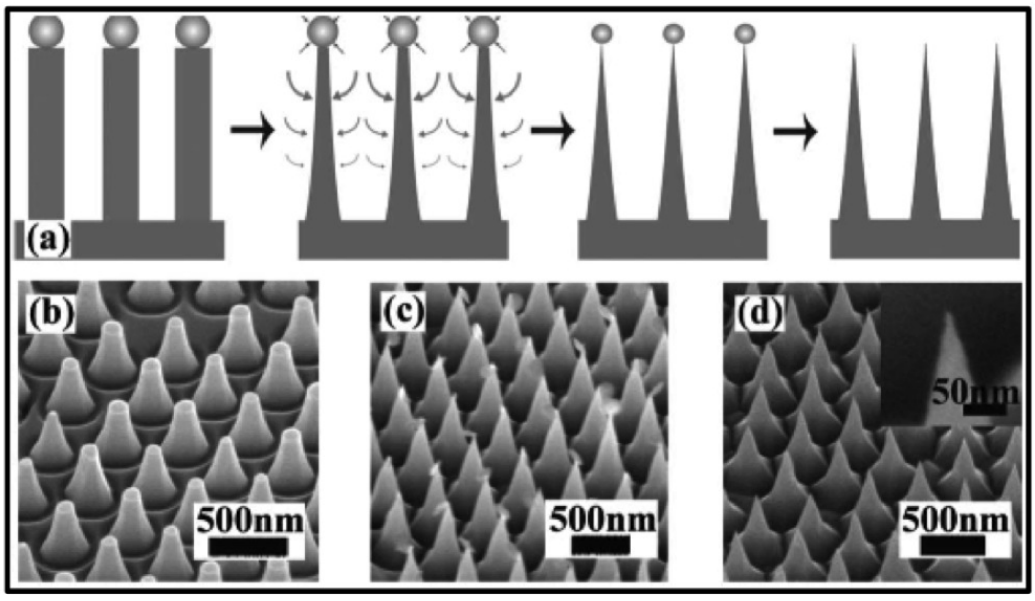

Figure 2.9: Nanosphere lithography followed by RIE for nanopillar or tapered pillar [33].

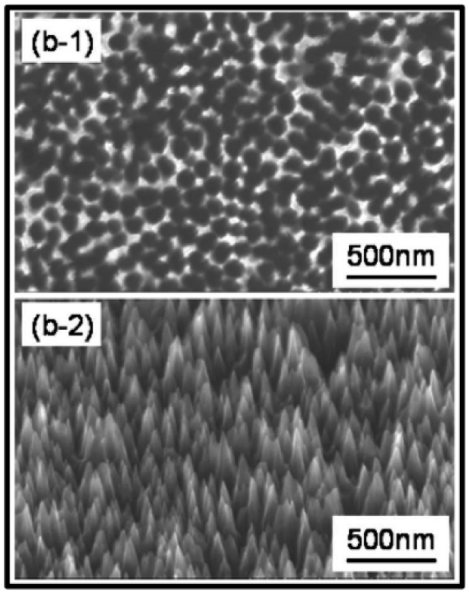

Figure 2.10: Anodized aluminum oxide (AAO) masking followed by RIE [35].

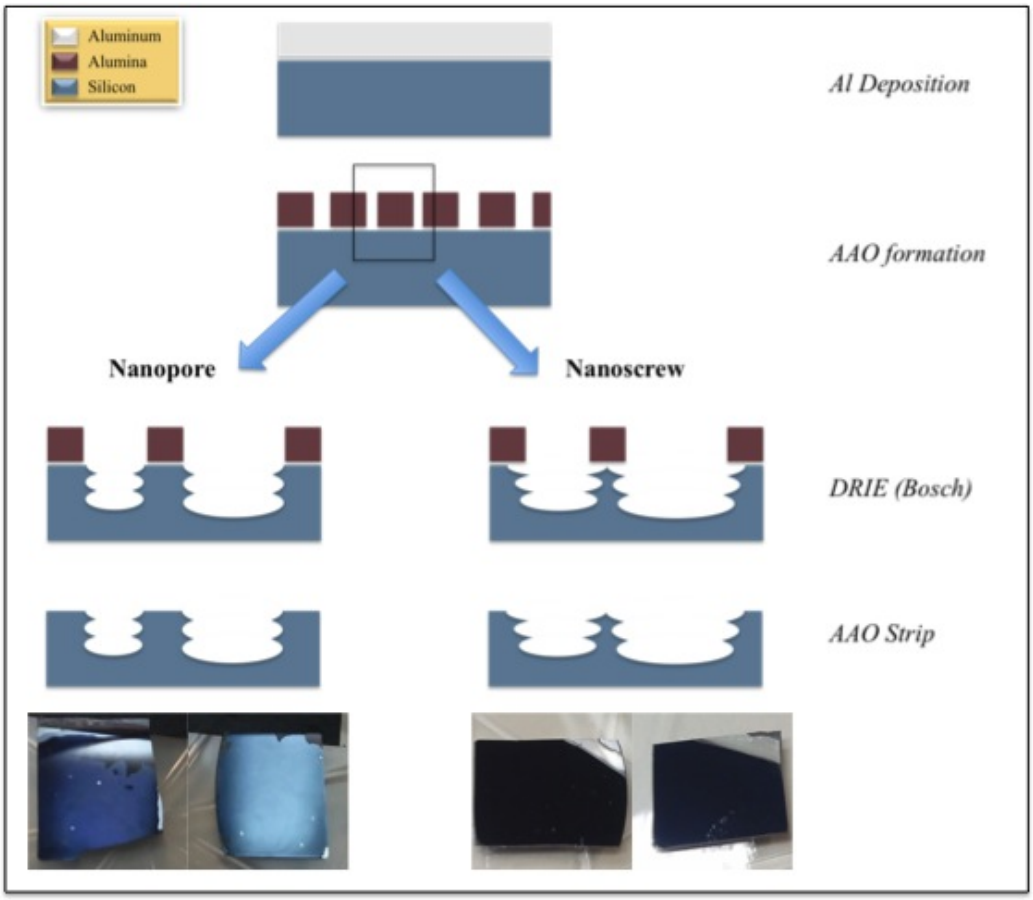

Figure 2.11: Schematic showing the fabrication flow of nanopore and nanoscrew based on Bosch process on anodized aluminum oxidation mask [41].

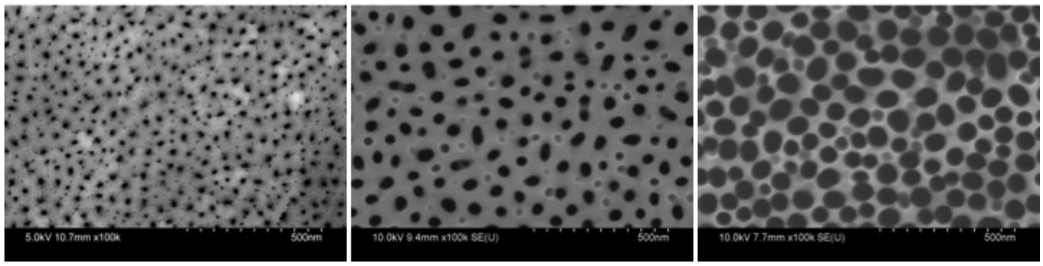

Figure 2.12: SEM images showing the AAO film resulting from anodization of Al in oxalic acid solution for self formed nanopore alumina. The parameters of interest are applied voltage, oxalic acid concentration, and anodization time.

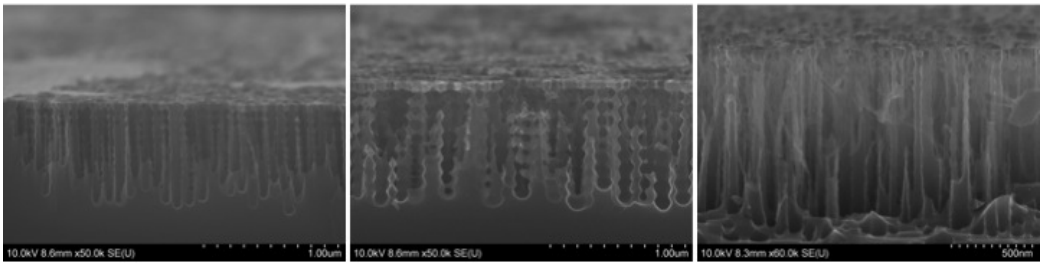

Figure 2.13: Cross sectional SEM images showing the etching result from DRIE based Bosch process. The same AAO mask has been used for the three samples. The parameters of interest are the passivation and etching conditions including time, inductive coil power, and applied DC voltage.

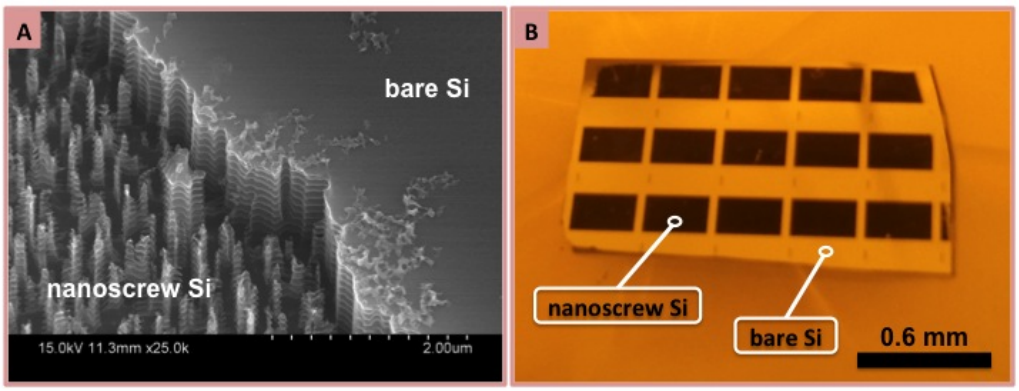

Figure 2.14: Images of integration of nanoscrew with planar Si. (a) 30 degree tilted SEM images. (b) Macroscopic image of the integrated device [41].

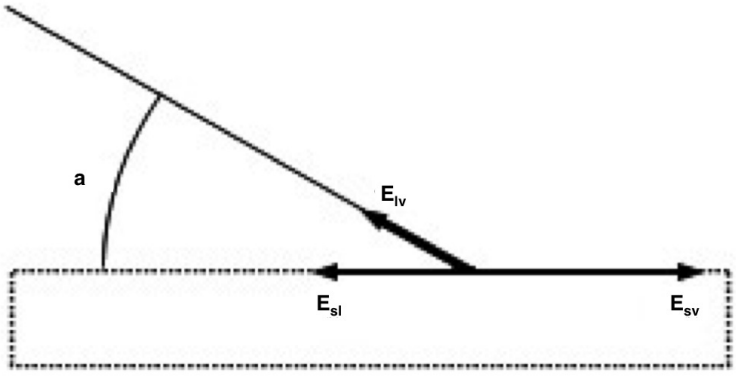

Figure 2.15: Balance of interfacial energy of water droplet on rigid surface [37].

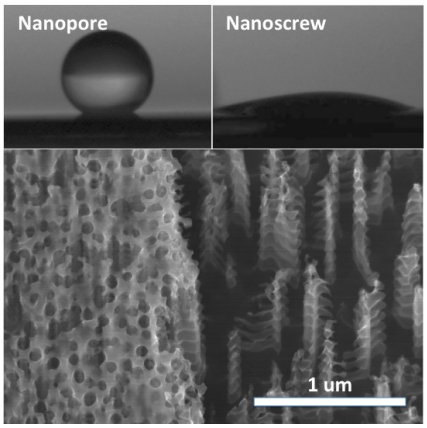

Figure 2.16: Contact angle images of nanopore (top left) and nanoscrew (top right) with 3 μL of water. SEM image (bottom) showing both nanopore and nanoscrew integrated on a single substrate [42].

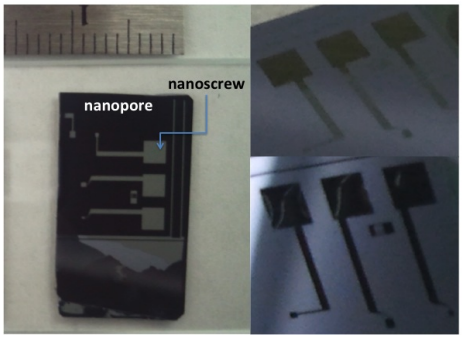

Figure 2.17: Image of nanoscrew integrated with shallow nanopores with ruler in cm scale (left). Image of sample with water dropped within channel on flat (top right) and tilted (bottom right) view [42].

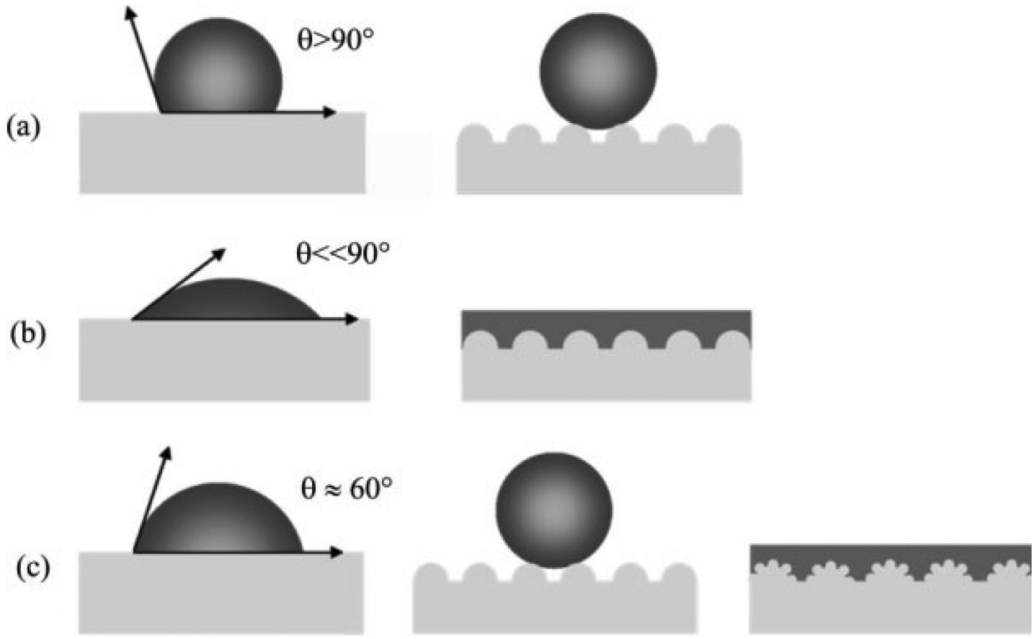

Figure 2.18: The relationship between nanostructures and surface hydrophobicity. (a) Originally hydrophobic materials enhance the hydrophobicity with nanostructures. (b) Originally hydrophilic materials enhance the surface wettability with nanostructures. (c) Extreme hydrophilic surfaces are obtained with highly roughened surface [39].

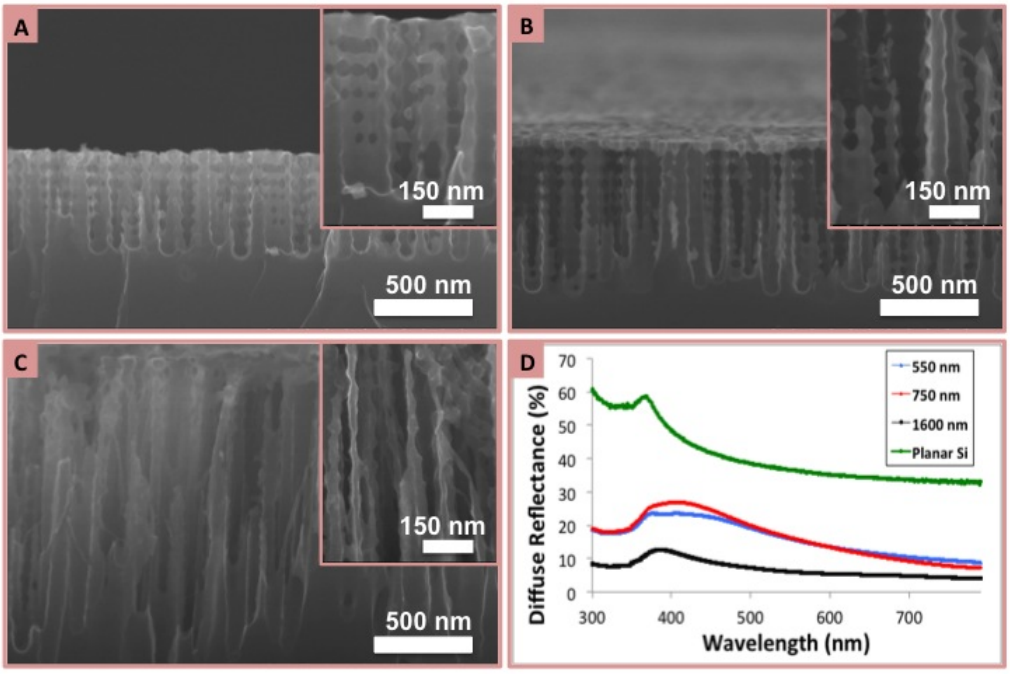

Figure 2.19: SEM images of nanopore Si for (a) 550 nm depth, (b) 750 nm depth, and (c) 1600 nm depth. Optical data for diffuse reflectance is presented in (d) [41].

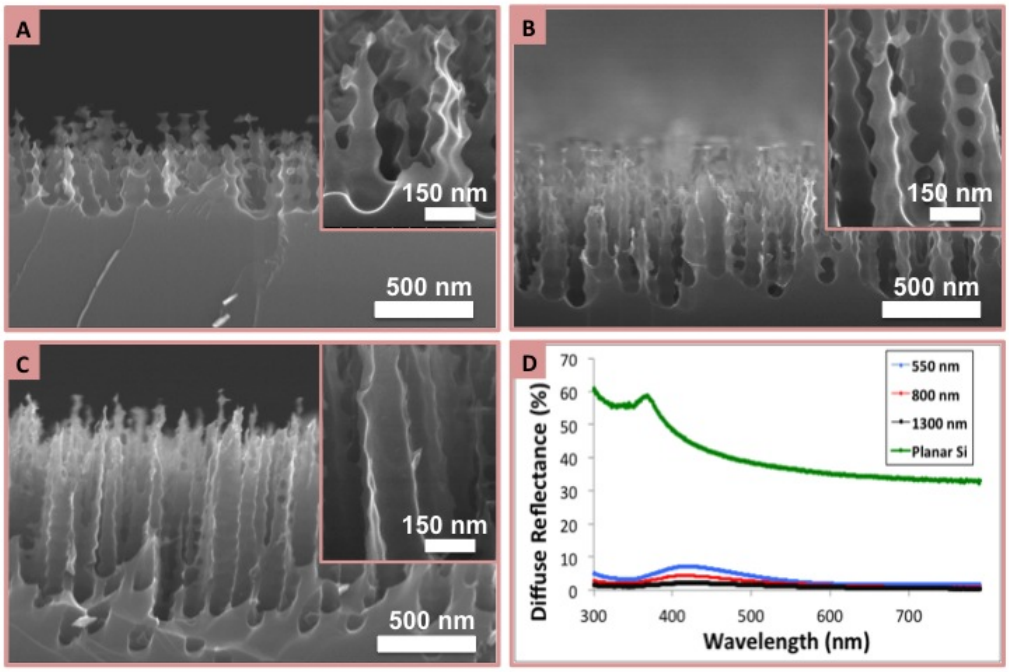

Figure 2.20: SEM images of nanoscrew Si for (a) 550 nm depth, (b) 800 nm depth, and (c) 1300 nm depth. (d) Optical diffuse reflectance of Si nanoscrew [41].

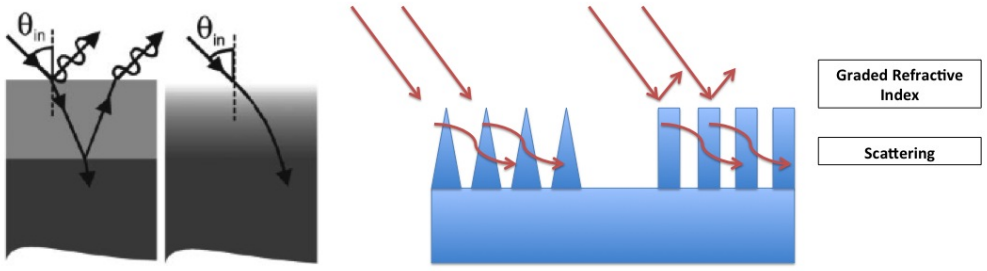

Figure 2.21: Schematic on the left showing the concept of graded refractive index [19]. Overview image on the right shows how optical characteristics of graded and abrupt structures would differ from each other due to graded refractive index. It would be a common attribute to have increased scattering within the nanostructures.

CHAPTER 3

RAPID PHOTOCHEMICAL REACTIONS ON NANOSCREW SILICON

The highly optically absorbent nanoscrew Si surface discussed in previous chapters opens the possibility toward converting sun light into energy. While the direct conversion would lead to the research in photovoltaics, we have been interested in other types of applications. Specifically, we have searched for possibilities toward utilizing the nanoscrew Si for applications toward photochemical reactions. The excited electron-hole pair will be injected into the electrolyte of interest, in which reduction or oxidation may occur. This would provide means of photocatalytic devices that utilize direction injection of carriers rather than inducing additional thermal energy.

The outline of this chapter is as follows: Section 3.1 introduces the readers to the motivation behind rapid photochemical reactions, particularly towards nanoparticle fabrication. Section 3.2 introduces the fabrication of Ag nanoparticles on planar substrate by thermal dewetting. Control experiments are conducted on this substrate to illustrate the overview of the redox Ag transformation reaction. The chemical redox reaction on nanoscrew Si device is demonstrated in Section 3.3. The mechanism of the nanoscrew Si chemical redox reactions is modeled in Section 3.4, with conclusions in Section 3.5.

3.1 Motivation for photochemical metal nanoparticle synthesis

Noble metallic nanoparticles have sparked interest in numerous scientific industrial communities as a universal nanomaterial. A key characteristic of nanoparticles derives from their interaction with light. Optical illumination with proper wavelength excites the collective oscillation of electrons in the interface between metal nanoparticles and the dielectric surrounding; such a phenomenon is defined as localized surface plasmon resonance (LSPR). The

LSPR effect results in local E field enhancements and fluorophore emission rate increase, enabling enhancements in applications such as fluorescence label detection [43, 44, 45], surface enhanced Raman scattering [7, 46], plasmon resonance based refractive index sensing [47, 48, 49], photodetection [50] and DNA detection [51]. With the mechanism originating from the collective oscillation of charge, the morphology of the metal nanoparticle attributes strongly to the LSPR conditions. Hence the controlled, cost effective fabrication of such nanostructures is of key in the adaptation of this technology for practical applications.

Methods to strategically place metal nanoparticles in certain locations and to mold them into particular physical shapes have benefited the diverse applications above. Recent studies have suggested that some metallic nanoparticles such as silver nanoparticles are much less structurally and chemically stable in comparison with the continuous metal thin film and bulk metal when exposed to water, oxygen and heat [52, 53, 54]. This relative instability has been utilized in previously reported efforts on structural transformation from spherical colloidal to prism shapes [55, 56, 57] and hollowing of noble metal nanoparticles [58]. The structural transformation of metallic nanoparticles in solution is due to nanoscale metal ionization and reduction processes. Ionization is understood to be due to surface oxidation of Ag nanoparticles in the presence of ambient oxygen and water [52]. The reduction reaction is achieved by two approaches, which are thermal and photochemical [55]. However, both reactions require various chemical treatment and long reaction time, preventing cost-effective scaling of metal nanoparticle synthesis. The thermal method requires various steps of chemical treatment to overcome the activation energy to achieve higher yield rate [55, 56], whereas photochemical approach based on plasmonic excitations still require tens of hours for the reaction to complete and bis(p-sulfonatophenyl)phenylphosphine dipotassium salt (BSPP) as a particle stabilization agent [55, 56, 57]. The disadvantages of specific chemical treatment requirement as well as tens of hours required for reaction completion hinder the rapid material synthesis.

Herein, we have demonstrated a rapid photochemical reaction substrate that completes such metal nanoparticle transformation reaction cycle within 5 minutes. By utilization of a special sharp-tip Si nanostructured device we call a nanoscrew, we show that noble metal nanoparticles may be structurally transformed through fast ionization and reduction with only pure water and

room light illumination. We have also demonstrated direct rapid reduction of ions in metal electrolyte into metal nanoparticles, drastically reducing the reaction time required in comparison to conventional synthesis approaches. The results shown in these sets of experiments provide the basis of utilizing the same substrate towards other photocatalytic applications such as water splitting [59, 60, 61, 62, 63] and ethylene epoxidation [64].

The optically illuminated Si nanoscrew device surface dramatically enhances the catalytic redox reaction in water leading to the rapid dissolving of predeposited Ag nanoparticle thin film and the transformation into prism shaped Ag nanoparticles. Previous reports [52, 53, 54] in the literature confirming this transformational reaction required time scales of 1 day [53] to 1 week [52] in room temperature. The prism shaped nanoparticle growth matches with the results from previous photocatalytic approaches [55, 57]. It has been suggested that plasmonic effects of the silver nanoparticles dominate such catalytic reactions [55, 57, 64]. However, additional experiments on strong reduction of ionic metal solution in absence of metal seeds provide insight into different mechanism. Besides Ag nanoparticles, we were also able to achieve growth of Au nanoparticles on Si nanoscrew device directly from the reduction of gold ionic solutions without adding additional reducing agents. From the evaluation of these two sets of experiments, it is shown that the mechanism behind the proposed device has additional physics to what has been previously observed. Experimental results suggest that the quantum physical properties of the nanoscale semiconductor substrate contribute to the rapid chemical reaction we have observed.

3.2 Redox of Ag nanoparticles on planar surface

Prior to demonstration of the proposed rapid photochemical substrate, the equivalent experiment is conducted on planar Si substrate as a control experiment. This section will also describe the overall ionization-reduction chemical reaction cycle of Ag nanoparticle transformation. Unless stated otherwise, device fabrication and characterization have been conducted within the Micro and Nanotechnology Laboratory in the University of Illinois at Urbana-Champaign.

Randomly isolated Ag nanoparticles are prepared on planar Si by thermal

dewetting, as shown in Fig. 3.1. The silicon wafer is cleaned by piranha etch to ensure there are no organic residues on the surface. Electron beam evaporator (CHA ebeam evaporator) is used to deposit 10 nm Ag film on the prepared silicon substrate. The metal deposited Si wafer is then subjected to rapid thermal annealing by Jipelec Rapid Thermal Processer. Thermal capillary wave is applied to the Ag thin film by the injected thermal energy. The wavelength of the wave depends on the thickness of the metal layer and the surface tension between two materials [24]. With enough energy, selected areas of the substrate with high amplitude will break the metal thin film and form isolated metal particles.

With the thermal dewetted nanoparticle substrate, deionized Millipore water and moderate heat are applied for Ag transformation experiments. The overall reaction is illustrated in Fig. 3.2. Isolated Ag nanoparticles in contact with water on Si substrate are ionized by oxidation of the metal surface in an oxygen rich environment. The Ag ions cause the deionized water to become an electrolyte, which is then subjected to reduction to form new Ag nanoparticles in the proximity of the original nanoparticle location. Previous reports in the literature have confirmed this reaction in time scales of 1 day [53] to 1 week [52] in room temperature. In our control experiment with Ag nanoparticles on planar Si prepared by thermal dewetting of thin film Ag, we have observed that Ag nanoparticles have begun to form a thin film in the proximity of the original location after two hours in water heated at 60 ^{o}C.

3.3 Photochemical redox of Ag nanoparticles on nanoscrew Si

The same experiment is conducted on the nanoscrew Si surface to confirm the rapid photochemical capability. To conduct the photochemical redox experiment of Ag nanoparticles, Ag deposition has been carried out by e-beam evaporation. Due to the tapered, pillar structure with periodic indentations, a single step top-down metal evaporation results in the formation of metal nanoparticles along the sidewall of the nanoscrew, as in Fig. 3.3.

The top-down deposited Ag thickness controls the size of the individual nanoparticles on the sidewall. The gaps between nanoparticles are controlled

by the periodicity of the scallops on the nanoscrew sidewall. The different schemes and corresponding characteristics for nanoparticle formation by simple, single-step ebeam evaporation will be illustrated in depth in Chapter 4.

The diffuse reflectance data for the nanoscrew alongside with that of the case after 200 nm Ag deposition are illustrated (Fig. 3.4). The slight dip around 500 nm for the Ag coated nanoscrew is assumed to be due to the localized surface plasmonic resonance mode that is excited due to closely packed Si nanoparticles. Such optical reflectance data will serve as means to characterize the apparent surface color change with the occurrence of transformational Ag nanoparticle redox reactions.

When the same conditions as the control experiment are applied, the proposed nanoscrew Si device decreases the required reaction time to less than 5 minutes. More interestingly, it enables a new reaction that leads to rapid transformational growth of prism-shaped Ag nanoparticles on n-type nanostructured Si surface as shown in Fig. 3.5.

Water is dropped on the nanostructured Si surface that has vertically packed Ag nanoparticles. The only condition for the rapid nanoparticle transformation is that heat of 60 °C is applied to the substrate under room light illumination. Upon the evaporation of the water droplet, the color of the nanostructured Si substrate surface changes, as seen in Fig. 3.6. A control experiment that has eliminated water, heat, and light has been conducted as in Fig. 3.5 and 3.6. The results indicate that water and heat are required for the drastic color change of the surface. Light has not been as strong a factor in terms of the apparent color change of the surface (Fig. 3.6). However, SEM examination in Fig. 3.5 reveals that light does play a critical role in the shape of the nanostructures. Water and heat enable the merging of local Ag nanoparticles in proximity with each other by rapid oxidation and weak reduction. Transformational Ag prism growth is only observed when room lighting illuminates the sample, indicating light is required for rapid reduction of metal ions.

Another factor of interest that affects such prism growth is the doping type of the nanoscre Si. The same Ag nanoparticle transformation experiment has been conducted on p-type nanoscrew Si, as seen in Fig. 3.7. Unlike n-type, the results suggest dispersed reduction of Ag ions. Hence, the transformed Ag nanoparticles are developed along the sidewall of the p-type Si nanoscrew instead of the very tip focused, prism shape for the n-type substrate case.

This difference between the two differently doped substrates will be discussed in Section 3.3 of this chapter.

The sidewall SEM images with in-situ XPS data in Fig. 3.8 confirm that there is no change in the material composition between the different conditions tested. The original substrate contains the same Ag compound composition at the tips of the Si nanostructure as with the transformed nanoprism case. It is confirmed that the prism is not a type of salt, but rather Ag nanoprisms that have been grown.

It is essential to describe the unique properties of the special silicon substrate at hand to understand the mechanism of the prism growth. Two key attributes of this device we have called a nanoscrew are the structurally repeated side hinges and the very sharp tips [41]. The repeated side hinges enable the device to form vertically close-packed metal nanoparticles with just a single metal evaporation step. The evaporated metal forms a discontinuous film along the nanoscrew sidewall surface. A proper thickness of metal deposition results in a substrate with vertically packed metal nanoparticles. But more importantly, such structure provides increased light scattering cross section, as discussed in Chapter 1. The strong antireflection property of the silicon nanoscrews exhibits lower than 2% diffuse reflectance for the visible wavelengths [41]. This enables the silicon nanoscrew structures to efficiently absorb light and create a high population of excitons in comparison to a planer Si device.

3.4 Analysis of photochemical reaction mechanism

The attributes of the nanoscrew provide insight into the mechanism behind the rapid photochemical reaction we observed. The increased surface area of the individual nanoparticles will allow the efficient release of Ag ions by thermal oxidation. Then the ions will undergo reduction in proximity of the originated nanoparticle. This will promote the change in shape of the individual nanoparticles as well as the merging of those close enough to each other. For the case room light is also applied to the substrate, which causes the Ag prism growth, there is a subtle difference in the oxidation step. It has been discussed of catalytic oxidation reactions by Ag nanostructures [64]. Hence oxidation processes may be accelerated with light illumination,

promoting stronger release of Ag ions. The reduction of the Ag ions back to Ag deposits on silicon surface is also strongly affected by the substrate. Due to the high photon absorption by the Si nanoscrew substrate, a high population of electron hole pairs is provided to the semiconductor-electrolyte interface. This in turn creates preferred redox sites along specific regions of the Si nanoscrew surface. For the case of the n-type Si nanoscrew substrate we have used, it would be later found that the tip region of the nanoscrew is the preferred redox site, hence where the strong amount of prism growth occurs.

To provide a deeper insight into the reduction mechanism of the Ag prism growth, we model the Si nanoscrew structure in contact with the electrolyte as a photochemical diode. The concept is to model a semiconductor-electrolyte electrical contact as Schottky barrier [65, 66, 67, 68]. Applying this model in our system of interest describes the exciton movement at the Si-electrolyte interface, as in Fig. 3.9. The key factor of consideration for this model is that the physical dimension of the Si nanoscrew in the lateral plane decreases towards the tip. This will force the energy band of the nanoscrew tip to form relatively thin Schottky barriers in comparison to that of the physically thicker base region.

With the energy band diagram of our model, we can now explain the high-level electron injection into the Si nanoscrew tip for the n-type Si case. Diffusion and drift, the two main charged carrier transport mechanisms, play different roles in the functionality of this system. Optical illumination on the n-type Si nanoscrew generates a high population of excitons. In a volumetric sense and from analysis of optical absorption for various Si nanoscrew heights [41], more excitons are generated towards the wider and larger base of the nanostructure in comparison with the thinner and sharper tip. Hence diffusion of majority carriers would favor the direction towards the tip of the nanostructure. In another competing transport process, the excitons will follow the drift current direction along the bending of the energy band diagram. However, such band bending in the proposed silicon nanostructures only occurs strongly in the direction away from the semiconductor-electrolyte interface. When we define the normal vector of the interface as the horizontal plane, drift will not have strong effect in the vertical direction. Hence, the majority carrier diffusion will dominate the carrier transport vertically from the base of the silicon nanoscrew toward the tip direction. In the hori-

zontal view, electrons are trapped within the center of the Si nanoscrew due to electrolyte-Si Schottky barrier induced carrier drift. With diffusion contributing to the carrier transport in the vertical direction, drift is responsible for that in the lateral direction. This causes electrons to transport away from the semiconductor-electrolyte interface while holes are to inject into the electrolyte. It is only towards the tip region in which photoelectrons in silicon may be close enough to the interface with the electrolyte and participate in reduction reactions by tunneling.

Similar explanation may be applied for the p-type Si nanoscrew in Fig. 3.9. In this case, the electrolyte-Si Schottky barrier causes photoelectrons to be injected into the electrolyte rather than being focused towards the center. Hence the Ag ion reduction will occur along the entire sidewalls of the Si nanoscrew in a rather non-focused fashion. This is in alignment with experimental results for Ag reformation by p-type nanoscrew experiments (Fig. 3.7), where we are not able to find such profound Ag prism growth.

To confirm the above physical model of reduction on n-type and p-type Si nanoscrew, experimentation on Au reduction from gold chloride solution ($AuCl_3$, 99.99% from metal basis, diluted to 0.05 g Au in 1 L) is demonstrated. SEM images in Fig. 3.10 show the difference between the Au reductions from the two different types of Si. It is shown that the n-type Si nanoscrew has focused Au growth towards the tip of the device whereas the p-type case has dispersed growth along the sidewalls that have been exposed to the electrolyte. The comparison shown here for Au reduction as well as Ag prism growth confirms the proposed photochemical model. With the n-type Si nanoscrew, additional experiments on Au growth have been conducted. Three different dilutions, which are 0.05 g, 0.25 g, and 0.5 g of Au in 1 L, have been applied. The results in Fig. 3.10 demonstrate a simple approach in making nanoscale Au particles. By simple controlling the concentration of the applied electrolyte, we may grow different sized metal nanoparticles.

3.5 Conclusion

In conclusion, we have demonstrated a rapid photochemical reaction platform based on semiconductor nanostructures. By the utilization of a highly optical energy absorbent semiconductor substrate with subwavelength nanos-

tructures, we have been able to directly inject the excited charge carriers into ionic solutions for reduction of noble metals. Such reactions would have direct applications toward nanomaterial fabrication and photocatalytic chemistry. This would provide a uniform and localized growth method of metallic nanoparticles by simply applying a controlled concentration of ionic solution under room light illumination. Such highly reactive surfaces may also be applied to other fields of study such as enhancing photocatalytic water splitting and solar fuel. We anticipate that the platform will also applied to many other fields of study in chemical reactions.

3.6 Figures

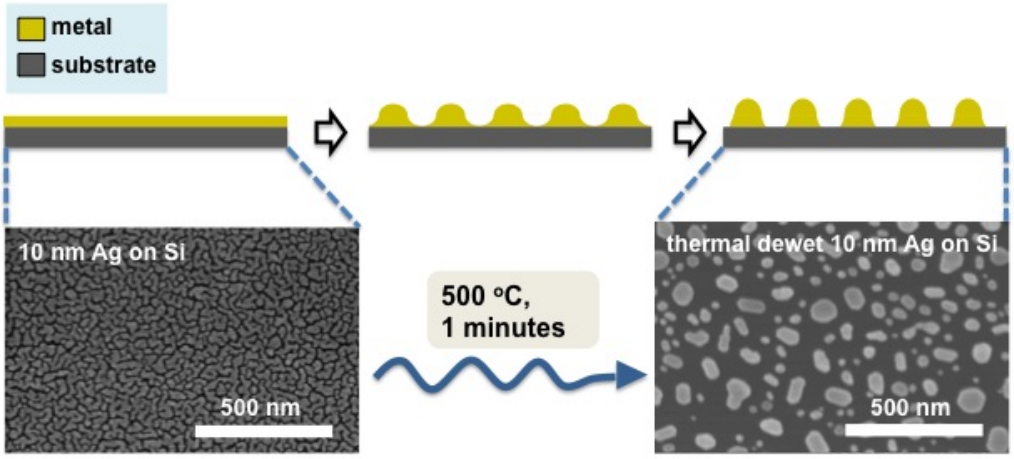

Figure 3.1: Ag nanoparticles are fabricated on planar Si by thermal dewetting.

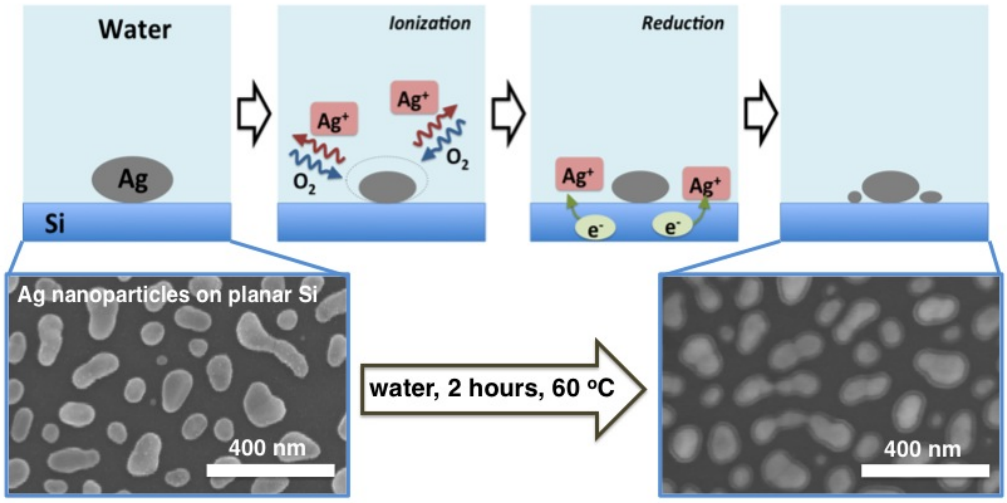

Figure 3.2: Overview of the ionization-reduction reaction sequence of Ag nanoparticle transformation with demonstration on planar Si surface as control experiment in comparison to Si nanoscrew.

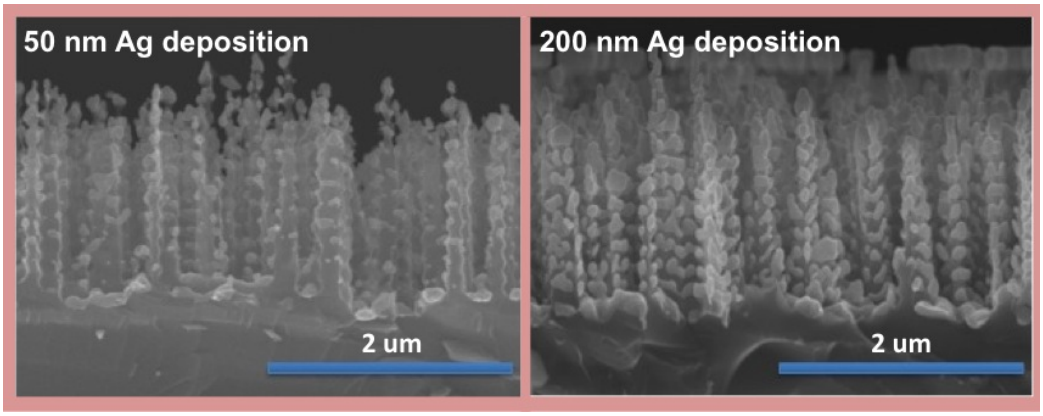

Figure 3.3: SEM images of Ag deposition on nanoscrew for 50 nm (left) and 200 nm (right) are illustrated.

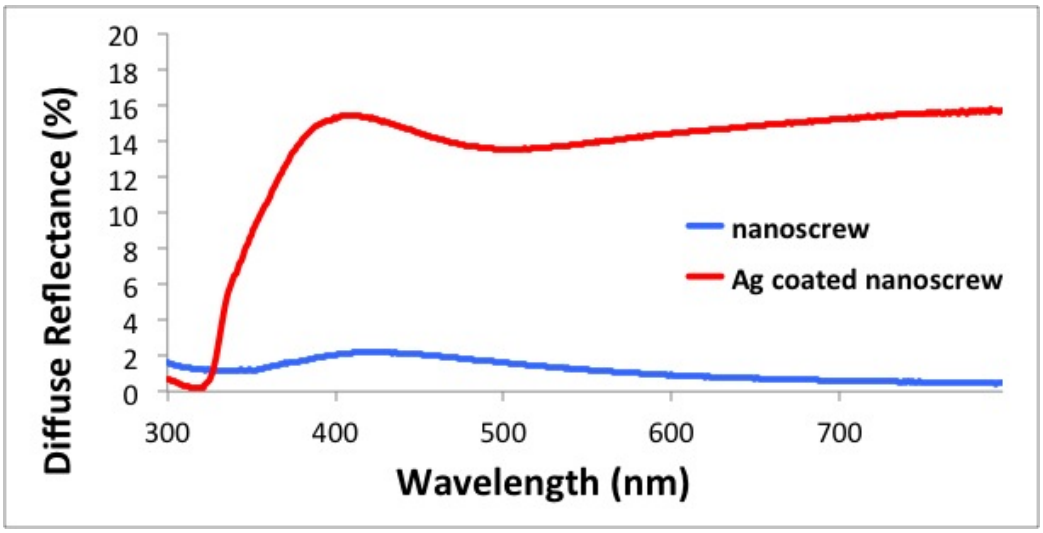

Figure 3.4: The diffuse reflectance for nanoscrew and 200 nm Ag coated nanoscrew.

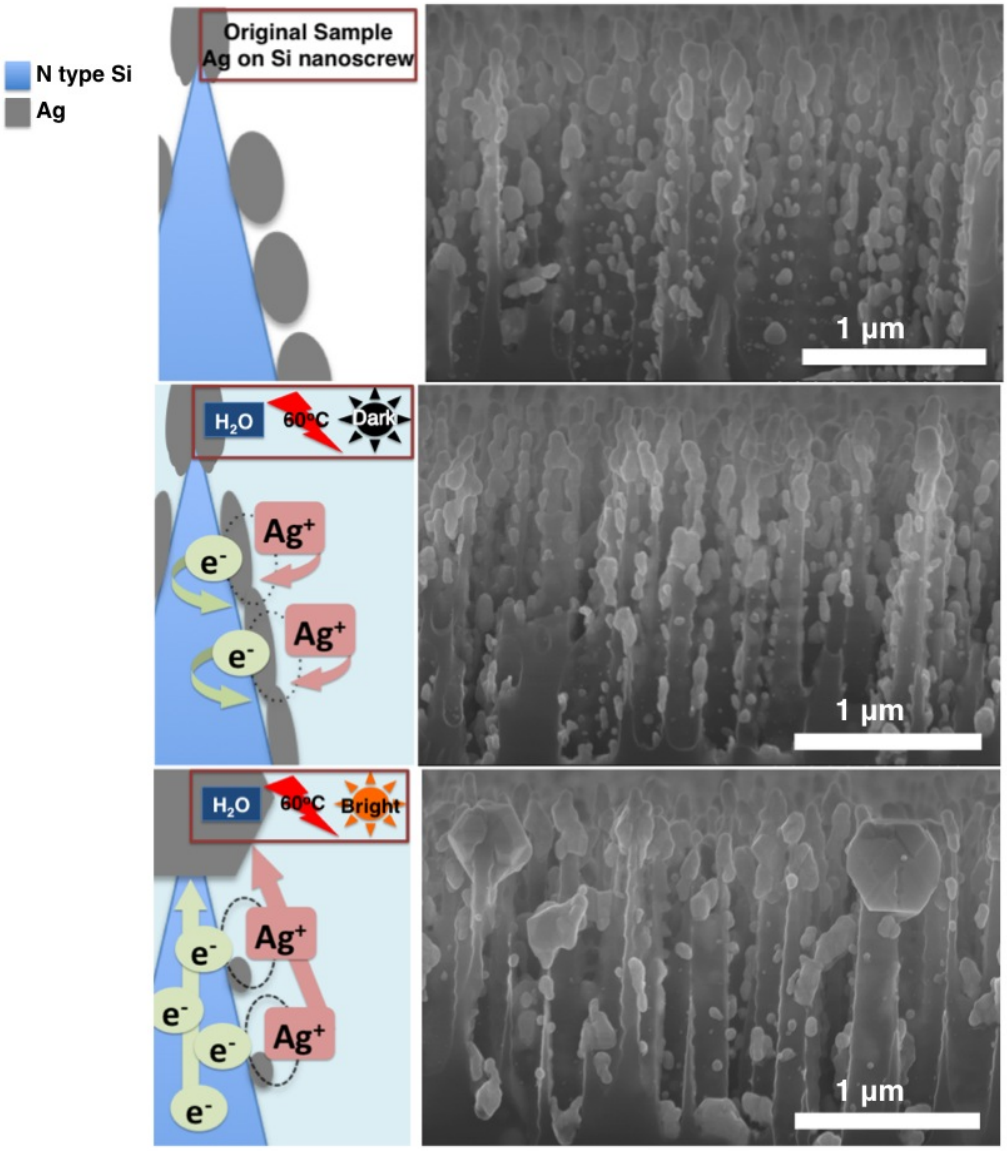

Figure 3.5: Schematic with the corresponding SEM images of proposed device. Experiments to confirm the effect of light on the redox rate have been conducted. Heat has been applied for enhanced oxidation of Ag particles to increase the release of Ag ions. Comparison between the dark room with ambient light condition confirms the photocatalytic effect on the redox reaction of the proposed device. All reactions have been completed within 5 minutes

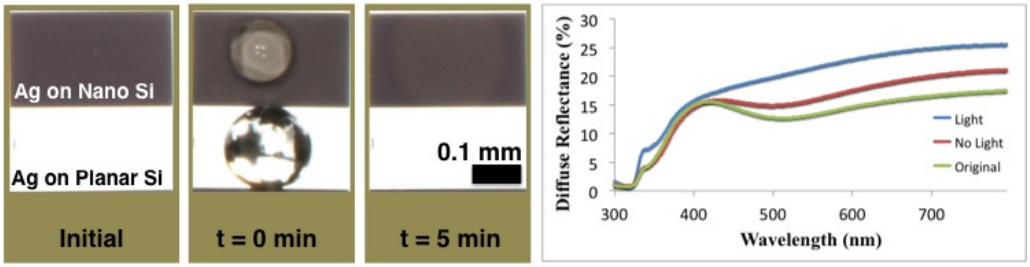

Figure 3.6: Macroscopic images showing the color changing effect of nanoparticle reformation in comparison to smooth Ag film on planar Si (left). Diffuse reflectance data of different Ag nanoparticle conditions. Original refers to the 200 nm Ag deposited Si nanoscrew. No Light refers to original after Ag transformation under water, 60 °C in dark room condition for 5 minutes. Light refers to original after Ag transformation under water, 60 °C in bright room condition for 5 minutes.

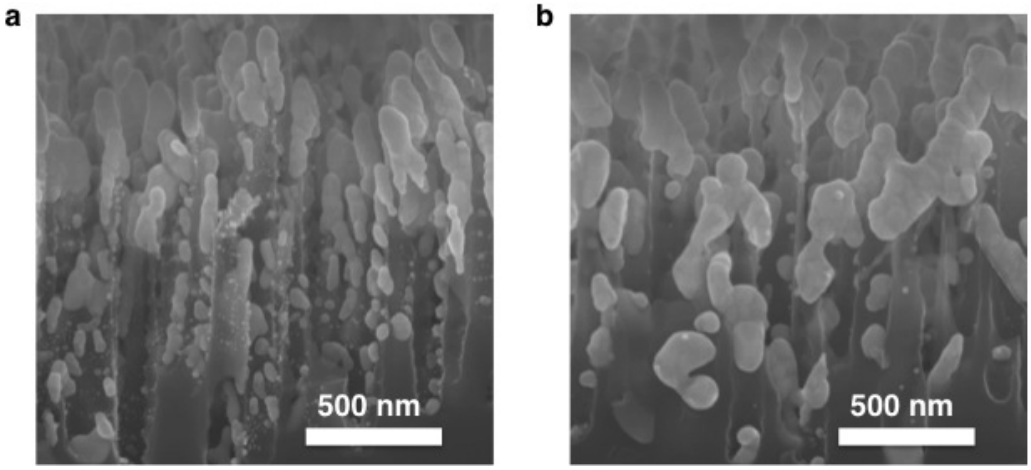

Figure 3.7: Ag transformation experiments on p-type Si nanoscrew. (a) SEM shows the initial state of p-type Si nanoscrew with 200 nm Ag deposition. (b) SEM showing Ag transformation on p-type Si nanoscrew for water, 60 °C in bright room condition for 5 minutes.

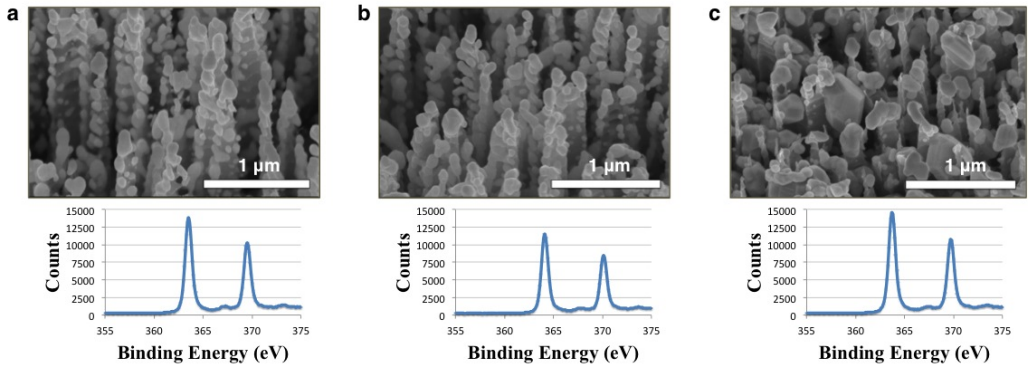

Figure 3.8: Verification of material composition by X-ray photoelectron spectroscopy. (a) SEM image of 30° tilted view and XPS data for original sample. (b) SEM image of 30° tilted view and XPS data for sample subjected to water, 60 °C in dark room condition for 5 minutes. (c) SEM image of 30° tilted view and XPS data for sample subjected to water, 60 °C in room light illumination for 5 minutes.

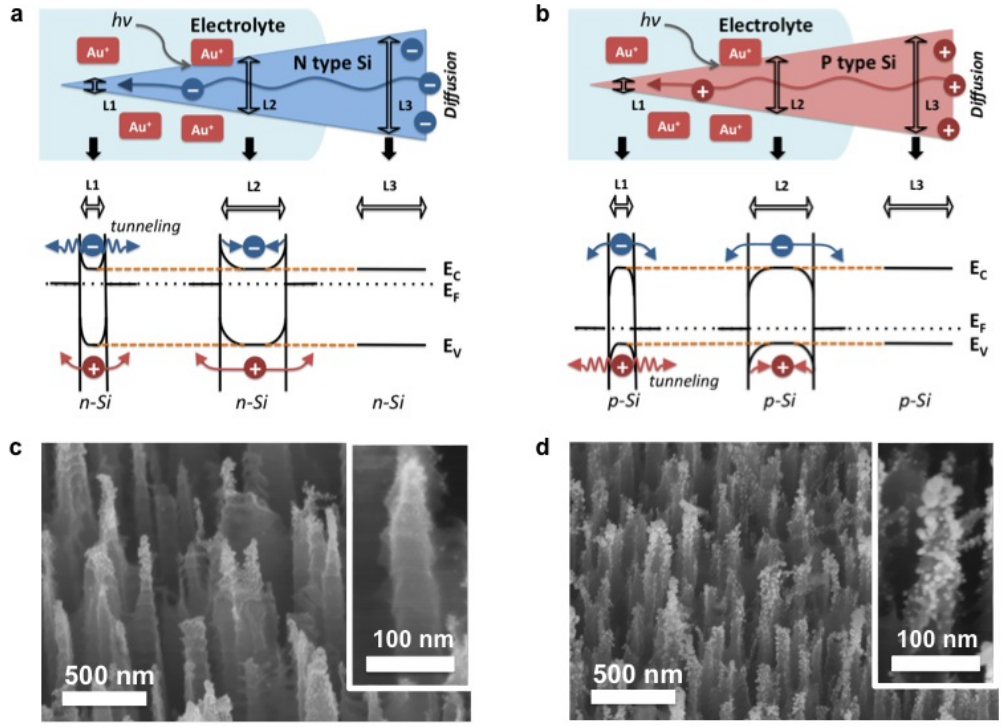

Figure 3.9: Mechanism for metal reduction on Si nanoscrew surface. Common experimental condition used for Au reduction was room light illumination, room temperature with reaction time of approximately 1 minute. (a) Energy band diagram showing movement of charged carriers for n type Si. (b) Energy band diagram showing movement of charged carriers for p type Si. (c) SEM image of Au nanoparticle on n-type Si nanoscrew by rapid reduction of 0.05 g/L $AuCl_3$ solution confirming confined reduction at tip. (d) SEM image of Au nanoparticle on n-type Si nanoscrew by rapid reduction of 0.05 g/L $AuCl_3$ solution confirming dispersed reduction along nanoscrew sidewall.

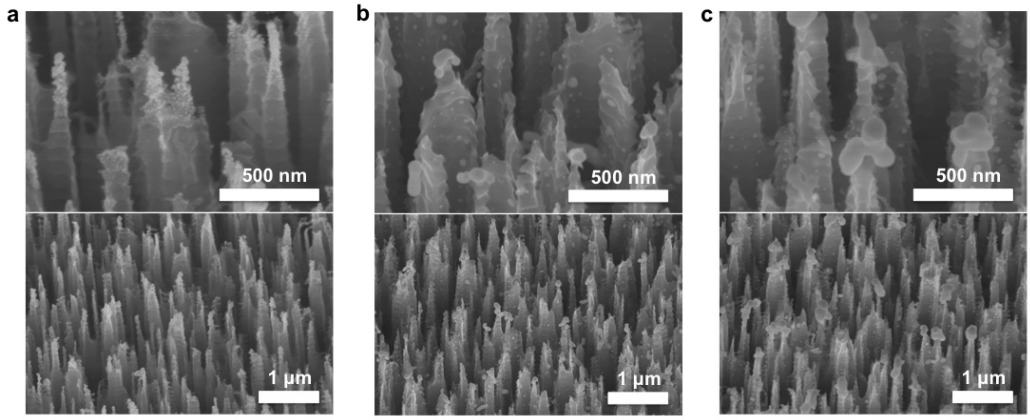

Figure 3.10: Demonstration of Au reduction in relation to concentration of applied $AuCl_3$ droplet on Si nanoscrew is shown. Common experimental condition used was room light illumination, room temperature with reaction time of approximately 1 minute. (a) Reduction of 0.05 g/L of $AuCl_3$ on n-type Si nanoscrew. (b) Reduction of 0.25 g/L of $AuCl_3$ on n-type Si nanoscrew. (c) Reduction of 0.5 g/L of $AuCl_3$ on n-type Si nanoscrew.

CHAPTER 4

3D LOCALIZED SURFACE PLASMON RESONANCE (LSPR) SUBSTRATE FOR OPTICAL BIOSENSING

In biosensing, the development of microfluidics, nanotechnology, and optics has enabled further understanding on the fundamentals of biosensors. The continued efforts to develop high throughput, high sensitivity, real time, and cost effective lab-on-chip systems is desired for rapid biosensing capabilities. This enables the detection of multiple biomolecules in a relatively short amount of time. Early diagnosis of diseases as well as the discovery of effective drugs may be achieved with such improvements. In particular, the utilization of localized surface plasmon resonance has enhanced highly sensitive detection methods such as fluorescence detection and surface enhanced Raman scattering (SERS). However, precise control of the localized surface plasmon resonance (LSPR) structures discussed in Chapter 1 has thus far been limited to planer surfaces [4]. This section will discuss the unique property of the proposed nanoscrew Si substrate and the demonstration towards a robust 3D LSPR substrate for fluorescence enhancement and SERS. Section 4.1 will introduce the concept of 3D nanostructures on the nanoscrew Si surface. Fluorescence enhancement measurements and SERS are demonstrated. Section 4.2 extends the concept into silicon nitride to replace Si as the substrate material. The chapter will close with ending remarks in Section 4.3.

4.1 Concept of 3D metallic nanostructures on nanoscrew Si

In comparison to 2D placement of nanoparticles, schemes to three-dimensionally pack metal nanoparticles would provide increased localized surface plasmonic resonance enhancement hot spots per planar area. While there still exists the issue of aligning the excitation light polarization with the plasmonic modes

for enhanced coupling, this approach would provide the basis for an enhanced LSPR platform. Previous schemes of fabricated 3D cavity nanoantenna for plasmonic applications have been based on rather random sidewall attachment of metal [69]. Herein we demonstrate a scheme for controlled sidewall deposition for 3D LSPR substrate.

4.1.1 Fabrication of 3D metallic nanostructures on nanoscrew Si

Sputtering and evaporation are the most common approaches for metallization in semiconductor devices. The impact energy from accelerating ions in sputtering gives the depositing metal more energy to redistribute, hence more sidewall profile coverage. On the other hand, thermal and ebeam evaporation is highly directional. There is very low deposition on the sidewall features, making evaporation preferable for planar electrical contact applications.

The proposed 3D LSPR structure utilizes this low sidewall coverage attribute of metal evaporation. While straight sidewalls would result in discrete deposition between different planar layers, tapered nanostructures would lead to continuous film deposition on sidewalls as well. If the tapered structure would have periodical grooves, the metal film deposited on the sidewalls will be discretized, forming isolated nanoparticles.

We have tested this concept of 3D metal nanoparticle formation on the nanopore and nanoscrew Si devices that were proposed in Chapter 2. The results in Fig. 4.1 show nanoparticle formation for nanopore and nanoscrew devices with same metal deposition thickness. The comparison shows preference of nanoscrew over nanopore. Note that the deposition thickness used throughout the paper would refer to that of planar deposition. Hence deposition of 50 nm Ag would mean that the evaporation step of interest would result in 50 nm thin films on planar structures, whereas the nanoparticles would have different thickness due to surface area condition change. Unless stated otherwise, device fabrication and characterization have been conducted within the cleanroom of the Micro and Nanotechnology Laboratory in the University of Illinois at Urbana-Champaign.

The side hinge structures of the nanoscrews provide local deposition sites for metals, enabling three-dimensional close-packed metallic nanoparticles.

The straight directionality of evaporation reduces sidewall coverage creating discrete nanoparticles. The interparticle distance, hence the LSPR hot spot gap, can be controlled by the nanoscrew groove periodicity and metal deposition thickness as seen in Fig. 4.1. The backbone nanostructure groove size, the tampered angle in relation to the original planer surface of the substrate and Ag deposition thickness determines the individual nanoparticle size and shape.

4.1.2 Surface enhanced Raman scattering and metal enhanced fluorescence on Si based 3D LSPR substrate

The 200 nm Ag deposited nanoscrew Si substrate has been examined for SERS measurement. The substrate SEM and data are shown in Fig. 4.2. The Renishawn Raman/PL Micro-spectroscopy System from the Micro and Nanotechnology Laboratory at the University of Illinois at Urbana-Champaign has been used for the Raman measurement. Rhodamine 6G is selected as the testing molecule of interest. Due to availability, 633 nm and 785 nm have been tested as the Raman excitation laser source. In comparison, the 633 nm laser resulted in higher Raman signal. This would result from the relative superior overlap of LSPR modes of the substrate with the 633 nm laser rather than 785 nm. With the laser excitation condition fixed, SERS signals were collected from 4 different concentrations. The detection suggested clear correlation between the signal intensity with the molecular concentration of the target molecule. The enhancement factor of 4.14 x 10^3 has been calculated in comparison with using planar Si as the reference surface.

Measurement for fluorescence enhancement on the proposed LSPR metallic sample has been taken with the Olympus BX51 Upright Fluorescence Microscope. For this demonstration, the device has been patterned by photolithography to integrate the nanoscrews with plain Si. Ag deposition of 90 nm has been used. The fluorophore of interest is Rhodamine 6G, of 1 μM concentration. Solution has been dropped on the borderline of Ag coated nanoscrews and planer Si substrate as in Fig. 4.3 for clear comparison. TRITC mode has been utilized for filtering out the excitation light. It has been examined that fluorescence enhancement is only seen in the nanoscrew region. Outside of that, only coffee ring stain induced local droplet concen-

tration spots on the Ag coat planer Si exhibit strong enough fluorescence to be detected. With background subtraction, metal enhanced fluorescence (MEF) factor of approximately 20 has been achieved.

4.1.3 Rotational deposition of metal on nanostructures

While top down e-beam deposition has been used thus far, additional schemes would be beneficial to tune the metal nanoparticle morphology in favor of excitation light. The current configuration causes the bottom nanoparticles to be partially blocked by nanoparticles formed at the tip of the device. This caused reduction in both the excitation light and back-scattered optical signals. Another challenge is the unfavorable vertical alignment of the metal nanoparticle gaps. The gap in the vertical direction is too sparse as show in Fig. 4.4 (a). Deposition thickness in the range of 200 nm is required to reduce such gaps. This thick deposition will lead to increase in size of individual nanoparticles, causing the LSPR condition to shift away from the excitation laser of interest. The vertical direction is also limiting the coupling between nanoparticles. The electric field polarization needs to be in alignment with the physical arrangement the nanoparticles are in, as explained in Chapter 1. Hence the current metal nanoparticle arrangement limits efficient coupling.

To overcome such challenges, a two-step solution is proposed. Slanted metal nanoparticles, as seen in Fig. 4.5, are prepared on the nanoscrew Si substrate. The substrate is then characterized by a laser setup that may provide tilted angle illumination. This enables such 3D metal nanoparticles to have increased exposed areas to excitation laser and for scattered optical signal extraction. It would also provide increased matching between excitation light polarization and nanoparticle arrangement.

The slanted metal nanoparticles may be prepared by rotational metal evaporation. The rotational metal deposition has been done with the Temescal E-Beam Evaporation Systems in the Micro/Nanofabrication Facility of the Frederick Seitz Materials Research Laboratory, University of Illinois at Urbana-Champaign. It has been experimentally shown that due to the angled groove along the sidewall, the nanoscrew substrate would result in a localized glancing angle deposition (GLAD) [70] with simply rotating the substrate during deposition. The SEM images in Fig. 4.4 compare the resulting 3D metal

nanoparticles with and without substrate rotation. It is seen that rotational metal evaporation causes the deposited metal nanoparticles to form different configuration in comparison to top-down evaporation.

The mechanism behind slanted metal nanoparticle formation is shown in Fig. 4.5. The rotational deposition causes the effective deposition surface area to widen. While this would enable the top of the nanoscrew feature to form metal nanoparticle shaped as a quarter sphere, the side lobes will have limited effective area due to blocking from the Si nanoscrew itself. Hence the metal deposited on the side lobes would result in fan-shaped nanoparticles, decreasing the minimum gap between each nanoparticle.

The rotational metal deposition is not limited to Ag. The SEM images in Fig. 4.6 show similar results achieved for both Au and even TiO_2. As long as the system provides substrate rotation, such results have been obtained. The device results from TiO_2 on Si nanoscrew will be utilized for photocatalytic experiments in Chapter 5.

The proposed device of slanted 3D metal nanoparticle will be characterized with tilted angle excitation laser setup in the future.

4.2 Extension towards silicon nitride substrate

Si nanostructures have been used for the substrate material for LSPR substrate due to the ease of fabrication. Structures relying on random metal deposition along sidewalls of nanostructures have been previously demonstrated [69, 71] for such Si substrate based devices. However, several characteristics of Si suggest that the use of an alternative material would be beneficial. Herein we demonstrate the need for and capabilities of silicon nitride substrate as a substitution material.

4.2.1 Motivations for silicon nitride nanostructure based LSPR substrate

The Si nanostructures shown throughout this paper have two potential hindrances as a substrate for LSPR devices. First, the sharp tip Si nanostructure is a semiconductor with thinned Schottky barrier as in Fig. 4.7. Plasmon resonance is based on the oscillation of electrons, which would indicate the

strong boundary condition dependence. With Fermi level pinning between the metal and semiconductor, such thinning of electric barrier would increase the possibility of change in plasmon resonance conditions. Such interaction may cause increased damping of the electron cloud oscillation.

The second difficulty with Si nanostructure is the strong absorption capability. It has been experimentally determined that Si nanostructures proposed in this paper have less than 2% diffuse reflection across the visible wavelengths [41]. This would cause incoming excitation light to be partially absorbed as well as the target optical signal itself. The substrate material may capture both the Raman scattered light and fluorescence emission, decreasing the optical output of the sensor. This reduced optical signal effect is illustrated in Fig. 4.8.

In comparison, SiN is a dielectric material, which would not have electrical interactions with the metal LSPR layer. It also does not show such high optical absorption as with the case of Si. Less of the output optical signals would be absorbed by the substrate, as shown in Fig. 4.8. Hence SiN nanostructure substrate would provide the platform for 3D metal nanoparticle device with reduced electron cloud damping and optical absorption that are present in Si.

Simulation results for normalized scattering electric field are shown in Fig. 4.9 for both Si nanostructure and SiN nanostructure substrate. Silver nanoparticles are placed on pillar structures with a main large sphere on the tip with ellipsoidal particles along the sidewall and bottom. It is shown that a stronger enhancement of electric field is present for the case of SiN based structures. This comes in alignment of the motivation for replacing Si with SiN as the substrate material.

4.2.2 Demonstration of SERS on silicon nitride nanostructure based LSPR substrate

Comparison of Si and SiN nanostructure based 3D LSPR device has been experimentally demonstrated. The SiN nanostructure has been fabricated by SiN deposition on Si wafer followed by using Ag thermal dewetting approach as an etching mask against inductively coupled plasma reactive ion etching (ICP-RIE). Si wafer has been cleaned with a two trial repeated sequence of

5:1 H_2SO_4/H_2O_2 piranha etch followed by 10:1 hydrofluoric (HF) to remove possible residues on the substrate. The STS plasma enhanced chemical vapor deposition (PECVD) system has been used to deposited 300 nm of silicon nitride. Mixed frequency has been utilized to eliminate any possible effect from surface tension from the silicon nitride layer. The CHA electron beam metal evaporation system has been utilized to deposit 10 nm of Ag on the SiN deposited substrate. The silver deposited substrate is then loaded into the Jipelec Rapid Thermal Processer. With rapid thermal annealing, the deposited Ag thin film form isolated random metal nanoparticles of 10 to 100 nm length scale. This process of thermal dewetting [24] condition depends on the surface tension between the two materials. Further experimentation comparing different surface tensions of silicon nitride as the thermal dewetting substrate material will follow in the future. Additional alternation of the Ag metal mask may be done by using O_2 plasma etch [72]. The SiN based nanostructures are then made by deep reactive ion etching (DRIE) in STS Advanced Silicon Etcher by the Bosch process, similar to the process of fabrication for nanoscrew Si [41]. Due to the difference in etch rates between SiN and Si, the etching conditions have been changed. The resulting nanostructure does not have as distinctive alternating grooves as the case for nanoscrew Si. Rather, the SiN nanostructure resembles a conical pillar.

The Si based nanostructure has been obtained from previously reported work [71] due to the similar conical shape of the SiN nanostructure. The SEM images in Fig. 4.10 show both devices of interest. The same 80 nm Ag deposition thickness have been used. Despite material difference, the two random nanostructured LSPR devices show similar metal nanoparticle morphology. Specular reflectance data from both surfaces have been taken with the Woollam Variable Angle Spectroscopic Ellipsometer in the Laser and Spectroscopy Facility within the Frederick Seitz Materials Research Laboratory, University of Illinois at Urbana-Champaign. Incident angle of 15 degrees has been tested, with the visible spectrum as the wavelength range of interest. The reflectance data from Fig. 4.11 shows that at 633 nm, the Ag coated Si nanostructure shows 7.4% specular reflectance whereas the Ag coated SiN nanostructure has 17.1%. The enhanced specular reflectance indicates the relative increase in optical signal output of SiN over Si device.

The SERS signals between the two different devices are shown in Fig. 4.12. The SERS data have been acquired by the Horiba Confocal Raman Imag-

ing Microscope in the Microscopy Suite of the Imaging Technology Group, Beckman Institute, University of Illinois at Urbana-Champaign. Excitation laser of 633 nm has been used, with proper attenuation of laser input power to avoid saturation of the Raman signal. Integration time of 10 seconds has been used. As for the sensing target, 10 μM of R6G has been used. The resulting signals indicate a significant enhancement of SERS signal of the SiN nanostructure LSPR device in comparison to that of the Si based system.

Further experimentation for thickness optimization has been conducted as seen in Fig. 4.13. Silver deposition of 60, 70, 80, and 100 nm thickness by top-down metal evaporation has been conducted. It is shown that deposition up to 80 nm remains particle-like, whereas 100 nm deposition results in rather a continuous film of Ag on the SiN nanostructure. SERS signal shown in Fig. 4.14 has been demonstrated with the identical setting as mentioned above except for laser attenuation for better comparison. It is shown that the case of 80 nm Ag deposition, which results in enlarged metal nanoparticle prior to forming a continuous film, would be preferred.

4.3 Conclusion

The concept of 3D packed metal nanoparticle LSRP device with utilization of alternating grooved nanostructure backbone substrate has been demonstrated. While this concept itself provides the platform for enhanced optical sensing, we have shown the capability of rotational metal evaporation for the formation of slanted metal nanoparticle in efforts to enhance the coupling of incident excitation light with the plasmonic modes of the device. As another possible direction for enhanced excitation and extraction of optical signals, we have shown SiN as the substation material for Si nanostructures due to enhanced boundary condition and higher optical reflection. Future schemes utilizing a back reflection such as Al metal film between the SiN nanostructure layer and the Si wafer would be experimented for further light extraction. Transfer of SiN based LSPR device to transparent substrate such as quartz may benefit fields such as cell imaging due to the enablement of transmission microscopy.

4.4 Figures

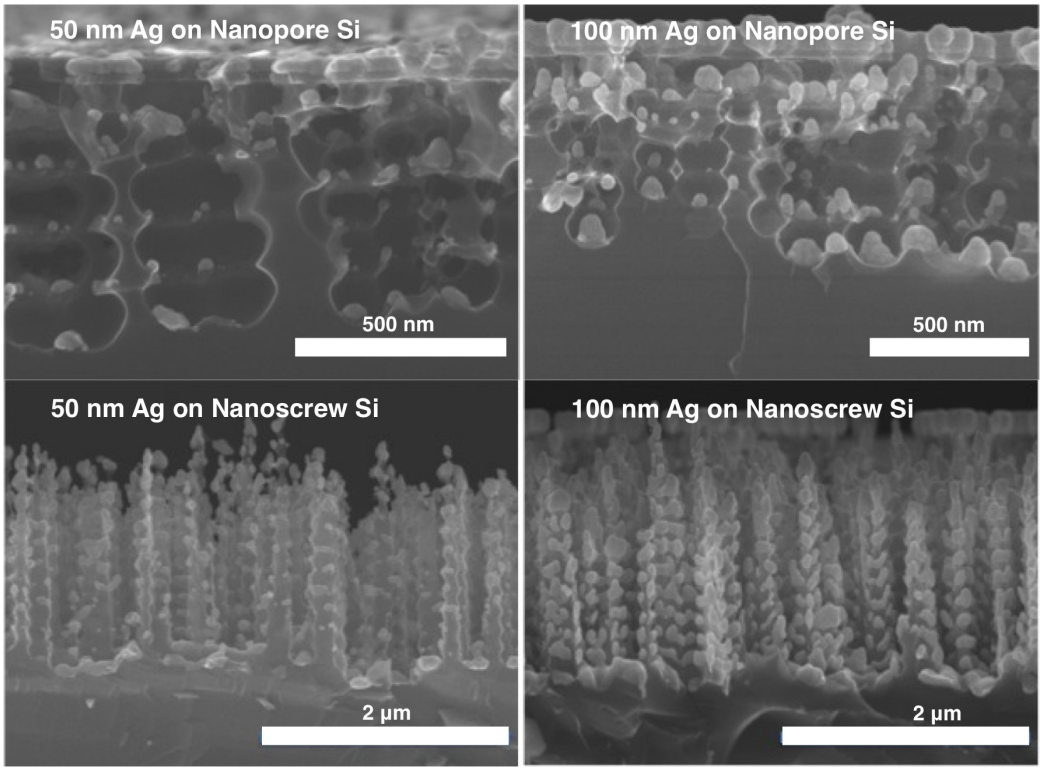

Figure 4.1: Metal deposition on nanopore and nanoscrew Si surface with cross sectional SEM images shown. The comparison between equal amounts of metal deposition thickness reveals that the nanoscrew case is preferred over nanopore for metal nanoparticle formation on the side lobe of the Si nanostructure.

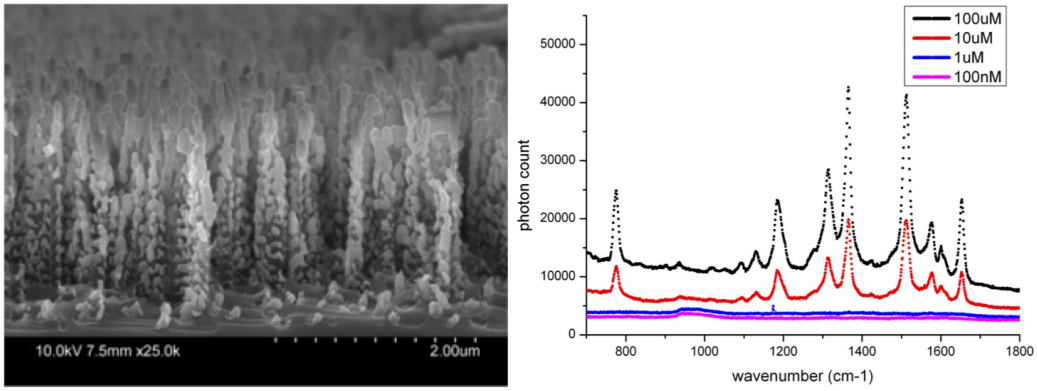

Figure 4.2: Nanoscrew with Ag 200 nm deposition tested for SERS. SEM images show the cross sectional view (left) with the Raman spectrum (right). Rhodamine 6G has been used as the sensing target. The excitation condition is 633 nm laser with 2.5 mW power setting, 20 seconds of exposure. In comparison to data obtained from planar Si, the enhancement factor is 4.14 X 10^3

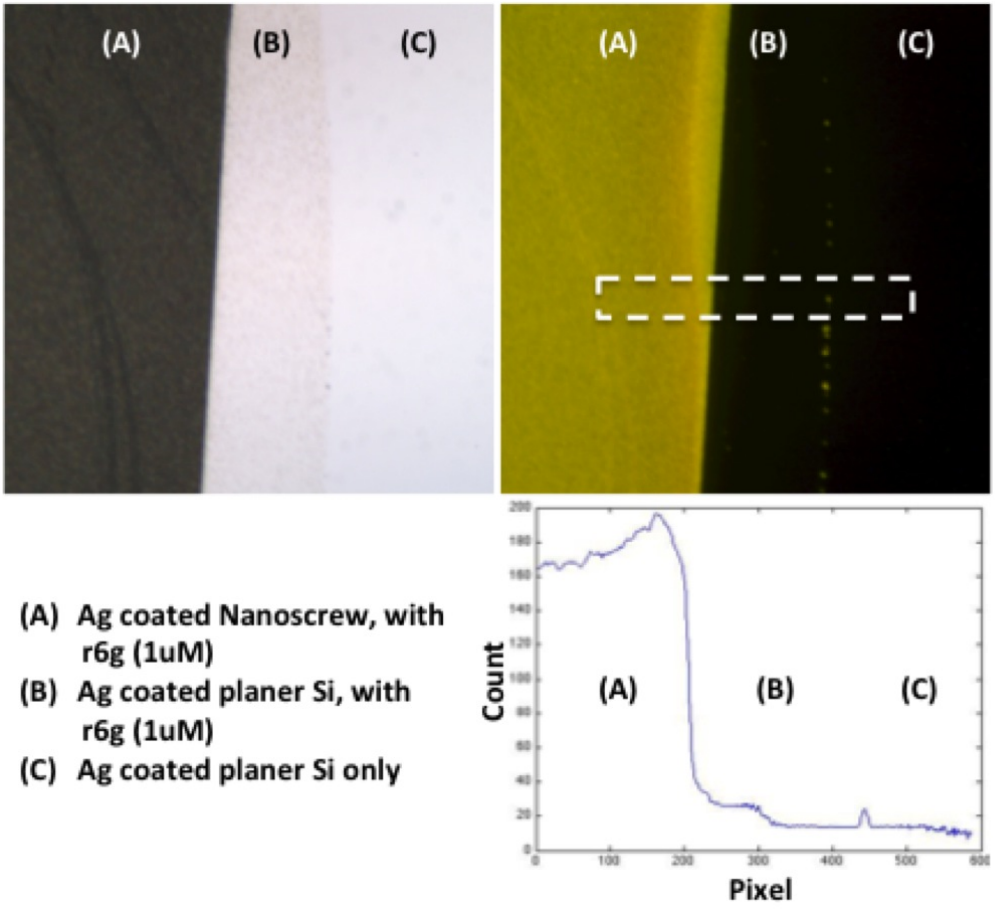

Figure 4.3: Bright field image of Ag deposited nanoscrew integrated with planer Si after 1 μM Rhodamine 6G dispersed at borderline (left) with corresponding TRITC image (top right). Pixel count of fluorescence image within the dotted line confirms the higher enhancement within the nanoscrew region (bottom right).

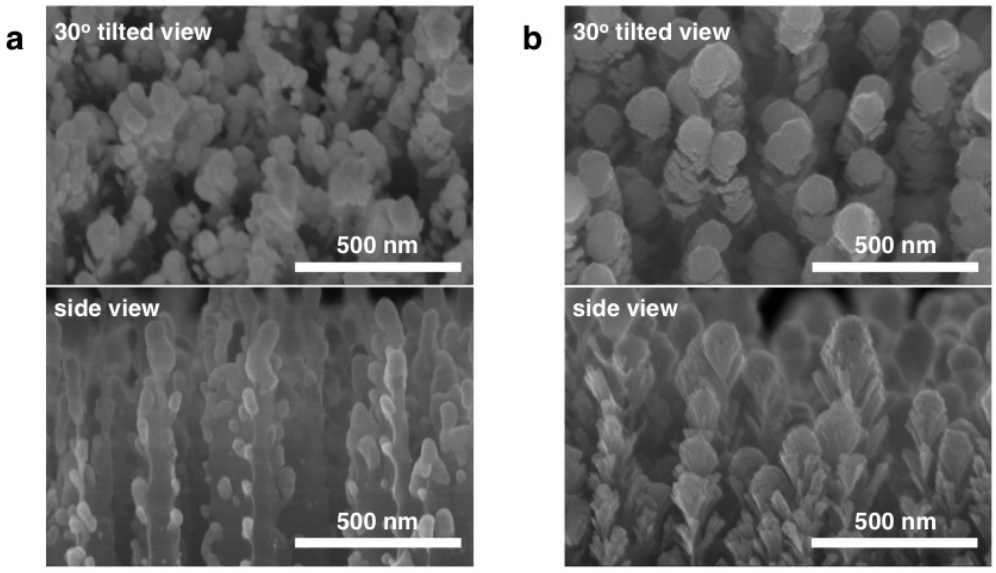

Figure 4.4: (a) SEM images of 120 nm Ag deposited on nanoscrew Si by top down approach. The ebeam system did not supply substrate rotation during the evaporation process. (b) SEM images of 120 nm Ag deposited on nanoscrew Si by rotational approach. The substrate is rotated in the process of metal evaporation.

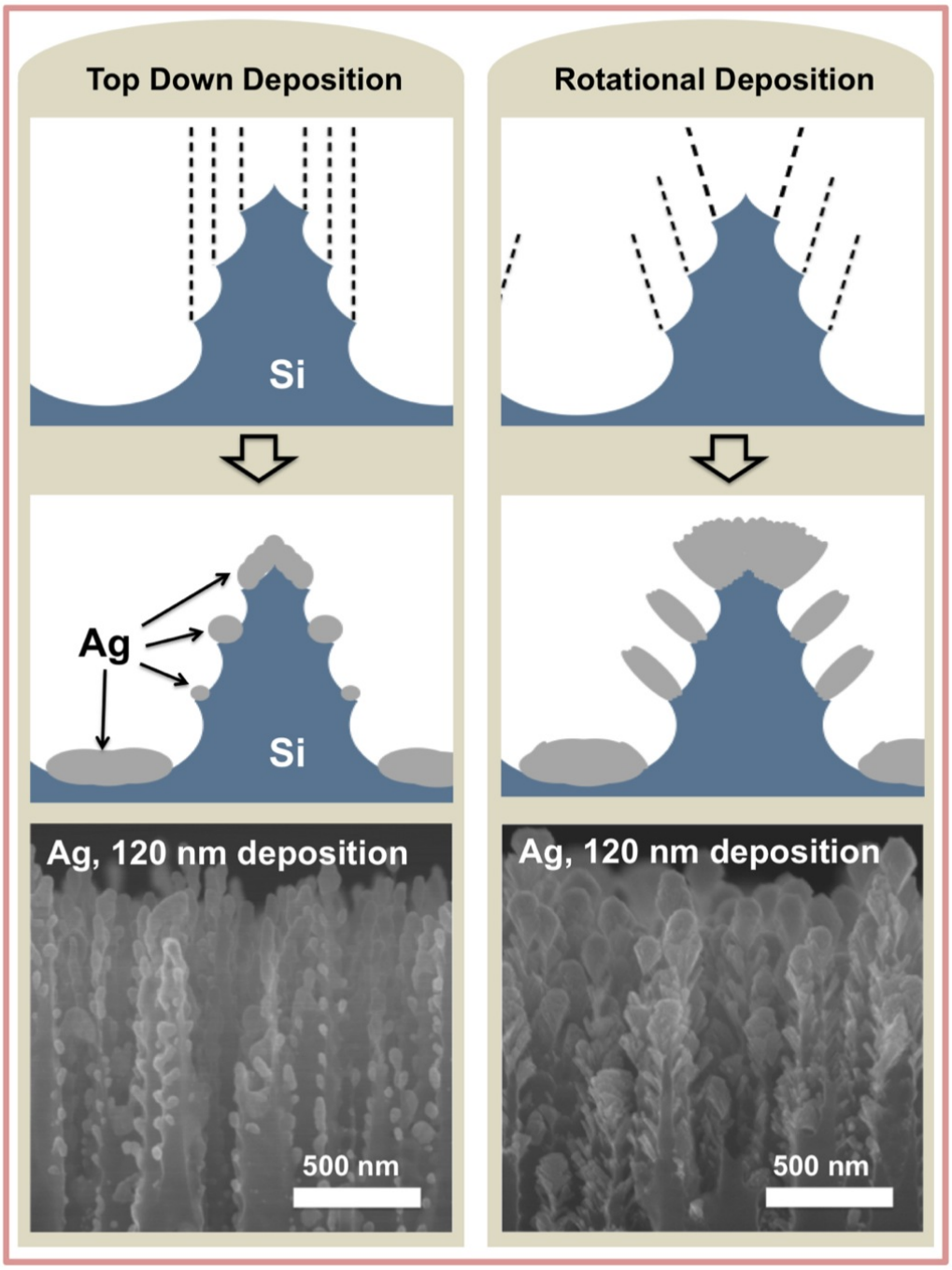

Figure 4.5: Schematic with corresponding cross sectional SEM images showing the difference between non-rotational and rotational ebeam deposition in nanoscale sidewall deposition. The slanted nature of the proposed nanoscrew surface causes localized glancing angle deposition [70], leading to slanted effective deposition surface. This causes the rotational deposition to force fan-like metal nanostructures to form on the sidewalls of the nanoscrew Si.

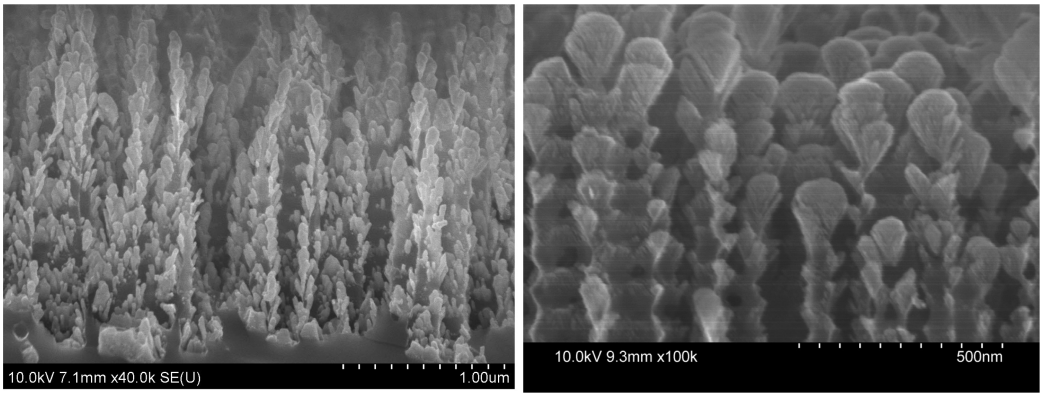

Figure 4.6: Cross sectional SEM images showing the rotational metal deposition with Au and TiO_2. The target planar thickness of each material were 200 nm for Au and 100 nm for TiO_2.

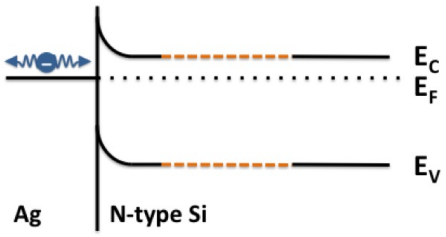

Figure 4.7: Energy band diagram for SERS of Ag on Si case. Having a doped Si surface as the substrate material for SERS is not favorable due to possible interaction between the electrons in the metal nanoparticle with that in the Si. This would only be of interest with nanoscale Si tips due to the thinning of the Schottky barrier in such condition.

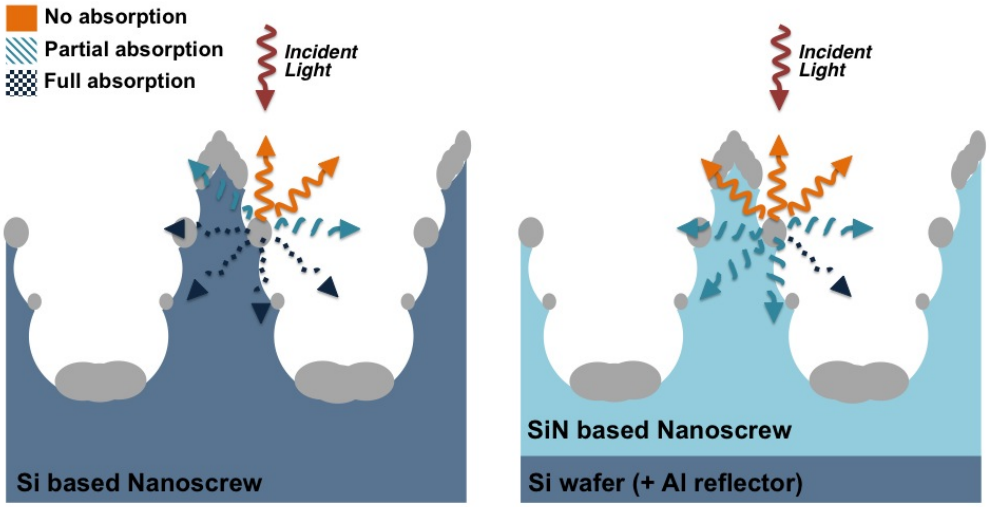

Figure 4.8: Schematic displaying the light absorption disadvantage of nanostructured Si as SERS substrate material. Due to the low reflectance of such Si based nanostructure surface [41], a significant amount of signal is trapped within the structure. This causes the overall extracted scattering signal to decrease. The SiN based system does not exhibit such high optical absorption, hence would be able to enhance the Raman signal. This analogy would be applicable toward fluorescence signals as well.

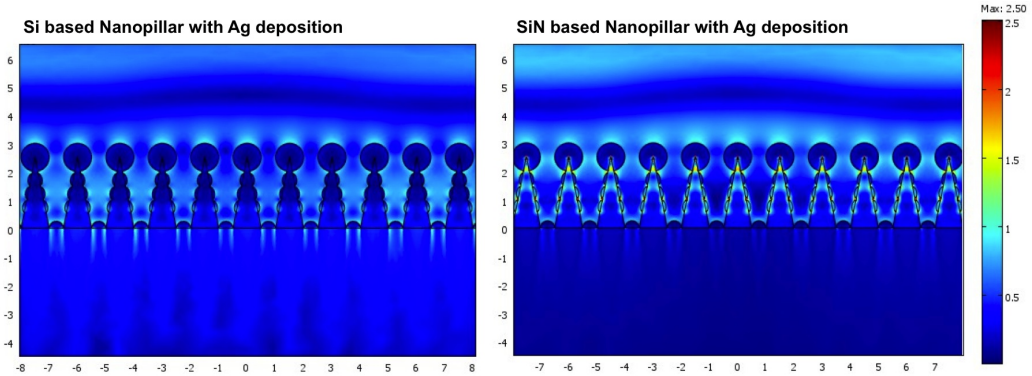

Figure 4.9: Simulation result of normalized scattering electric field enhancement. The physical dimension scales on the x and y axis are in units of 100 nm. The simulated surface are constructed with a main backbone pillar made of either Si or SiN that is covered by spherical and ellipsoidal Ag nanostructures. The results indicate higher electric field enhancement for the case of SiN based nanostructure.

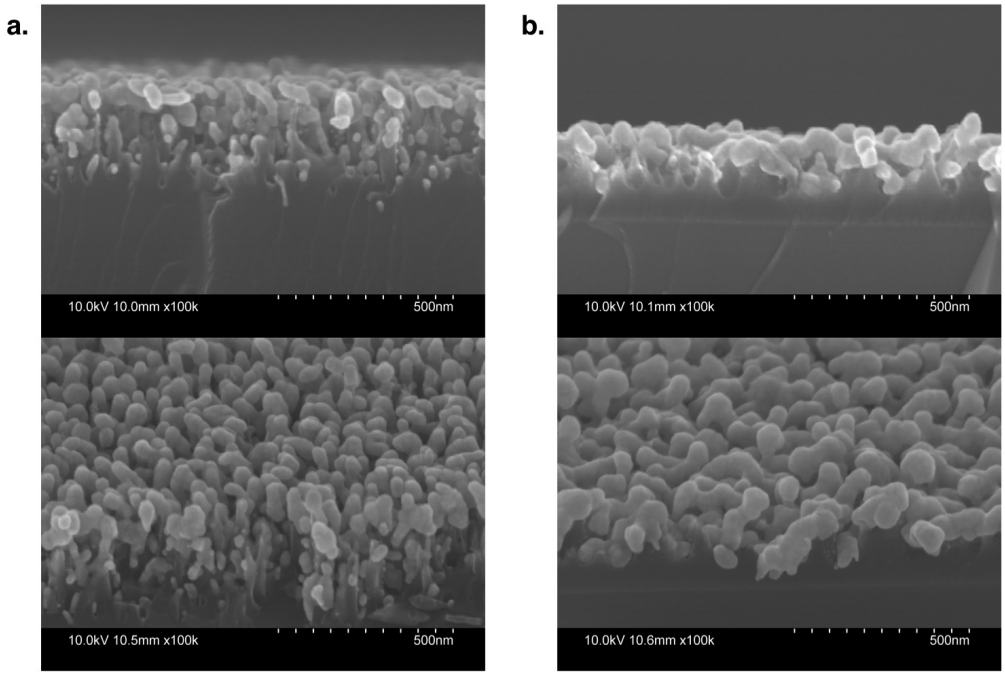

Figure 4.10: SEM images showing cross sectional and 60 degree tilted views of Si and SiN based LSPR substrates. Both samples are deposited by 80 nm of Ag.

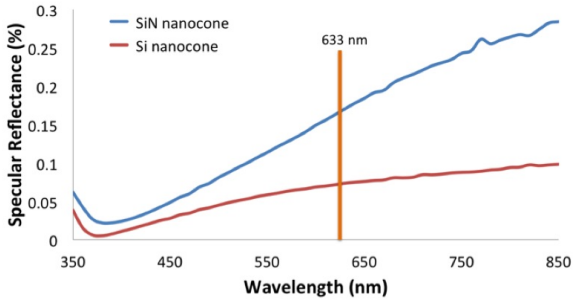

Figure 4.11: Specular reflectance data for 15 degree incident angle of both Si and SiN nanocone structures with 80 nm of Ag deposition. The term nanocone describes the smooth sidewall shape the SiN based surface has formed. The Si based devices used are identical to those reported in [71]. The results indicate that at 633 nm, SiN based nanocone shows 17.1% whereas Si based nanocone has 7.4% reflectance. The increased reflection suggests ease of extracting scattered signals from the substrate.

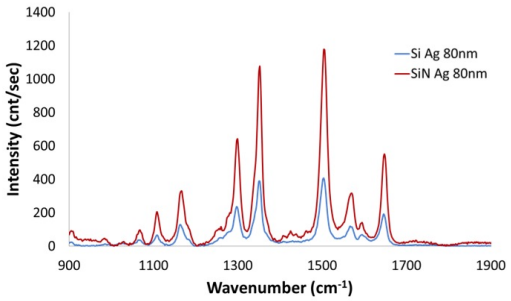

Figure 4.12: SERS signal comparison between Si and SiN based LSPR substrate. Total of 80 nm Ag has been deposited on both surface. For SERS comparison, 10 μM of R6G has been used with 633 nm as the excitation laser, 10 seconds of integration time.

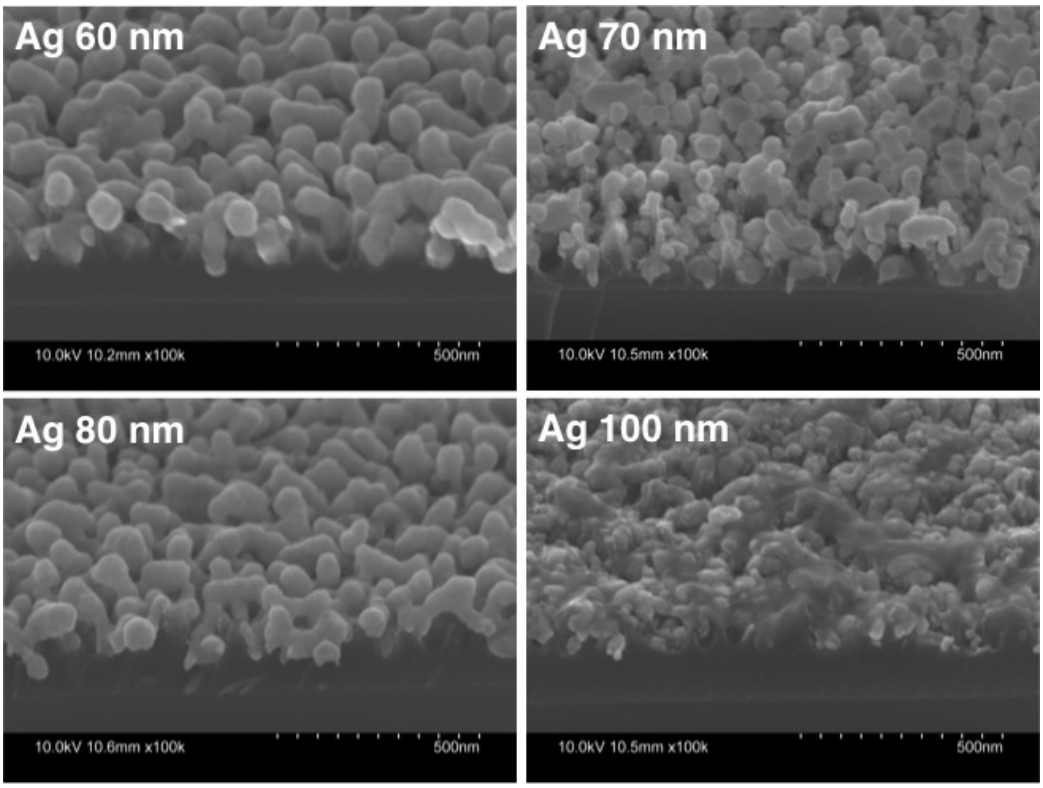

Figure 4.13: SEM images showing 60 degree tilted views of SiN based LSPR substrates with varied Ag deposition thickness. For thickness approaching 100 nm, the deposited Ag layer tend to form a continuous film rather than discrete particles.

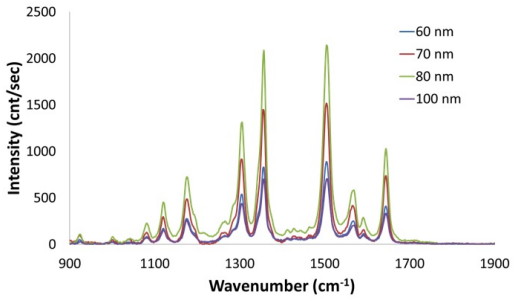

Figure 4.14: SERS signal comparison of different metal thickness deposited on SiN based LSPR substrate. For SERS comparison, 10 μM of R6G has been used with 633 nm as the excitation laser, 10 seconds of integration time.

CHAPTER 5

FUTURE DIRECTIONS TOWARD WATER DISINFECTION AND WATER SPLITTING APPLICATIONS

The similarity between the concepts of photochemical based water disinfection and photocatalytic water splitting has led to the investigation of utilizing the proposed nanoscrew Si as the platform for such chemical reactions. The high optical absorbing nature of the nanoscrew surface described in Chapter 2 with the demonstration of photochemical metallic nanoparticle transformation in Chapter 3 have shown such possibilities.

This chapter will cover the basis of water disinfection and water splitting, with demonstrations by the proposed nanoscrew Si device. Section 5.1 will discuss the mechanism behind semiconductor photocatalytic reaction for water disinfection with Section 5.2 dedicated to that of water splitting. Section 5.3 will demonstrate the water disinfection capability by the proposed nanoscrew Si based 3D photocatalytic substrate. Future directions with the proposed nanostructured Si will be discussed in Section 5.4.

5.1 Semiconductor photocatalytic water disinfection

The lack of clean water is becoming a common problem for all countries around the world. We are facing rising challenges to meet the demands of clean drinking water in regions ranging from the Middle East, to South Asia, Northern Africa, and parts of Brazil [73]. Even China, despite efforts at constructing reservoirs of water sources, has recently faced a series of water shortages [74].

As of 2011, an estimated 884 million people rely on biologically unsafe water sources, resulting in increased risk of infection [75]. It has been mandated by the UN Millennium Project to halve the population of the globe that are without access to a clean source of drinking water [76]. While chemical treatment based on chlorine or hydrogen peroxide provides efficient purifi-

cation, the operational expertise required to avoid side effects hinders its adaptation in developing countries [75]. This has led to the development of a simple disinfection scheme solely based on solar energy. The solar disinfection (SODIS) concept has become an alternative to chemical based removal of organic pollutants in water sources for its simple and economical nature. However, SODIS has various constraints limiting the efficiency such as the long treatment time of more than 6 hours, requirement of steady sunlight, and the uncertainty of disinfection [75].

To address these challenges, a promising approach is the utilization of semiconductor photochemical reactions. Semiconductors produce electron-hole pairs when illuminated with light that has energy above the semiconductor bandgap. These charge carriers may recombine or may migrate to participate in redox reactions at the semiconductor-water interface. The reactive oxygen species produced, such as hydroxyl radical, are indiscriminate oxidants [77, 78]. This leads to destroying contaminants and microorganisms in the water. Companies such as Purifics Environmental Tech Inc. (Canada), Hyosung Ebara (Korea), and Ishihara Sangyo Kaisha (Japan) have developed commercial products for photochemical water disinfection [79].

The basis of SODIS is the damage of cell membrane by oxidation. In conventional SODIS that uses as much as 8 hours of daylight exposure, the biocidal mechanisms are due to UVA radiation (315 nm to 400 nm) and thermal inactivation [75]. The direct UVA radiation in sunlight leads to cell membrane damage and blocks the growth of pathogens [80]. In addition to direct effects, UVA radiation produces reactive oxygen species by dissolving oxygen in water [81] which would also lead to biocidal activities. Thermal biocidal activities, typically induced by water absorbing the visible red and IR portion of light, have been observed to become comparable to the contribution from that of by UVA above 45 ^{o}C [75].

While conventional SODIS utilizes UVA and thermal based disinfection, semiconductor photocatalytic approaches follow two distinct paths of cell membrane disintegration as shown in Fig. 5.1. Pathogens may come in direct contact with the semiconductor surface. This will cause oxidization of the cell membrane possibly by charged carrier injection across the semiconductor-cell interface, but more likely by hydroxyl radicals formed on the semiconductor. For the case not in direct contact but rather in proximity of the photocatalytic substrate, hydroxyl radicals generated from water by the semiconductor will

diffuse towards the pathogens. This will also lead to the disintegration of the cell membrane [77]. The specific illustration for titanium oxide based water disinfection is shown in Fig. 5.2.

The biocidal process of a cell is shown in Fig. 5.3. The direct contact between the semiconductor surface and the cell membrane leads to increased permeability. This degree of damage is to a recoverable degree. It is the reactions with hydroxyl radicals which leads to additional permanent damage to the cell wall, resulting in leakage of ions and small molecules from the pathogen. Continued damage results in loss of larger compounds, leading to the degrading of major cell components. The cell disinfection is completed by the complete mineralization of the remaining materials [77]. The mechanism of cell membrane damage is initiated by the attack on fatty acids, which may react with hydroxyl radicals [78]. The oxidation of fatty acids by the photocatalytically generated hydroxyl radical causes the cell membrane to become porous, leading to the leaking of internal materials mentioned above. In the outer membrane, lipopolysaccharide (LPS) and phospholipid are made from fatty acids, and hence would be of particular interest in water disinfection [78].

5.2 Mechanism of semiconductor photocatalytic water splitting

Sustainable development is not limited to gaining clean sources of water. The energy sector would contribute substantially by reducing carbon emission through utilization of sunlight. Concepts such as solar powered cars [82], zero energy buildings [83], and solar power plants have been consistently researched. However, the variations in the sunlight available on a daily basis as well as regional discrepancies requires the efficient storing of solar energy for practical applications [2]. It has been considered that the Holy Grail of utilizing solar power is the conversion and storing of energy by means of water splitting and hydrogen storage. This approach, based solely on water, will eliminate the requirement of complex chemical based battery systems for storage.

The mechanism behind water splitting is based on the chemical variation water molecules go through in strong oxidation/reduction chemistry. When

proper energy conditions are met, water molecules are split into different chemical states. The chemical balance for oxygen evolution reactions (OER) is shown in Eq. 5.1. Hydrogen evolution reactions (HER) are in Eq. 5.2 and Eq. 5.3 [2].

$$Injection\ of\ holes\ into\ electrolyte:$$
$$2H_2O + 4h^+ \rightarrow O_2 + 4H^+ \tag{5.1}$$

$$Injection\ of\ electrons\ into\ electrolyte:$$
$$2H^+ + 2e^- \rightarrow H_2\text{: } for\ low\ pH \tag{5.2}$$
$$2H_2O + 2e^- \rightarrow H_2 + 2OH^-\text{: } for\ high\ pH \tag{5.3}$$

$$Overall:$$
$$2H_2O \rightarrow O_2 + 2H_2\ , \delta G = 237.2 \frac{\text{kJ}}{\text{mole}} \tag{5.4}$$

Note that reactions for the HER are dependent on the pH value of the solution of interest. The reaction in Eq. 5.2 is for low pH values in which there are plenty of H^+ ions. For neutral or base pH, the reaction in Eq. 5.3 is dominant.

The energy requirements of semiconductor based photochemical water splitting are shown in 5.4. This corresponds to 1.23 eV of energy per electron that is supplied. Hence, the ideal material for solar water splitting would have a band gap higher than that of the required splitting energy but at the same time a low enough band gap to be able to convert incoming photons into excited electron-hole pairs. An additional requirement is to have proper energy band alignment with that of the HER/OER. As shown in Fig. 5.4, the HER and OER each have preferred energy band. However, the energy value specified above does not account for overpotentials that are required to drive the HER/OER at the semiconductor surfaces. This means additional energy potential is essential to induce efficient water splitting. The conduction band of the semiconductor needs to be placed higher than the energy band

of HER while the valence band of the semiconductor should be sufficiently lower than the energy band of OER. Common semiconductor materials such as Si only have proper band alignment with HER, whereas Fe_2O_3 is matched for OER. It is worth noting that TiO_2 has been the early material choice due to the overlapping with both HER and OER energy bands as well as ease of fabrication.

There are other considerations that must be met other than energy band conditions. The material to be used needs to have chemical stability during the oxidation and reduction reactions with the electrolyte of interest. The semiconductors reductive and oxidation potentials must be further away from the band gap edges than the energy levels of the respective chemical evolution reactions [2]. The quality and size of the semiconductor crystal also affects the overall efficiency of the system. As shown in Fig. 5.5, the excited charge carriers need to reach the semiconductor-electrolyte interface without recombination. This can be achieved by using higher quality of crystalline material for the semiconductor and also by using nanoparticle semiconductors. With decreased size, the photon induced electron hole pairs may transport easily to the surface with reduced loss.

The water splitting process is completed with surface chemical reactions. The two main factors affecting the surface chemistry efficiency are the density of active sites and the surface area [84]. The excited charge particles that are transported to the semiconductor-electrolyte interface may participate in the chemical reaction only when an active site is available. In absence of such active redox sites, the electron-hole pairs will recombine with each other. Catalysts such as Pt are introduced in forms of nanoparticles to increase the active sites. The high numbers of available energy states in a metal along with the Schottky barrier mean increase in the minority carrier transport from the semiconductor into the metal. Hence more excited carriers are used to participate in redox reaction. Another consequence of this is the decreased possibility of semiconductor corrosion, due to less minority carrier charge being stored at the semiconductor surface. The density of active sites is related to the overpotentional that has been mentioned above. With improved kinetics of the chemical reaction, the required overpotentional is decreased, allowing higher efficiency of photon energy induced water splitting. The use of the semiconductor itself as nanoparticles also benefits in this aspect due to the increased surface area. Larger exposed surface area of the

semiconductor enables the absolute number of active sites to increase [2].

While a single material may be used, it is also possible to utilize two different semiconductors for photocatalytic water splitting, each of which is matched for HER and OER, respectively. This type of system, named dual band gap configuration, enables the engineering of the anode and cathode of the water splitting system separately. This may significantly reduce the band gap of the semiconductors involved in the water splitting process, leading the system to utilize a wider range of light illumination.

Utilization of multiple semiconductors is not limited to separate HER/OER active surface engineering. More than one semiconductor may be used to fabricate a single water splitting electrode. While the outermost layer semiconductor would act as the active layer, the sublayer semiconductor facilitates the process by injecting the appropriate carrier (electrons for HER, holes for OER) or removing the opposite carrier from the active semiconductor [62]. This type of tandem cell uses a wider range of wavelength, increasing the overall efficiency of the system. An example utilizing Si/TiO_2 system is shown in Fig. 5.6, where it is shown that n-Si efficiently eliminates the electrons in TiO_2, allowing the holes in the TiO_2 system to avoid recombination. This allows increase in the hole injection into the electrolyte of interest.

5.3 3D stacked dual semiconductor photocatalytic substrate

In extension to the work on 3D stacked metal nanoparticles, we show here a 3D stacked dual semiconductor nanostructure for the use of water disinfection and potentially towards water splitting. The engineering innovation of this structure, shown in Fig. 5.7 and Fig. 5.8, is applicable for both water disinfection and water splitting applications. For water disinfection, the backbone n-Si layer will act to facilitate the extraction of electrons from the TiO_2 layer similarly to the work illustrated in Fig. 5.6. However, the increased surface area by the nanoparticle TiO_2 stacked in high planar density with the high optical absorption capability of the Si nanoscrew layer provides strong photochemical capability in comparison to previous reports. This will enable the substrate to produce hydroxyl radicals more efficiently. In applications for water splitting, this approach again benefits from the high

Table 5.1: Fluorescence Conditions for Promokine Live/Dead Cell Staining Kit

	Excitation	Emission
Live Cells	490 nm	520 nm
Dead Cells	490 nm to 545 nm	620 nm

surface area, as the active site will be increased. The difference from the water disinfection case is that the Si nanoscrew itself will have an active role in the photochemistry. The HER will be primarily conducted on the exposed Si region, whereas the OER reaction will occur on the TiO_2 nanoparticle.

The demonstration of water disinfection is shown with the disintegration of E. coli. We have used Promokine Live/Dead Cell Staining Kit to provide green stain to live cells and bright red stain for dead cells. The basis of staining is the attachment of the green stain on the cell membrane while red stain is applied on the DNA within the cell. It is only the case when the membrane is disintegrated and the cell is functionally dead that the red stain will be seen. The fluorescence conditions for the live cell stain are shown in Table 5.1.

To image the cells, Olympus BX51 Upright Fluorescence Microscope has been used. With the data from Table 5.1, FITC mode (excitation 490 nm, emission 525 nm) is used for live bacteria imaging with TRITC mode (excitation 557 nm, emission 576 nm) for dead bacteria imaging. Even though the dead cell mode is not in accord with the specifications from the vendor, the results have shown successful imaging of dead cells.

The disinfection capability of the TiO_2 deposited Si nanoscrew surface is compared with that of TiO_2 on planar Si. The substrate has been integrated on a single device using photolithography. With the process described in Chapter 2 for integration of nanoscrew Si with planar Si, followed by a top down TiO_2 ebeam evaporation via a Denton Electron Beam Evaporator system, the sample is prepared for comparison testing of water disinfection.

The E. coli bacteria has been prepared in broth with 8 hour incubation in 36 ^oC to insure high density within the solution. Promokine stain solution that contains both live and dead cell stains has been prepared accordingly to the procedures provided. The bacteria disinfection has been tested by applying a droplet of E. coli containing broth on the surface of interest, followed by dropping an equivalent volume of the stain solution on top. Cover

glass has been applied to delay death of bacteria due to drying of solution during experimentation as well as ease of experimentation.

As control experiments to test for background fluorescence, the staining dyes have been applied to the surfaces of interest as in Fig. 5.9. It is worth noting that the live cell stains have slight background fluorescence on top of the nanoscrew Si surface. In the case of dead cell stain, no such background has been observed. Hence the effect the substrate itself would have on the fluorescence has been accounted for.

We have intentionally provided dead bacteria on top of the two surfaces of interest to test any substrate dependent differences that may arise from the dead cell stain fluorescence. After dropping the bacteria solution and the staining kit, we intentionally let the surface dry out. This would cause all bacteria to be killed regardless of the surface the bacteria are attached to. The results seen in Fig. 5.10 illustrate how there is no apparent difference between the two surfaces of interest if all cells are dead. As expected, we are able to see abundant E. coli that have been disinfected on both surfaces.

Prior to testing the TiO_2 on the nanoscrew Si system, the E. coli disinfection has been tested directly on ntype nanoscrew Si. The absence of TiO_2 would result in low efficiency of hydroxyl radical formation, hence weak disinfection capabilities. The images in Fig. 5.11 show that we may only see live bacteria (small rice pattern emitting relatively high emission of green), but no indications of dead bacteria.

The final experiment using the TiO_2 on nanoscrew Si substrate is shown in Fig. 5.12. We are able to see a significantly higher density of live cells in the planar Si region in comparison to nanoscrew Si. For dead cells, we are able to observe strong disinfection capabilities of the TiO_2-nanoscrew Si substrate. Multiple screen shots over time confirm that the majority of dead bacteria shown to be placed on top of the planar Si side have actually migrated from the nanoscrew Si region. Hence it is shown that the proposed TiO_2 on nanoscrew Si system would be applicable for water disinfection applications.

5.4 Conclusion and future directions

Further quantitative analysis of the water disinfection would be required for proper characterization of the device. Cell counting as well as the integra-

tion of the TiO_2 on nanoscrew Si surface with microfluidics would provide a quantitative analysis of this device for cost effective water disinfection. One key experiment is testing the wavelength dependence of the system. As in Fig. 5.13, the mixture solution of bacteria and staining kit is injected into the inlet of the microfluidic device. The photochemical active area is illuminated with the wavelength of interest. Cell imaging to confirm the disinfection capability is done on the final microfluidic channel chamber. This work will be continued and prepared for publication in the near future. For water splitting, a proper catalyst would be required to facilitate the HER reaction. An assembly such as nanoscrew Si - Pt TiO_2 would provide the proper system. Key considerations that would need to be addressed would be the enhanced photocurrent as well as the composition of the resulting gas from the chemical reaction. For proper water splitting, it would be expected that the H_2 to O_2 ratio would be two to one. The optical absorbing nanoscrew Si substrate has been tested for direct sunlight absorption, photocatalytic material synthesis, and preliminary water disinfection testing. We expect this system to expand towards hydrogen generation to address the sustainable growth of our society. The structure of the nanoscrew system has also been applied towards optical biosensing. The unique properties of this system provide means of increasing the efficiency of Raman scattering in comparison to using Si nanostructures as the backbone material for metal deposition. Future experiments with angled light sources as well as possible integration with photonic crystals to control the excitation light polarization are to be conducted.

5.5 Figures

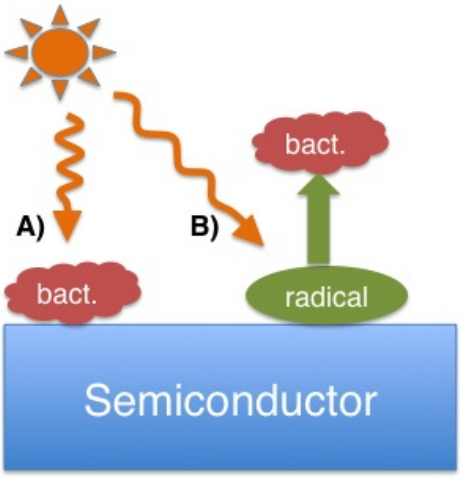

Figure 5.1: The two primary mechanisms of photocatalytic water disinfection by semiconductor. (a) Direct oxidation of pathogen (in this case bacteria) by the semiconductor surface. (b) Formation of reactive oxygen species which then disinfects pathogens not in direct contact with the surface. Image based on [77].

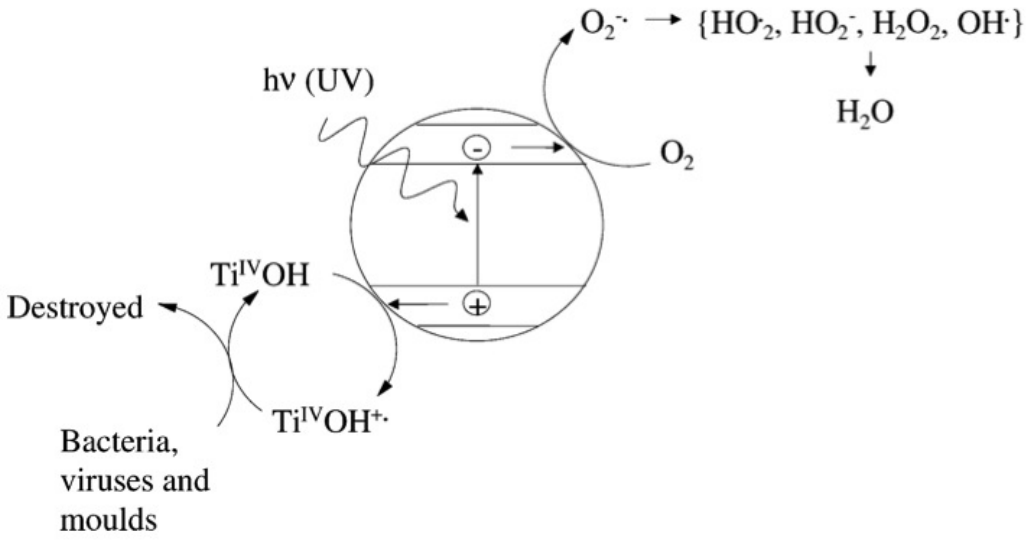

Figure 5.2: Schematic showing TiO_2 as the photocatalyst for water disinfection. The hydroxyl radical absorbed on the semiconductor surface will oxidize pathogens in direct contact. The excited electrons will react with oxygen, generating superoxide. This superoxide is then reduced to hydrogen peroxide, and eventually into water. Intermediate states will form additional sources for hydroxyl radicals that react with pathogens away from the surface [79].

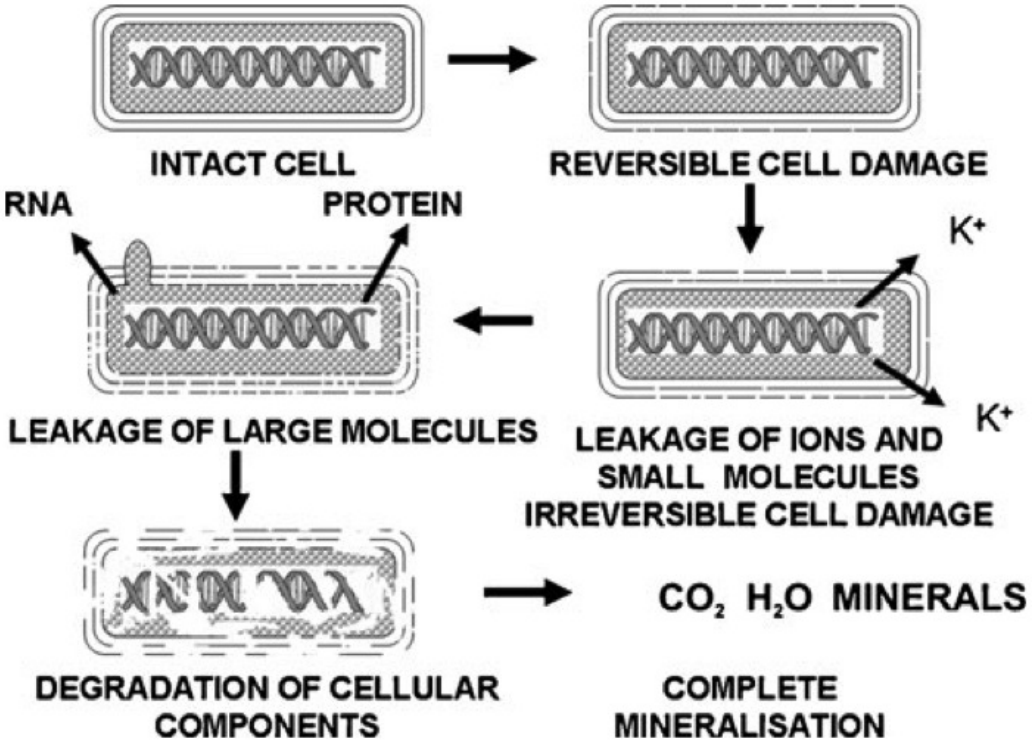

Figure 5.3: Schematic showing the process of cell disinfection. The hydroxyl radical damages the cell membrane which causes leakage of cellular material. Upon leaking of larger components within the cell such as RNA, the cell is fully discomposed [77].

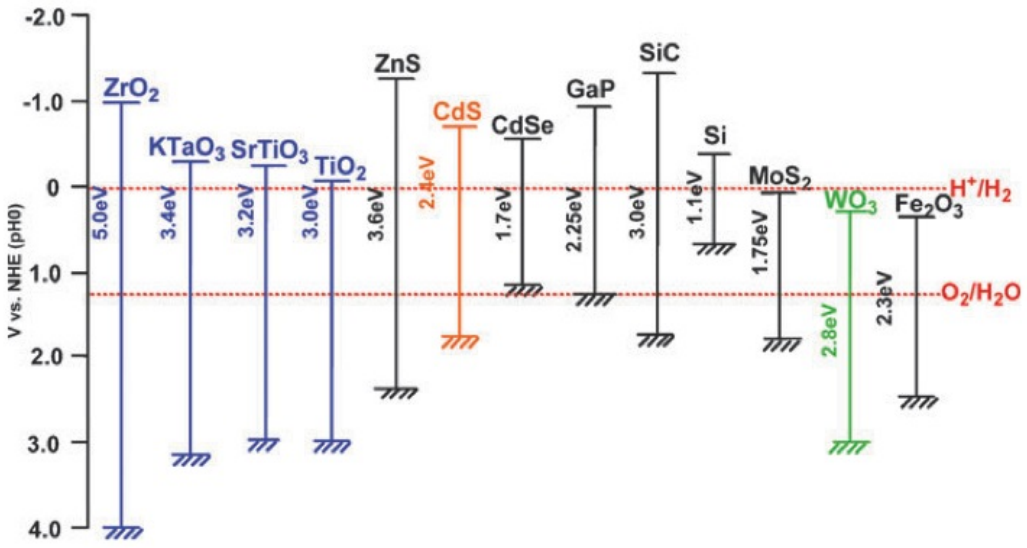

Figure 5.4: Different semiconductors showing energy band alignment with respect to that of the HER and OER reactions [84]. While CdS best fits for both reactions, environmental regulations have led to disregarding this material for study.

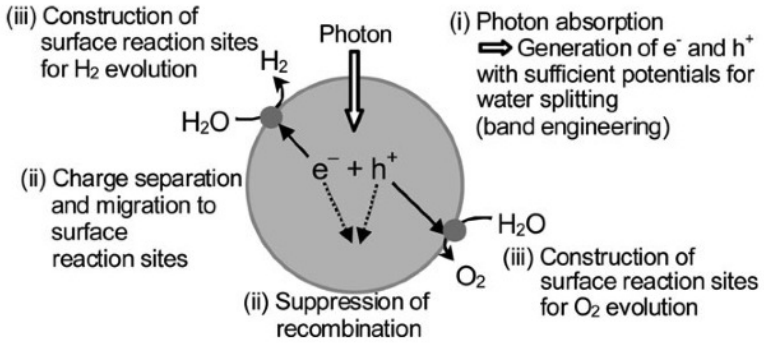

Figure 5.5: Schematic showing the overview of the photon induced water splitting process. The absorbed photon induces an electron-hole pair. The excited carriers may transport to the semiconductor-water interface. Upon migration to active sites, the carriers will participate in the respective reactions of water splitting [84].

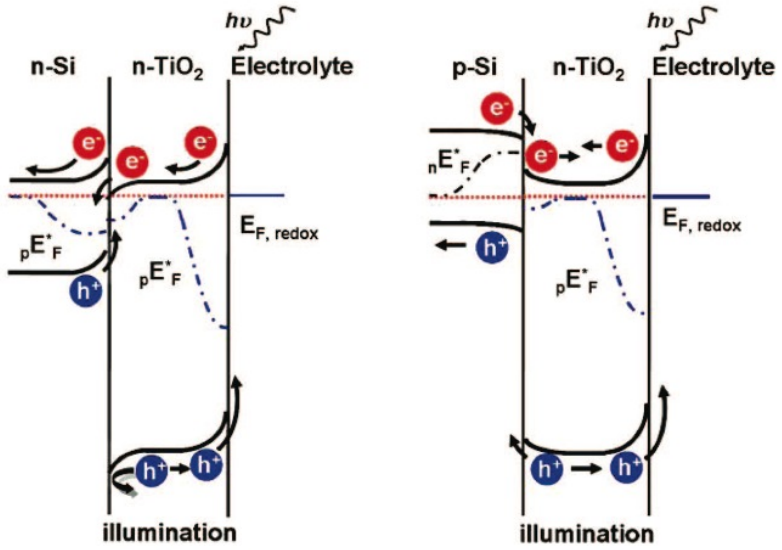

Figure 5.6: Energy band diagram showing a dual semiconductor system for photo-oxidation of water [62].

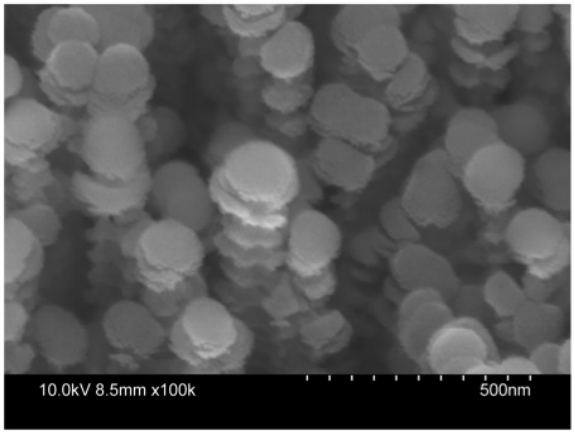

Figure 5.7: 30d tilted view of TiO_2 deposited on Si nanoscrew.

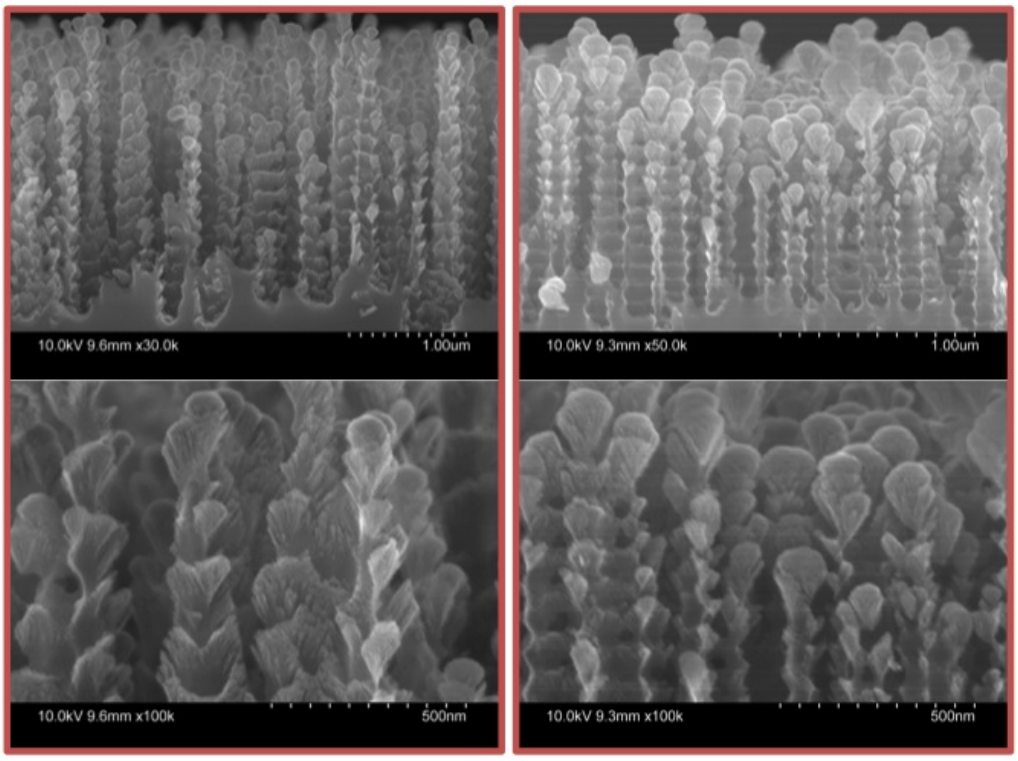

Figure 5.8: Cross-sectional view of 100 nm and 120 nm TiO_2 deposited on Si nanoscrew.

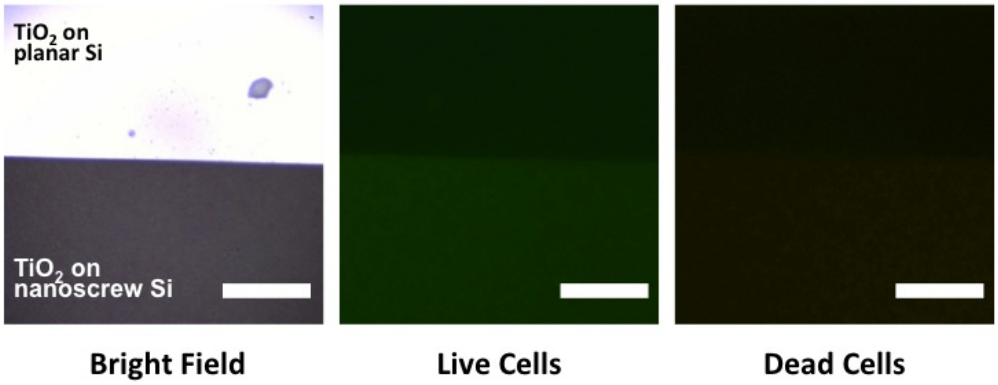

Figure 5.9: Control experiments of dropping only the fluorescence tags for live-dead cell staining assays on TiO_2 deposited nanoscrew Si and planar Si to test background fluorescence. Scale bar set at 0.1 mm.

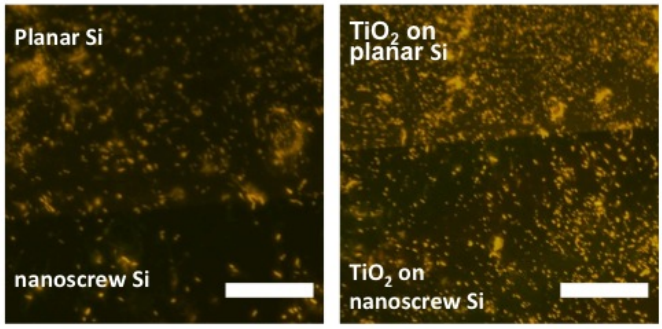

Figure 5.10: Control experiment showing stained dead cells on different types of substrate. The cells has been intentionally killed by drying the applied cell contained droplet.

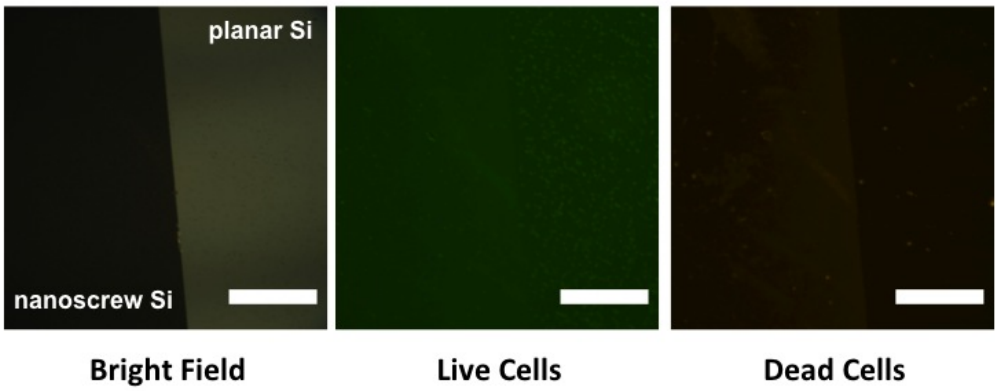

Figure 5.11: Experimentation of cell disinfection experiments with Si nanoscrew. Due to just Si being present, hydroxyl radicals are not being efficiently formed on the Si surface. Hence water disinfection is not achieved. Scale bar set at 0.1 mm.

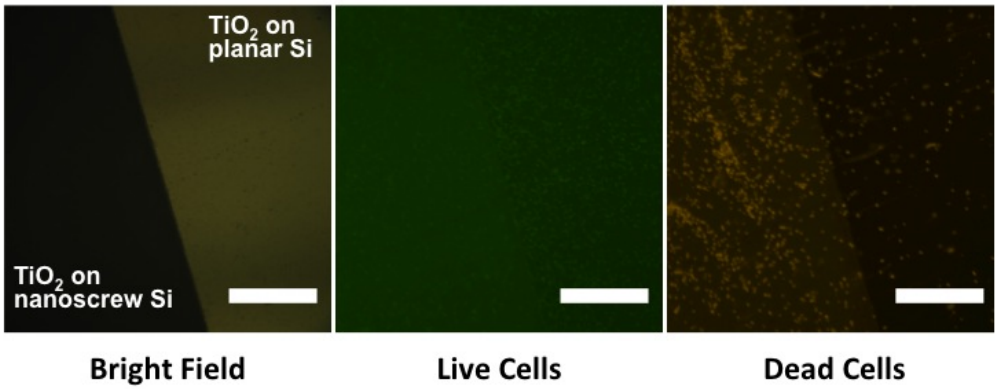

Figure 5.12: Experimentation of cell disinfection experiments with 3D stacked dual semiconductor substrate of TiO_2 deposited on Si nanoscrew. Disinfection of e coli cells are shown. The dead cells on the planar Si side have been confirmed from several screen shots over time to be from the migration of cells due to the flow of solution. Scale bar set at 0.1 mm.

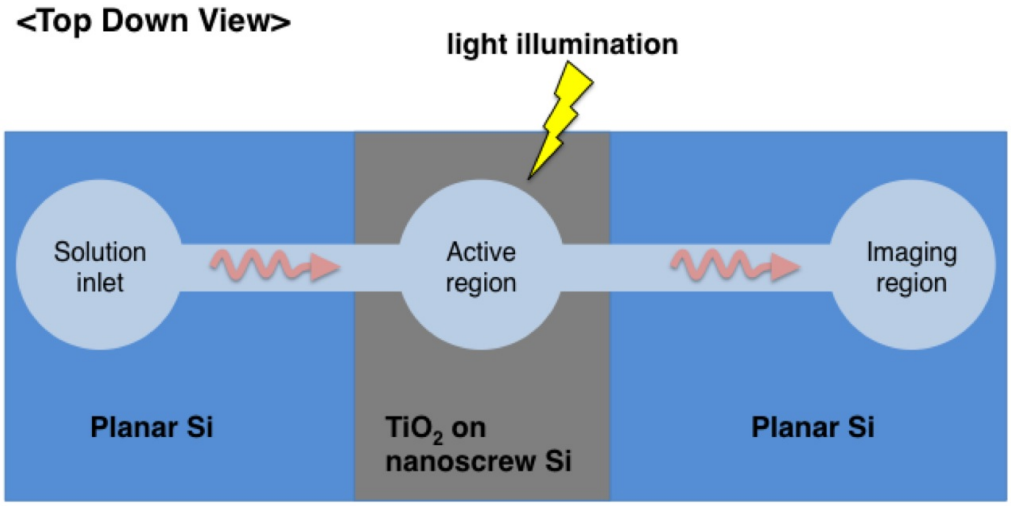

Figure 5.13: Experimental setup for testing wavelength dependence on water disinfection. The TiO_2 substrate is integrated with a microfluidic channel. Solution mixture of bacteria with the staining kit is inserted into the device, where a select wavelength is illuminating the active nanoscrew area. Fluorescence imaging is performed on the chamber after the active water disinfection area.

REFERENCES

[1] A. Polman and H. A. Atwater, "Photonic design principles for ultrahigh-efficiency photovoltaics," *Nature Materials*, vol. 11, pp. 174–177, 2012.

[2] M. G. Walter et al., "Solar water splitting cells," *Chem. Rev.*, vol. 110, pp. 6446–6473, 2010.

[3] D. W. Hahn, "Rayleigh/mie light scattering," 2009. [Online]. Available: http://plaza.ufl.edu/dwhahn/

[4] K. A. Willets and R. P. V. Duyne, "Localized surface plasmon spectroscopy and sensing," *Ann. Rev. Phys. Chem.*, vol. 58, pp. 267–297, 2007.

[5] K. Kneipp, H. Kneipp, I. Itzkan, R. R. Dasari, and M. S. Feld, "Surface-enhanced raman scattering and biophysics," *J. Phys.: Condens. Matter*, vol. 14, pp. R597–R624, 2002.

[6] M. Moskovits, *Surface-Enhanced Raman Spectroscopy.* New York, NY: Springer, 2006.

[7] Y. J. Oh et al., "Beyond the SERS: Raman enhancement of small molecules using nanofluidic channels with localized surface plasmon resonance," *Small*, vol. 7, pp. 184–188, 2011.

[8] V. Giannini, J. A. Sanchez-Gil, O. L. Muskens, and J. G. Rivas, "Electrodynamic calculations of spontaneous emission coupled to metal nanostructures of arbitrary shape: nanoantenna-enhanced fluorescence," *J. Opt. Soc. Am. B*, vol. 26, pp. 1569–1577, 2009.

[9] S. K. Ghosh and T. Pal, "Interparticle coupling effect on the surface plasmon resonance of gold nanoparticles: from theory to applications," *Chem. Rev.*, vol. 107, pp. 4797–4862, 2007.

[10] C. J. Choi, Z. Xu, H. Y. Wu, G. L. Liu, and B. T. Cunningham, "Surface-enhanced raman nanodomes," *Nanotechnology*, vol. 21, p. 415301, 2010.

[11] J. J. Greffet, "Introduction to surface plasmon theory," Summer School On Plasmonics, Porquerolles, 2009.

[12] R. Clegg, "Physics 552: Optical spectroscopy," University of Illinois at Urbana-Champaign, 2010.

[13] R. Shimokawa, K. Ishii, and T. Takahashi, "Optical confinement in thin film Si solar cells by diffuse reflective substrate," *Jpn. J. Appl. Phys.*, vol. 35, pp. 3445–3456, 1996.

[14] N. N. Feng et al., "Design of highly efficient light-trapping structures for thin-film crystalline silicon solar cells," *IEEE Trans. Elec. Dev.*, vol. 54, pp. 1926–1933, 2007.

[15] R. B. Stephens and G. D. Cody, "Optical reflectance and transmission of a textured surface," *Thin Solid Films*, vol. 45, pp. 19–29, 1977.

[16] H. M. Branz, V. E. Yost, S. Ward, K. M. Jones, B. To, and P. Stradins, "Nanostructured black silicon and the optical reflectance of graded-density surfaces," *Appl. Phys. Lett.*, vol. 94, pp. 231 121–231 123, 2009.

[17] X. Li and P. W. Bohn, "Metal-assisted chemical etching in HF/H_2O_2 produces porous silicon," *Appl. Phys. Lett.*, vol. 77, pp. 2572–2574, 2000.

[18] H. C. Yuan, V. E. Yost, M. R. Page, P. Stradins, D. L. Meier, and H. M. Branz, "Efficient black silicon solar cell with a density-graded nanoporous surface: Optical properties, performance limitations, and design rules," *Appl. Phys. Lett.*, vol. 95, pp. 123 501–123 503, 2009.

[19] O. L. Muskens, J. G. Rivas, R. E. Algra, E. P. A. M. Bakkers, and A. Lagendijk, "Design of light scattering in nanowire materials for photovoltaic applications," *Nanolett.*, vol. 8, pp. 2638–2642, 2008.

[20] Y. H. Pai et al., "Aspect-ratio-dependent ultra-low reflection and luminescence of dry-etched Si nanopillars on Si substrate," *Nanotechnology*, vol. 20, p. 035303, 2009.

[21] G. L. Liu, Y. Choi, S. Kwon, and L. P. Lee, "Nanopillar substrate for SERS," in *Proceedings of Micro Total Analysis Systems 2003*, Squaw Valley, CA, USA, Oct. 2003, pp. 705–708.

[22] Y. F. Huang et al., "Improved broadband and quasi-omnidirectional anti-reflection properties with biomimetic silicon nanostructures," *Nature Nanotech.*, vol. 2, pp. 770–774, 2007.

[23] L. Sainiemi et al., "Nonreflecting silicon and polymer surfaces by plasma etching and replication," *Adv. Mater.*, vol. 23, pp. 122–126, 2011.

[24] A. Sharma and R. Khanna, "Pattern formation in unstable thin liquid films," *Phys. Rev. Lett.*, vol. 81, pp. 3463–3466, 1998.

[25] J. Bischof, D. Scherer, S. Herminghaus, and P. Leiderer, "Dewetting modes of thin metallic films: Nucleation of holes and spinodal dewetting," *Phys. Rev. Lett.*, vol. 77, pp. 1536–1539, Aug 1996. [Online]. Available: http://link.aps.org/doi/10.1103/PhysRevLett.77.1536

[26] C. Hedlund, H. O. Blom, and S. Berg, "Microloading effect in reactive ion etching," *J. Vac. Sci. Technol. A*, vol. 12, pp. 1962–1965, 1994.

[27] S. S. Walavalkar et al., "Tunable visible and near-IR emission from sub-10 nm etched single-crystal Si nanopillars," *Nano Lett.*, vol. 10, pp. 4423–4428, 2010.

[28] S. S. Walavalkar et al., "Size tunable visible and near-infrared photoluminescence from vertically etched silicon quantum dots," *Appl. Phys. Lett.*, vol. 98, pp. 153 114–153 116, 2011.

[29] M. Gartia et al., "Rigorous surface enhanced raman spectral characterization of large-area high-uniformity silver-coated tapered silica nanopillar arrays," *Nanotechnology*, vol. 21, p. 395701, 2010.

[30] I. S. Chun, E. Chow, and X. Li, "Nanoscale three dimensional pattern formation in light emitting porous silicon," *Appl. Phys. Lett.*, vol. 92, pp. 191 113–191 115, 2008.

[31] K. H. Hsu, P. L. Schultz, P. M. Ferreira, and N. X. Fang, "Electrochemical nanoimprinting with solid-state superionic stamps," *Nano Lett.*, vol. 7, pp. 446–451, 2007.

[32] W. Chern et al., "Nonlithographic patterning and metal-assisted chemical etching for manufacturing of tunable light-emitting silicon nanowire arrays," *Nano Lett.*, vol. 10, pp. 1582–1588, 2010.

[33] C. M. Hsu, S. T. Conner, M. X. Tang, and Y. Cui, "Wafer-scale silicon nanopillars and nanocones by LangmuirBlodgett assembly and etching," *Appl. Phys. Lett.*, vol. 93, pp. 133 109–133 111, 2008.

[34] J. Zhu et al., "Optical absorption enhancement in amorphous silicon nanowire and nanocone arrays," *Nano Lett.*, vol. 9, pp. 279–282, 2009.

[35] H. Sai, H. Fujii, K. Arafune, Y. Ohshita, and M. Yamaguchi, "Antireflective subwavelength structures on crystalline Si fabricated using directly formed anodic porous alumina masks," *Appl. Phys. Lett.*, vol. 88, pp. 201 116–201 118, 2006.

[36] A. P. Li, F. Muller, A. Birner, K. Nielsch, and U. Gosele, "Hexagonal pore arrays with a 50420 nm interpore distance formed by self-organization in anodic alumina," *J. Appl. Phys.*, vol. 84, pp. 6023–6026, 1998.

[37] F. Muguele and J. C. Baret, "Electrowetting: from basics to applications," *J. Phys.: Condens. Matter*, vol. 17, pp. 705–774, 2005.

[38] M. Nosonovsky and B. Bhushan, "Biomimetic superhydrophobic surfaces: Multiscale approach," *Nano Lett.*, vol. 7, pp. 2633–2637, 2007.

[39] W. Ren, C. Cheng, R. Wang, and X. Li, "Effect of fiber surface morphology on the hydrophilicity modification of cold plasma-treated polypropylene nonwoven fabrics," *J. Appl. Polymer Sci.*, vol. 116, pp. 2480–2486, 2010.

[40] S. L. Diedenhofen et al., "Broad-band and omnidirectional antireflection coatings based on semiconductor nanorods," *Adv. Mater.*, vol. 21, pp. 973–978, 2009.

[41] H. Jin and G. L. Liu, "Fabrication and optical characterization of light trapping silicon nanopore and nanoscrew devices," *Nanotechnology*, vol. 23, p. 125202, 2012.

[42] H. Jin, Z. Xu, A. Hsiao, P. Vuttipittayamongkol, and G. L. Liu, "Microfluidics with monolithically integrated self- wetting and fluorescence enhancing 3D nanostructured surface," in *Proceedings of Micro Total Analysis Systems 2011*, Seattle, WA, USA, Oct. 2011.

[43] M. Schmelzeisen, Y. Zhao, M. Klapper, K. Mullen, and M. Kreiter, "Fluorescence enhancement from individual plasmonic gap resonances," *ACS Nano*, vol. 4, pp. 3309–3317, 2010.

[44] Y. Chen, K. Munechika, and D. S. Ginger, "Dependence of fluorescence intensity on the spectral overlap between fluorophores and plasmon resonant single silver nanoparticles," *Nano Lett.*, vol. 7, pp. 690–696, 2007.

[45] B. Yang et al., "Tuning the intensity of metal-enhanced fluorescence by engineering silver nanoparticle arrays," *Small.*, vol. 7, pp. 1038–1043, 2010.

[46] G. L. Liu, Y. Lu, J. Kim, J. C. Doll, and L. P. Lee, "Magnetic nanocrescents as controllable surface enhanced Raman scattering nanoprobes for biomolecular imaging," *Adv. Mater.*, vol. 17, pp. 2683–2688, 2005.

[47] J. J. Mock, D. R. Smith, and S. Schultz, "Local refractive index dependence of plasmon resonance spectra from individual nanoparticles," *Nano Lett.*, vol. 3, pp. 485–491, 2003.

[48] Y. H. Lee, H. Chen, Q. H. Xu, and J. Wang, "Refractive index sensitivities of noble metal nanocrystals: The effects of multipolar plasmon resonances and the metal type," *J. Phys. Chem. C*, vol. 115, pp. 7997–8004, 2011.

[49] J. S. Sekhon and S. S. Verma, "Refractive index sensitivity analysis of ag, au, and cu nanoparticles," *Plasmonics*, vol. 6, pp. 311–317, 2011.

[50] M. Knight, H. Sobhani, P. Nordlander, and N. J. Halas, "Photodetection with active optical antennas," *Science*, vol. 332, pp. 702–704, 2011.

[51] S. J. Park, T. A. Taton, and C. A. Mirkin, "Array based electrica detection of DNA with nanparticle probes," *Science*, vol. 295, pp. 1503–1506, 2002.

[52] R. D. Glover, J. M. Miller, and J. E. Hutchison, "Generation of metal nanoparticles from silver and copper objects: nanoparticle dynamics on surfaces and potential sources of nanoparticles in the environment," *ACS Nano*, vol. 5, pp. 8950–8956, 2011.

[53] S. Kittler, C. Greulich, J. Diendorf, M. Koller, and M. Epple, "Toxicity of silver nanoparticles increases during storages because of slow dissolution under release of silver ions," *Chem. Mater.*, vol. 22, pp. 4548–4554, 2010.

[54] R. D. Kent and P. J. Vikesland, "Controlled evaluation of silver nanoparticle dissolution using atomic force microscopy," *Environ. Sci. Technol.*, p. article ASAP, 2011, dOI: 10.1021/es203475a.

[55] R. Jin et al., "Controlling anisotropic nanoparticle growth through plasmon excitation," *Nature*, vol. 425, pp. 487–490, 2003.

[56] J. Zhang, M. R. Langille, and C. A. Mirkin, "Photomediated synthesis of silver triangular bipyramids and prisms: the effect of pH and BSPP," *J. Am. Chem. Soc.*, vol. 132, pp. 12 502–12 510, 2010.

[57] R. Jin, Y. Cao, C. A. Mirkin, K. L. Kelly, G. C. Schatz, and J. G. Zhang, "Photoinduced conversion of silver nanospheres to nanoprisms," *Science*, vol. 294, pp. 1901–1903, 2001.

[58] Y. Sun, B. Mayers, and Y. Xia, "Transformation of silver nanospheres into nanobelts and triangular nanoplates through a thermal process," *Nano Lett.*, vol. 3, pp. 675–679, 2003.

[59] Z. Liu, W. Hou, P. Pavaskar, M. Aykol, and S. B. Cronin, "Plasmon resonant enhancement of photocatalytic water splitting under visible illumination," *Nano Lett.*, vol. 11, pp. 1111–1116, 2011.

[60] Y. Ling, G. Wang, D. A. Wheeler, J. Z. Zhang, and Y. Li, "Sn-doped hematite nanostructures for photoelectrochemical water splitting," *Nano Lett.*, vol. 11, pp. 2119–2125, 2011.

[61] S. Y. Reece, J. A. Hamel, K. Sung, T. D. Jarvi, A. J. Esswein, J. J. H. Pijpers, and D. G. Nocera, "Wireless solar water splitting using silicon-based semiconductors and earth-abundant catalysts," *Science*, vol. 4, pp. 645–648, 2011.

[62] Y. J. Hwang, A. Boukai, and P. Yang, "High density n-Si/n-TiO_2 core/shell nanowire arrays with enhanced photoactivity," *Nano Lett.*, vol. 9, pp. 410–415, 2009.

[63] Y. W. Chen et al., "Atomic layer-deposited tunnel oxide stabilizes silicon photoanodes for water oxidation," *Nature Materials*, vol. 10, pp. 539–544, 2011.

[64] P. Christopher, H. Xin, and S. Linic, "Visible-light enhanced catalytic oxidation reactions on plasmonic silver nanostructures," *Nature Chem.*, vol. 3, pp. 467–472, 2011.

[65] A. J. Nozik, "Photochemical diodes," *Appl. Phys. Lett.*, vol. 30, pp. 567–569, 1977.

[66] A. Meier, D. C. Selmarten, K. Siemoneit, B. B. Smith, and A. J. Nozik, "Fast electron transfer across semiconductor-molecule interfaces: GaAs/$Co(Cp)_2{}^{+/0}$," *J. Phys. Chem. B*, vol. 103, pp. 2122–2141, 1999.

[67] C. A. Koval and J. N. Howard, "Electron transfer at semiconductor electrode-liquid electrolyte interfaces," *Chem. Rev.*, vol. 92, pp. 411–433, 1992.

[68] A. M. Fajardo and N. S. Lewis, "Rate constants for charge transfer across semiconductor-liquid interfaces," *Science*, vol. 274, pp. 969–972, 1996.

[69] W. D. Li, F. Ding, J. Hu, and S. Y. Chou, "Three-dimensional cavity nanoantenna coupled plasmonic nanodots for ultrahigh and uniform surface-enhanced raman scattering over large area," *Optics Express*, vol. 19, pp. 3925–3936, 2011.

[70] P. C. P. Hrudey, K. L. Westra, and M. J. Brett, "Highly ordered organic chiral luminescent thin films made using glancing angle deposition," *Adv. Mater.*, vol. 18, pp. 224–228, 2006.

[71] Z. Xu, Y. Chen, M. R. Gartia, J. Jiang, and G. L. Liu, "Surface plasmon enhanced broadband spectrophotometry on black silver substrates," *Appl. Phys. Lett.*, vol. 98, pp. 241 904–241 906, 2011.

[72] Z. Li, W. M. Tong, W. F. Stickle, D. L. Neiman, and R. S. Williams, "Plasma-induced formation of ag nanodots for ultra-high-enhancement surface-enhanced raman scattering substrates," *Langmuir*, vol. 23, pp. 5135–5138, 2007.

[73] National Academy of Engineering, "Provide access to clean water," 2012. [Online]. Available: http://www.engineeringchallenges.org/cms/8996/9142.aspx

[74] "Drying up," May 2005, The Economist. [Online]. Available: http://www.economist.com/node/4000643

[75] J. A. Byrne, P. A. Fernandez-Ibanez, P. S. M. Dunlop, D. M. A. Alrousan, and J. W. J. Hamilton, "Photocatalytic enhancement for solar disinfection of water: A review," *International Journal of Photoenergy*, vol. 2011, pp. 1–12, 2011.

[76] UN Millennium Project, "Goal 7: Ensure environmental sustainability," 2010. [Online]. Available: http://www.unmillenniumproject.org/goals/

[77] H. A. Foster, I. B. Ditta, S. Varghese, and A. Steele, "Photocatalytic disinfection using titanium dioxide: spectrum and mechanism of antimicrobial activity," *Appl. Microbiol. Biotechnol.*, vol. 90, pp. 1847–1868, 2011.

[78] O. K. Dalrymple, E. Stefanakos, M. A. Trotz, and D. Y. Goswami, "A review of the mechanisms and modeling of photocatalytic disinfection," *Applied Catalysis B: Environmental*, vol. 98, pp. 27–38, 2010.

[79] A. Mills and S. K. Lee, "A web-based overview of semiconductor photochemistry-based current commercial applications," *Journal of Photochemistry and Photobiology A*, vol. 152, pp. 233–247, 2002.

[80] A. Hamamoto et al., "New water disinfection system using uva light-emitting diodes," *Jour. Appl. Microbiol.*, vol. 103, pp. 2291–2298, 2007.

[81] R. Khaengraeng and R. H. Reed, "Oxygen and photoinacti- vation of escherichia coli in uva and sunlight," *Jour. Appl. Microbiol.*, vol. 99, pp. 39–50, 2005.

[82] Stanford Solar Car Project Team, "Stanford solar car project," 2012. [Online]. Available: http://solarcar.stanford.edu/

[83] P. Torcellini, S. Pless, M. Deru, and D. Crawley, "Zero energy buildings: A critical look at the definition," Nat. Renewable Ener. Lab., Amherst, MA, Conference Paper NREL/CP-550-39833, 2006.

[84] A. Kudo and Y. Miseki, "Heterogeneous photocatalyst materials for water splitting," *Chem. Soc. Rev.*, vol. 38, pp. 253–278, 2009.